

Numerical simulations of three black holes

Dissertation
zur Erlangung des akademischen Grades

doctor rerum naturalium (Dr. rer. nat.)

vorgelegt dem Rat der Astronomisch-Physikalischen Fakultät
der Friedrich-Schiller-Universität Jena

von

M. en C. Juan Pablo Galaviz Vilchis

geboren am 21. Januar 1979 in Mexiko

Gutachter

- 1. Prof. Dr. Gerhard Zumbusch**
- 2. Prof. Dr. Bernd Brüggemann**
- 3. Prof. Dr. Luciano Rezzolla**

Tag der Disputation: 14. Dezember 2010

Contents

1	Introduction	5
1.1	Background	8
1.2	Motivation	10
2	Initial data for multiple black holes evolution	13
2.1	Puncture method	14
2.2	Numerical solution of the Hamiltonian constraint	15
2.2.1	Multigrid method	16
2.2.2	Results	22
3	Numerical evolution of three black holes	31
3.1	Numerical relativistic three black hole simulations	31
3.1.1	The moving puncture approach	31
3.1.2	Mergers and gravitational waves	32
4	Post-Newtonian simulation of three black holes	41
4.0.3	Post-Newtonian equations of motion up to 2.5 order	43
4.0.4	Gravitational radiation in the linear regime	44
4.1	Simulations and results	48
4.1.1	Numerical integration	49
4.1.2	Strong perturbation of a binary system	56
5	Conclusions	65

Bibliography	67
A Multigrid methods	75
B Newton-Raphson method	87
C Convergence of C^n functions	91
D First and second post-Newtonian Hamiltonian	95
Ehrenwörtliche Erklärung	97
Zusammenfassung	98

Chapter 1

Introduction

The classical three-body problem refers to the motion of three celestial bodies under their mutual Newtonian gravitational attraction. The three-body problem is one of many scientific problems where a small generalisation of a simple problem resulted in a very hard problem to solve. Using a coordinate transformation it is possible to reduce the two-body problem to a single body problem. The equations of motion of the reduced problem can be integrated to give a closed-form solution. On the other hand, for the three-body problem only in a few cases the equations of motion can be reduced in a simple enough form to obtain an analytical solution. In general, the three-body problem is formulated in terms of a coupled system of 18 first order non-linear ordinary differential equations. It is possible to find 12 constants of motion which reduce the system to one of six equations. The solution of the classical three-body problem is formally given by a convergent power series.

The Three-body problem is important from a historical point of view because many of the attempts to solve it resulted in new mathematical ideas and methods. In the next paragraphs we will give a short chronology of highlight attempts to solve the problem. More about the history of the three-body problem can be found in [15, 132] and references therein. The early attempts start around 1687 when Issac Newton published *Principia* and geometrically solved the problem of two bodies. Newton tried without success to solve with the same techniques the problem of describing the orbits of the moon, earth and sun. Between 1748 and 1772 Euler studied the

restricted problem¹ and found a particular solution² where the three bodies stay in a collinear configuration. Clairaut published “*Théorie de la lune*” in 1752 and two years later he applied his knowledge of the three-body problem to compute lunar tables and the orbit of Halley’s comet to predict the date of its return. The approximate method of Clairaut to calculate the orbit of Halley’s comet was quite accurate and the comet appeared in 1759, only one month before the predicted date. Lagrange found in 1772 a particular solution where the three bodies are placed at the corners of an equilateral triangle. In the general case the lengths of the sides can vary, keeping their ratio constant. Studying the restricted problem, Lagrange found five special points where the forces acting on the third body of a rotating system are balanced. Jacobi showed in 1836 that the restricted problem can be represented by a system of fourth-order differential equations. Between 1860 and 1867 Delaunay applied the method of variation of parameters to the restricted problem and was the first to complete a total elimination of the secular terms in the problem of lunar theory. Gyldén’s main research from 1881 to 1893 was devoted to the study of the sun and two planets, where one planet is designated as disturbing and the other is disturbed. In 1883 Lindstedt provided trigonometric series solutions for the restricted three-body problem. One year later a phenomenological description of the main features of the planetary and the lunar motion was published by Airy [4]. Hill published in 1877 a paper on the motion of the lunar perigee which contains new periodic solutions to the three-body problem. Later in 1878 he published a paper on the lunar theory which included a more complete derivation of the periodic solutions.

The classical period of the three-body problem research arrives in its final phase with Poincaré’s works. Hill’s investigation on the theory of periodic solutions had a fundamental influence on Poincaré’s research in this field. In 1890 Poincaré published a memoir on the (restricted) three body problem which is a reviewed version of the original work which won King Oscar’s Price.³ Poincaré’s memoir goes beyond the three-body problem and deals for the first time with the qualitative theory of dynamical systems. Poincaré’s work also provided the

¹The restricted three-body problem refers to the case where a third body, assumed mass-less with respect to other two, moves in the plane defined by the two revolving bodies. While being gravitationally influenced by them, it exerts no influence of its own.

²Particular solutions are those solutions in which the geometric configuration of the three bodies remains invariant with respect to the time.

³Poincaré’s memoir was published in the journal *Acta Mathematica* as the winning entry in the international Price competition honouring the 60th birthday of Oscar II, King of Sweden and Norway.

foundations for the author's three-volume "*Les Méthodes Nouvelles de la Mécanique Céleste*" and contains the first mathematical description of chaotic behaviour in a dynamical system. Poincaré's memoir includes many important results, among others, the discovery of *homoclinic points*, the recurrence theorem, application of the theory of asymptotic solutions to the restricted three body problem and a distinction between *autonomous* and *non-autonomous* Hamiltonian systems of differential equations.

In 1912 Sundman mathematically solved the problem by providing a convergent power series solution valid for all values of time [15, 119]. However, the rate of convergence of the series which he had derived is extremely slow, and it is not useful for practical purposes. Barrau considered in 1913 an initial configuration where three bodies are initially at the corners of a Pythagorean right triangle.⁴ The masses of the three bodies are 3, 4 and 5 units, and they are placed at the corners which face the sides of the triangle of the corresponding length. Between 1750 and the beginning of 20th century more than 800 papers relating to the three body problem were published.

In 1915 the astrophysical three-body problem changed with the publication of Einstein's general relativity theory. In some sense a new three-body problem was born together with the theory which includes new features. We can refer to the relativistic three-body problem as the three compact objects problem because only for stellar compact object, like neutron stars and black holes, its requires a relativistic description. For most of the stellar objects the classical three-body problem is good enough for describing the dynamics of such objects. This is a contribution to the study of the three compact objects problem from the numerical point of view.

Since the 1950's the computational numerical simulations of the three body problem provides the best approximation to the solution for a given initial configuration. We have to notice that numerical solutions of the n -body problem does not distinguish between two, three or more bodies in the sense that the same techniques works in each case. The only difficulty arrives from the fact that the computational cost increases with the inclusion of more bodies into the problem. The same is true for the relativistic case. The numerical relativistic methods to perform evolutions of two black holes are equally applicable for three or more black holes. There are many methods for integration of orbits, however the details are beyond the scope of this work.

⁴A Pythagorean triangle is a right triangle with sides of length 3, 4 and 5 units.

We describe the numerical techniques that we use to integrate the orbits in Sec. 3.1.1 and 4.0.4. More about numerical integration of the three-body problem can be found in [2].

The thesis is organised as follows. The rest of this chapter is devoted to the description of some of the recent work related to the classical three-body problem and the relativistic case where the inclusion of gravitational radiation is a new ingredient. We give also the motivation for this work, describing the new contributions presented in this thesis. In Chap. 2 we review the puncture method [17, 18, 28], which is the basic approach that we use to solve the initial data problem. This is followed by a description of the multigrid method to solve numerically the Hamiltonian constraint and its implementation in OLLIPTIC, a parallel computational code which solves three dimensional systems of non-linear elliptic equations with a 2nd, 4th, 6th, and 8th order finite difference multigrid methods. At the end of the chapter we present the result of some accuracy tests. In Chap. 3 the evolution of three black holes is presented. In Sec. 3.1 we describe the full numerical relativistic method that we use to evolve three black holes in a close configuration and we present the result of some simulations. The numerical solution of the equations of motion in the 2.5 Post-Newtonian regime is presented in Chap. 4. We describe the numerical approach and we review the basic equations used to calculate the gravitational waveform from a point-like object. At the end of the chapter we present the numerical results. We conclude with a discussion in Chap. 5. In the appendices we give some details of the formulation.

1.1 Background

A well known result on the three body problem is that some of the configurations are chaotic. On the other hand as we pointed out before there are particular configurations which are periodic and in some cases stable.⁵ Recently new periodic solutions were found [75, 104, 105, 106].⁶ There is evidence of the existence of periodic solutions when non-radiative relativistic corrections are included in the equations of motion via post-Newtonian corrections [80, 93]. The gravitational waveform of periodic configurations in the Newtonian regime was studied in [9, 44, 127]. The stability of the Lagrangian points in a black hole binary system which in-

⁵For example the Lagrange's solution is stable if one of the bodies holds more than 95% of the total mass [132].

⁶A subclass of periodic solutions are those where every particle moves periodically in a single closed orbit. Such solutions are known as *choreographic*, an example which involve three bodies is Moore's figure eight [105].

clude the effect of gravitational radiation was studied in [116].

The chaotic behaviour of triple systems is well known in the Newtonian case, (see e.g., [132] and references therein). There is evidence that chaos appears in some cases using post-Newtonian approximation for system of spinning binaries (see e.g., [90, 49, 14, 91, 61, 71, 115]). As natural generalisation of the Newtonian case we expect that the three compact objects problem exhibit a chaotic behaviour. An important question is: how does the gravitational radiation change the chaotic properties of the system?

From the astrophysical point of view several models of three or more black holes have been studied recently. Hierarchical three black hole configurations interacting in a galactic core were studied by several authors. For example in [64, 65, 66] some configurations of intermediate-mass black holes (IMBHs) with different mass ratios were studied. The inclusion of gravitational radiation was done via effective force which includes 1 PN and 2.5 PN correction to the binary dynamics. The configurations consist of a binary system in a quasi-circular orbit and a third black hole approaching from a distance around 200 times the binary separation. The initial eccentricity was specified in a random way. N-body simulations of dynamical evolution of triple equal-mass super-massive black holes (SMBHs) in a galactic nuclei were done in [81]. The method includes effective force with gravitational radiation terms and galaxy halo interactions. In [78] the dynamics of repeated triple SMBHs interactions in galactic nuclei for several mass ratios and eccentricities were studied. The simulations were performed using Newtonian dynamics with corrections through an additional force which includes 2.5 PN correction to the binary dynamics and stellar dynamical friction. Other astrophysical applications of multiple black holes simulations include for example three-body kicks [77, 63] and binary-binary encounters (see e.g., [98, 99, 103, 74, 131]).

The first complete simulations using general-relativistic numerical evolutions of three black holes were presented in [42, 94] (see [36, 52]⁷ for very limited early examples of multiple black

⁷The first proof of principle simulation showing that puncture evolutions generalise to three or more black holes with minimal changes to a binary code was performed in 1997 [35]. Since this was an unpublished report, we summarise one of these simulations here. 30 black holes were arranged in a planar configuration using Brill-Lindquist data. Evolutions were performed using the fixed puncture method with the ADM formulation, maximal slicing, and vanishing shift, using an early version of the BAM code [34, 36]. Shown at [1] is the lapse at $t = 0.5M$, which was initialised to one and collapsed quickly towards zero near the punctures, thereby marking the location of the black holes. These simulations were not stable on orbital time scales, so neither the full merger nor waveforms were computed. About at the same time, there were also experiments with three black holes using the Cactus code, for which we are only aware of reference [52].

hole simulations). The recent simulations show that the dynamics of three compact objects display a qualitative different behaviour than the Newtonian dynamics.

1.2 Motivation

Einstein published in 1915 his general relativity theory and changed the picture of the stellar dynamics by the inclusion of gravitational radiation which is one of the main results of the theory. Gravitational waves are an extra component in the three-body problem of compact objects which enrich the phenomenology of the system. The changes in the energy and momentum resulting from the gravitational radiation produce a difference in the dynamics of the system. There are open questions related to the general-relativistic dynamics of n compact objects, for example the possible chaotic behaviour of the dynamics of n black holes, the inverse problem in gravitational wave emission, the existence of quasi-stationary solutions and their stability, etc.

In previous work on the numerical evolution of three black holes [42, 94], the initial data for the Hamiltonian constraint has been specified using an analytical approximate solution (see [94, 86, 51, 58, 59]) which introduces a finite error that does not converge to zero with numerical resolution. The reason to use such initial data is that, although accurate initial data for two black holes is readily available, this is not the case for more than two black holes. Below we show that solving the constraints numerically to obtain initial data for an arbitrary number of black holes, the result of the evolutions can change dramatically. The actual difference between the analytic approximation and the numerical initial data is not large (depending on the initial parameters), but, as expected, even small differences can lead to large changes for multiple black hole orbits. The new contribution of this work to the full numerical evolution of three black holes is the simulation of systems which satisfy numerically the Hamiltonian constrain and the comparison with evolutions made with the approximate prescription.

From the theoretical point of view the close encounter of three black holes is an interesting problem, as we will show in Sec. 3.1 the strong interaction of three bodies can produce very different kinds of waveforms showing single and double mergers. However, from the astrophysical point of view close encounters and triple merger are not expected to be common. Nevertheless, a probable situation is a binary system which is strongly perturbed by a third black hole. For this case a post-Newtonian approach can be appropriate. For the systems studied in previous

works the Newtonian dynamics provide a good description to the dynamics of the third body and the post-Newtonian corrections are considered only for the binary.

Although using post-Newtonian techniques it is possible to describe the dynamics of n compact objects, up to 3.5 PN order, most of the results are specialised for binary systems. The new contribution of this work to the post-Newtonian study of compact objects is the numerical simulation of three black holes which include gravitational radiation via 2.5 PN formulation. In order to perform such simulations, we compute explicitly the equations of motion for the triple system up to 2.5 post-Newtonian approximation. We consider configurations where the three bodies require a post-Newtonian description. Moreover, we compute the gravitational waveforms of the triple systems. For the stronger perturbed binary, we found a relationship between the modulation of the mass octupole and current quadrupole part of the waveform and the period of the external black hole.

Chapter 2

Initial data for multiple black holes evolution

Under a 3+1 decomposition, the Einstein equations split into a set of evolution equations and constraint equations, namely the Hamiltonian and momentum constraints. The Bianchi identities guarantee that if the constraints are initially satisfied they will remain satisfied during the subsequent evolution. However, for numerical solutions that is true only in an approximate way. In vacuum the constraint equations read as follows:

$$\nabla_j (K^{ij} - \gamma^{ij} K) = 0, \quad (2.1)$$

$$R^2 + K^2 - K_{ij} K^{ij} = 0, \quad (2.2)$$

where R is the Ricci scalar, K_{ij} is the extrinsic curvature and K its trace, γ_{ij} is the 3-metric, and ∇_j the covariant derivative associated with γ_{ij} . In the following sections we will present a way to solve numerically the system of equation (2.1)-(2.2) to specify initial data for multiple black holes evolutions. The discussion found here can be seen in more detail in [5, 48, 62]. A description of an early version of the computational code OLLIPTIC and the mathematical background was done in [55] (Master Thesis in Spanish). Here we summarise some of the important results and we give a description of the new features.¹

¹The original code was a parallel second order multigrid elliptic solver. The main applications were the numerical solution of Brill's wave initial data and the evolution of the Schrödinger-Poisson system (see Appendix A). The new implementation includes boxes mesh refinement, high order finite difference scheme and the solution of

2.1 Puncture method

The constraints can be solved, for example, with the puncture method of [28]. N black holes are modelled by adopting the Brill-Lindquist wormhole topology [30] with $N+1$ asymptotically flat ends which are compactified and identified with points r_i on \mathbb{R}^3 . The coordinate singularities at the points r_i resulting from compactification are referred to as punctures.

Following the conformal transverse-traceless decomposition approach, we make the following assumptions for the metric and the extrinsic curvature:

$$\gamma_{ij} = \psi_0^4 \tilde{\gamma}_{ij}, \quad (2.3)$$

$$K_{ij} = \psi_0^{-2} \tilde{A}_{ij} + \frac{1}{3} K \gamma_{ij}, \quad (2.4)$$

where \tilde{A}^{ij} is trace free. We choose an initially flat background metric, $\tilde{\gamma}_{ij} = \delta_{ij}$, and a maximal slice, $K = 0$. The last choice decouples the constraint equations (2.1)-(2.2) which take the form

$$\partial_j \tilde{A}^{ij} = 0, \quad (2.5)$$

$$\Delta \psi_0 + \frac{1}{8} \tilde{A}^{ij} \tilde{A}_{ij} \psi_0^{-7} = 0. \quad (2.6)$$

Bowen and York [23] have obtained a non-trivial solution of Eq. (2.5) in a Cartesian coordinate system (x^i) , which by linearity of the momentum constraint can be superposed for any number of black holes (here the index n is a label for each puncture):

$$\begin{aligned} \tilde{A}^{ij} = & \sum_n \left[\frac{3}{2r_n^3} \left[x_n^i P_n^j + x_n^j P_n^i - \left(\delta^{ij} - \frac{x_n^i x_n^j}{r_n^2} \right) P_k^n x_n^k \right] \right. \\ & \left. + \frac{3}{r_n^5} \left(\epsilon^{ik} S_k^n x_n^l x_n^j + \epsilon^{jk} S_k^n x_n^l x_n^i \right) \right], \end{aligned} \quad (2.7)$$

where $r_n := \sqrt{x_n^2 + y_n^2 + z_n^2}$, ϵ^{ik}_l is the Levi-Civita tensor associated with the flat metric, and P_i and S_i are the ADM linear and angular momentum, respectively. The Hamiltonian constraint (2.6) becomes an elliptic equation for the conformal factor. The solution is split as a sum of a

singular term and a finite correction u ,

$$\psi_0 = 1 + \sum_n \frac{m_n}{2r_n} + u, \quad (2.8)$$

with $u \rightarrow 0$ as $r_n \rightarrow \infty$. The function u is determined by an elliptic equation on \mathbb{R}^3 and is C^∞ everywhere except at the punctures, where it is C^2 . The parameter m_n is called the bare mass of the n th puncture.

For the “physical” or outer boundary we require that $u \rightarrow A$ as $r \rightarrow \infty$. The standard condition used in this case is an inverse power fall-off,

$$u(r) = A + \frac{B}{r^q}, \quad \text{for } r \gg 1, \quad q > 0, \quad (2.9)$$

where the factor B is unknown. It is possible to get an equivalent condition which does not contain B by calculating the derivative of (2.9) with respect to r , solving the equation for B and making a substitution in the original equation. The result is a *Robin* boundary condition:

$$u(\vec{x}) + \frac{r}{q} \frac{\partial u(\vec{x})}{\partial r} = A. \quad (2.10)$$

In the case of the puncture method typically we set $A = 0$ and $q = 1$.

2.2 Numerical solution of the Hamiltonian constraint

The theory of elliptic equations is vast (see e.g., [67, 122, 123, 124, 133]). Analytical methods to solve elliptic equations include *separation of variables*, *Green’s function* and *variational methods* among other. However only in a few special cases it is possible to obtain analytical solutions. For a wide range of problems which involves elliptic equations it is possible to obtain accurate approximation to the solution through numerical methods. There are several numerical methods appropriate to solve partial differential elliptic equations (a brief selection of references are [84, 130, 109, 83, 24, 118, 89, 136]). Finite elements, finite differences and spectral methods are the most common numerical methods used to solve elliptic equations.

For most of the problems, spectral methods or finite elements produce in general more accurate solutions to elliptic equations than those obtained by finite difference methods [24].

However, in order to take full advantage of the spectral method for punctures, it is necessary to construct a special set of coordinates. Indeed, there exist coordinates in which the conformal correction u is smooth at the puncture [8]. Although these coordinates are in principle applicable for both spectral and finite differencing methods, the resulting grids are specific to two black holes. Generalising that approach to more than two punctures is an interesting but non-trivial challenge that we do not pursue in this work. Using finite difference multigrid methods with Cartesian coordinates, one advantage of the puncture construction is that it is possible to produce accurate solutions of the Hamiltonian constraint for multiple black holes with minimal changes to a code prepared for binaries.

In order to solve Eq. (2.6) numerically, we have written `OLLIPTIC` (see also [55]), a parallel computational code to solve three dimensional systems of non-linear elliptic equations with a 2nd, 4th, 6th, and 8th order finite difference multigrid method. The elliptic solver uses vertex-centred stencils and box-based mesh refinement that we describe in the next section. `OLLIPTIC` uses a standard multigrid method [27, 11, 26, 87, 72, 46] with a Gauss-Seidel Newton relaxation algorithm (e.g. [45]).

2.2.1 Multigrid method

Although there are different kinds of multigrid methods (for example additive or multiplicative, local MG, etc), here we summarise of the basic idea behind the multigrid method as it is implemented in `OLLIPTIC`. A brief description of some of the methods can be found in Appendix A. For a more complete discussion see for example [25, 29, 129, 89, 136].

Let \mathcal{L} be an elliptic operator, $\Omega \subset \mathbb{R}^3$ an open domain, and $u : \Omega \rightarrow \mathbb{R}$ the solution of the problem

$$\mathcal{L}u(\vec{x}) = \rho_i(\vec{x}) \quad \text{for} \quad \vec{x} \in \Omega, \quad (2.11)$$

$$\mathcal{B}u(\vec{x}) = \rho_b(\vec{x}) \quad \text{for} \quad \vec{x} \in \partial\Omega, \quad (2.12)$$

where \mathcal{B} is a boundary operator, $\rho_i : \Omega \rightarrow \mathbb{R}$ and $\rho_b : \partial\Omega \rightarrow \mathbb{R}$ are source terms. As a model problem we consider a single spinning or boosted puncture in a cubic domain² $\bar{\Omega} =$

²We define $\bar{\Omega} := \Omega \cup \partial\Omega$, i.e., $\bar{\Omega}$ is the closure of Ω

$[x_0, x_{n_x-1}] \times [y_0, y_{n_y-1}] \times [z_0, z_{n_z-1}]$:

$$\Delta u + \frac{1}{8} \tilde{A}^{ij} \tilde{A}_{ij} \left(1 + \frac{m}{2|\vec{x} - \vec{x}_0|} + u \right)^{-7} = 0 \quad \text{for } \vec{x} \in \Omega, \quad (2.13)$$

$$u(\vec{x}) + r \frac{\partial u(\vec{x})}{\partial r} = 0 \quad \text{for } \vec{x} \in \partial\Omega, \quad (2.14)$$

Where \vec{x}_0 is the location of the puncture and $r = |\vec{x}|$.

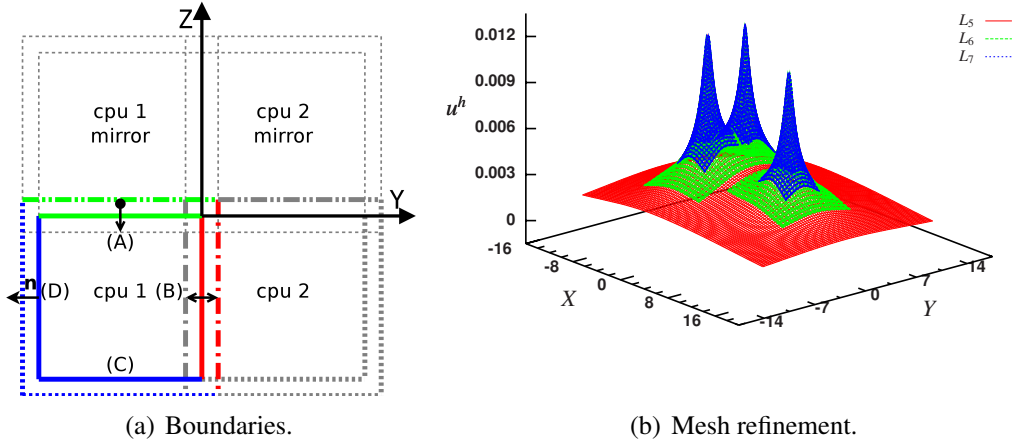


Figure 2.1: (a) 2D representation of a domain divided between 2 processors and with bitant symmetry. Face (A) is internal to the global domain and handles a reflection symmetry. Face (B) is internal to the domain and manages the communication with the second processor. Faces (C) and (D) are physical boundaries, where we impose a Robin boundary condition in the normal direction \vec{n} (see text). (b) Correction to the conformal factor for 3 punctures initial data. Here we plot the three finest levels of refinement (the total number of levels is 8). L_5 is a single box which covers the three punctures. L_6 contains 2 boxes, one covering 2 of the punctures. L_7 consist of 3 boxes each covering a puncture.

In order to solve numerically the equations using finite difference methods, we adopt the standard discretization approach with box-like mesh refinement. The numerical domain is represented by a hierarchy of nested Cartesian grids. The hierarchy consists of $L + G$ levels of refinement indexed by $l = 0, \dots, L + G - 1$. A refinement level consists of one or more Cartesian grids with constant grid-spacing h_l on level l . A refinement factor of two is used such that $h_l = h_G/2^{l-G}$. The grids are properly nested in that the coordinate extent of any grid at level

Table 2.1: Symmetries implemented in OLLIPTIC.

octant	quadrant	bitant
$z \rightarrow -z \quad \forall x, y$	$z \rightarrow -z \quad \forall x, y$	$z \rightarrow -z \quad \forall x, y$
$y \rightarrow -y \quad \forall x, z$	$y \rightarrow -y \quad \forall x, z$...
$x \rightarrow -x \quad \forall y, z$

$l > G$ is completely covered by the grids at level $l - 1$. The level $l = G$ is the “external box” where the physical boundary is defined. We use grids with $l < G$ to implement the multigrid method beyond level $l = G$. Each level is a uniform discrete set of grid points constituting the discrete domain Ω^h .

The parallelization approach that we use is block decomposition, in which each domain is divided into rectangular regions among the processors such that the computational work load is balanced. For levels $l \geq G$ every domain uses $p/2$ buffer points at the boundary of the domain. Levels with $l < G$ contain a single point at the boundary. For every face of the three dimensional rectangular domain we use these points for different purposes (see Fig. 2.1(a)):

1. If the face is on the outside of the global domain, we use the points as a refinement boundary (or physical boundary if $l = G$); the boundary conditions are explained below.
2. If the face is in the internal part of the global domain, then we use ghost zones of the neighbouring processors to update information of the buffer points.
3. If the face is defined with symmetry, we use a reflection condition to calculate the values at the boundary.

OLLIPTIC can be used with three symmetries which are useful for solutions which are spherical symmetric, axial symmetric or symmetric respect to a plane (see Table 2.1).

We use the negative part of the domain to define the computational grid, because that increases the performance of the relaxation method somewhat since the resulting order of point traversal helps propagating boundary information into the grid.

We describe first the numerical method as is implemented for the external box, after that we describe the refinement process. The mesh spacing in each direction is given by h_x, h_y and

h_z . However, for simplicity we assume $h_i = h$ for $i \in \{x, y, z\}$. Let \mathcal{L}^h be a finite difference representation of order p of \mathcal{L} in a mesh $\Omega^h \subset \mathbb{R}^3$. The exact solution $u^h : \Omega^h \rightarrow \mathbb{R}$ satisfies

$$\mathcal{L}^h u^h(\vec{x}^h) = \rho_i^h(\vec{x}^h) \quad \text{for} \quad \vec{x}^h \in \Omega^h, \quad (2.15)$$

$$\mathcal{B}^h u^h(\vec{x}^h) = \rho_b^h(\vec{x}^h) \quad \text{for} \quad \vec{x}^h \in \partial\Omega^h, \quad (2.16)$$

where \mathcal{B}^h is a discrete boundary operator and ρ_i^h and ρ_b^h are the restriction of ρ_i and ρ_b on Ω^h , respectively.

Points $\vec{x}_{ijk} = (x_i, y_j, z_k) \in \Omega^h$ are defined by $x_i = x_0 + ih_x$, $y_j = y_0 + jh_y$ and $z_k = z_0 + kh_z$, where $i \in \{0, 1, \dots, n_x - 1\}$, $j \in \{0, 1, \dots, n_y - 1\}$ and $k \in \{0, 1, \dots, n_z - 1\}$. For every grid function we use as notation $u_{ijk} := u^h(x_{ijk})$. In order to discretize the Laplacian operator in (2.13), we need finite difference approximation to the second derivatives. We use the standard 2nd, 4th, 6th or 8th order, centred approximations [54]. On the other hand for the first derivative at the boundary in (2.14) we use a corresponded one sided finite difference stencil of 2nd, 4th, 6th or 8th order.

In solving the system (2.15)-(2.16) iteratively we will only compute the exact discrete solution u^h in the limit of infinite iteration.³

$$\lim_{n \rightarrow \infty} U_n^h = u^h, \quad (2.17)$$

where n is an iteration index and U_n^h denotes the current numerical approximation to u^h . We define the residual r^h by:

$$r^h := \mathcal{L}^h U^h(\vec{x}^h) - \rho_i^h(\vec{x}^h) \quad \text{for} \quad \vec{x}^h \in \Omega^h, \quad (2.18)$$

$$r^h := \mathcal{B}^h U^h(\vec{x}^h) - \rho_b^h(\vec{x}^h) \quad \text{for} \quad \vec{x}^h \in \partial\Omega^h. \quad (2.19)$$

The task of the relaxation method is to adjust the values of U^h in order to reduce the residual. To do this it is useful to implement a Newton-Raphson method (see Appendix B for a short review of the method and examples of its implementation) which we apply pointwise. The iteration

³ u^h is in the practise exact up to machine accuracy and order $O(h^p)$

formula is

$$U_{ijk}^{n+1} = U_{ijk}^n - r_{ijk}^n \left[\frac{\partial r_{ijk}^n}{\partial u_{ijk}} \Big|_{u_{ijk}=U_{ijk}^n} \right]^{-1} \quad \text{for } \vec{x}^h \in \bar{\Omega}^h. \quad (2.20)$$

Notice that we use also a Newton-Raphson method to update the values on the boundary (using the appropriate definition of the residual).

The implementation of the boundary condition was a key point to get accurate solutions, so we describe our implementation in some detail. Rather than taking derivatives in the radial direction as is required by (2.14), we take derivatives only in the direction normal to the faces of our rectangular domain. At the edges of the boundary, we use a linear combination of the derivatives along the normals of the two adjacent faces. At the corners, we use a linear combination of the derivatives for the three adjacent faces. In the computation, we first apply the boundary condition to the interior of the boundary faces, then compute derivatives inside the faces to update the edges, and then compute derivatives inside the edges to obtain boundary data at the corners. Since there are $p/2$ boundary buffer points, we have to specify a method to obtain more than one buffer point. In our implementation the method is stable if we update the values of the boundary points from the inside to the outside of the domain. First, inside points are used to get the first boundary point using the one-sided derivative. Then the stencil is shifted by one from the inside to the outside, including the first boundary point to compute data at the second boundary point, and so forth.

For the inner points we update the values following a lexicographical order of the unknowns U_{ijk} , with the i index varying most rapidly than j , and j varying most rapidly than k . In the computation we use “new” values from iteration $n + 1$ wherever is available, i.e., we use a Gauss-Seidel relaxation method. This method is very easy to code and it is storage efficient. On the other hand relaxation methods are characterised by slow convergence. As we describe in appendix A a multigrid strategy can accelerate the calculation of the solution.

An important ingredient in a multigrid algorithm is the definition of a *prolongation operator* I_{2h}^h and a *restriction operator* I_h^{2h} . The prolongation operator interpolates between a coarse grid and a finer one. OLLIPTIC can use either linear interpolation, Lagrange of several orders of approximation or a method of splines of fourth-order. The restriction operator transfers the solution from a finer grid to the next coarse grid. In OLLIPTIC the grids are vertex-centred, as a consequence every point of the coarse grid is contained in the finer. For vertex-centred

arrangements it is possible to transfer the solution by *injection*⁴ or doing a *weighted restriction*. OLLIPTIC implements both approaches, using a half-weighted restriction defined by:

$$U_{I,J,K}^{2h} = \frac{1}{2}U_{i,j,k}^h + \frac{1}{12} \left(U_{i-1,j,k}^h + U_{i+1,j,k}^h + U_{i,j-1,k}^h + U_{i,j+1,k}^h + U_{i,j,k-1}^h + U_{i,j,k+1}^h \right),$$

where indices (i, j, k) and (I, J, K) label the fine and the coarse grids respectively. We use injection as default restriction operator, as long as, our test did not show significant difference in performance or accuracy.

We employ the *Full Approximation Storage Scheme* (see e.g., [11, 27, 32, 33] for details about the scheme). The corresponding pseudo-code for external and internal boxes are shown in algorithm 2.2.1 and 2.2.2 respectively.⁵ The three main differences between the implementation for internal and external boxes are the treatment of the boundary condition, the order of the interpolation used in the prolongation operator and the construction of the source used in the coarser level. In the case of the external boxes the procedure includes the calculation of the boundary condition together with the calculation of the elliptic operator. For internal boxes the boundary is not updated during the first part of the procedure; after the computation of the correction we fill the boundary with values which are interpolated from the coarser level. For external boxes it is enough to use linear interpolation for the prolongation operator. However, for internal boxes we observed a better results using interpolation of the same order as the finite difference stencil. For the Internal boxes the source of the coarse level consist on the original source in the region which is not cover by the finer level, and the standard source-correction of the FAS method for the points which are cover by the finer grid. In practise both algorithms are implemented as a single procedure with conditional statements placed in the proper stage.

⁴The injection restriction consists on do a copy of the corresponding data point by point from the finer to the coarser grid.

⁵As we mention before, external boxes are those which cover the whole computational domain. We impose in external boxes the physical boundary condition. On the other hand internal boxes cover a smaller region around the punctures (Fig. 2.1(b) shows internal boxes for three punctures.)

Algorithm 2.2.1: FAS($h, cycle, p, q, ord$)**comment:** External box

$$U^h \leftarrow \text{SMOOTH}(\mathcal{L}^h U^h = \rho_i^h, \mathcal{B}^h U^h = \rho_b^h, p)$$

$$\{\omega^h|_{\Omega^h} = \rho_i^h - \mathcal{L}^h U^h\} \wedge \{\omega^h|_{\partial\Omega^h} = \rho_b^h - \mathcal{B}^h U^h\}$$

$$\omega^{2h} \leftarrow \text{RESTRICT}(\omega^h, \bar{\Omega}^h \rightarrow \bar{\Omega}^{2h}, \text{Injection})$$

$$\{\rho_i^{2h} = \omega^{2h} + \mathcal{L}^{2h} U^{2h}\} \wedge \{\rho_b^{2h} = \omega^{2h} + \mathcal{B}^{2h} U^{2h}\}$$

$$U^{2h} \leftarrow \text{RESTRICT}(U^h, \bar{\Omega}^h \rightarrow \bar{\Omega}^{2h}, \text{Injection})$$

$$U_*^{2h} = U^{2h}$$

if $2h = h_{\max}$ **then** $U^{2h} \leftarrow \text{SOLVE}(\mathcal{L}^{2h} U^{2h} = \rho_i^{2h}, \mathcal{B}^{2h} U^{2h} = \rho_b^{2h})$ **else** $U^{2h} \leftarrow \text{FAS}(2h, cycle, p, q)$ $V^{2h} = U^{2h} - U_*^{2h}$ $V^h \leftarrow \text{PROLONG}(V^{2h}, \bar{\Omega}^h \leftarrow \bar{\Omega}^{2h}, \text{Linear})$ $U^h = U^h + V^h$ $U^h \leftarrow \text{SMOOTH}(\mathcal{L}^h U^h = \rho_i^h, \mathcal{B}^h U^h = \rho_b^h, q)$ $cycle++$ **Algorithm 2.2.2:** FAS($h, cycle, p, q, ord$)**comment:** Internal box

$$U^h \leftarrow \text{SMOOTH}(\mathcal{L}^h U^h = \rho_i^h, p)$$

$$\omega^h|_{\Omega^h} = \rho_i^h - \mathcal{L}^h U^h$$

$$\omega^{2h} \leftarrow \text{RESTRICT}(\omega^h, \Omega^h \rightarrow \Omega^{2h}, \text{Injection})$$

$$\rho_i^{2h}|_{\Omega^h} = \omega^{2h}|_{\Omega^h} + \mathcal{L}^{2h} U^{2h}|_{\Omega^h}$$

$$U^{2h} \leftarrow \text{RESTRICT}(U^h, \Omega^h \rightarrow \Omega^{2h}, \text{Injection})$$

$$U_*^{2h} = U^{2h}$$

 $U^{2h} \leftarrow \text{FAS}(2h, cycle, p, q)$ $V^{2h} = U^{2h} - U_*^{2h}$ $V^h \leftarrow \text{PROLONG}(V^{2h}, \Omega^h \leftarrow \Omega^{2h}, \text{Lagrange}_{ord})$ $U^h|_{\Omega^h} = U^h|_{\Omega^h} + V^h|_{\Omega^h}$ $U^h \leftarrow \text{PROLONG}(U^{2h}, \partial\Omega^h \leftarrow \Omega^{2h}, \text{Lagrange}_{ord})$ $U^h \leftarrow \text{SMOOTH}(\mathcal{L}^h U^h = \rho_i^h, \mathcal{B}^h U^h = \rho_b^h, q)$ $cycle++$

2.2.2 Results

Analytic test problems

We published the results that we present in the rest of this section in [56]. We test OLLIPTIC with three simple elliptic equations using the following procedure. Given the solution U^h on a mesh with grid-spacing h and an elliptic operator \mathcal{L}^h , we calculate a source ρ^h which satisfies the equation

$$\mathcal{L}^h U^h = \rho^h, \quad (2.21)$$

and then we solve the equation to obtain u^h numerically. In this way it is possible to calculate the error

$$E^h := |U^h - u^h|, \quad (2.22)$$

where $|\cdot|$ is a suitable norm. We summarise the grid setup for our tests and puncture initial data in Table 2.2.

The goals of the first test were to estimate the error introduced by the refinement method and to investigate the effectiveness of the algorithm to solve non-linear equations. We have solved

Table 2.2: Grid setups used for tests and puncture initial data. $l_r := l - G$ is the number of inner refinement levels, L is the length of the numerical domain and h_{min} is the grid size in the finest level (see text for details about each system).

System	Levels	Length	Grid size
	l_r	L	h_{min}
Test 1	1-4	$4.8 * 2^{l-1}$	1/20
Test 2 & 3	3	20.0	{0.1, 0.09, ..., 0.02}
1-puncture	5	40.0	{5/256, 1/64, 5/384}
2-punctures	7	40.0	{1/16, 1/32, 1/64}
3-punctures	7	50.0	5/64

the equation

$$\nabla^2 U(\vec{x}) + U(\vec{x})^2 = \rho_1(\vec{x}) \quad \text{for} \quad \vec{x} \in \Omega, \quad (2.23)$$

$$U(\vec{x}) = \epsilon e^{-\frac{1}{2}\vec{x}\cdot\vec{x}} \quad \text{for} \quad \vec{x} \in \partial\Omega, \quad (2.24)$$

where ∇^2 is the three-dimensional Laplace operator, and Ω is the interior of a rectangular domain. The solution given is a Gaussian function with amplitude $\epsilon = 0.004$, in this case we use a Dirichlet boundary condition. We have solved the equation with a single level of refinement in a cube of length $L = 4.8$, and with mesh size $dx = dy = dz = 0.05$. Using this solution as reference, we solve Eq. (2.23), increasing the number of levels up to 3 external boxes. Due to the Dirichlet boundary condition the numerical solution is exact at the boundary. We use the norm L_∞ to calculate the relative error,

$$R := \frac{|U^h - u^h|}{|U^h|}, \quad (2.25)$$

and as measurement of the error introduced by the refinement method, we calculate the difference between the error using more than one refinement level and the reference solution, $\Delta R = |R(l > 1) - R(l = 0)|$. The results are summarised in Table 2.3. The results for the non-linear Eq. (2.23) show that using high order schemes gives a significant improvement in the accuracy of the solution. Increasing the order from p to $p + 2$ decreases R by almost three orders of magnitude.

Table 2.3: Results of test 1, where p is the order of the stencil which we use to solve the equation, l is the number of refinement levels, R is the relative error calculated in the finest level and ΔR is the comparison with the reference solution.

p	2		4		6		8	
l	R	ΔR	R	ΔR	R	ΔR	R	ΔR
	$(\times 10^{-4})$		$(\times 10^{-7})$		$(\times 10^{-10})$		$(\times 10^{-12})$	
1	3.83	-	4.36	-	9.29	-	3.05	-
2	4.57	0.74	12.56	8.20	32.81	23.52	67.25	64.20
3	5.23	1.40	15.42	11.06	105.37	96.08	207.75	204.70
4	5.54	1.71	16.93	12.56	139.53	130.24	284.75	281.70

In order to test the implementation of the Robin boundary condition, we use a second trial function,

$$\nabla^2 U(\vec{x}) = \rho_2(\vec{x}) \quad \text{for} \quad \vec{x} \in \Omega, \quad (2.26)$$

$$U(\vec{x}) = \epsilon \frac{\tanh(r)}{r} \quad \text{for} \quad \vec{x} \in \partial\Omega, \quad (2.27)$$

where $r := |\vec{x}|$. The solution U is a function which has the asymptotic behaviour given by Eq. (2.9) with $A = 0$, $B = 1$, and $q = 1$. In this case we look at the convergence of our numerical data using 3 levels of refinement in a cubic domain of length 20, and using 7 resolutions going from 0.1 to 0.04 in the finest level.

For a finite difference implementation of order p , for $h \ll 1$, we expect

$$E^h \simeq Ch^p, \quad (2.28)$$

where E^h , is given by Eq. (2.22) using the L_2 norm, h is the mesh size, and C is constant with respect to h . After calculating the logarithm of Eq. (2.28) we get a linear function of p ,

$$\ln(E^h) \simeq p \ln(h) + C'. \quad (2.29)$$

Using this expression with our data and doing a linear regression analysis, we estimate the convergence order \mathcal{P} for our numerical experiment (in the best case $\mathcal{P} \rightarrow p$ as $h \rightarrow 0$). As measurement of the error we use the standard deviation and the coefficient of variation of our

Table 2.4: Convergence test for the Robin boundary condition. Here p is the order of the finite difference, \mathcal{P} , σ , and c_v are the mean, the standard deviation, and the coefficient of variation of the convergence order for our numerical experiments, respectively, and $\Delta\mathcal{P}$ is the relative deviation of our results with respect to p .

p	\mathcal{P}	σ	c_v	$\Delta\mathcal{P}$
2	2.002	0.0002	0.009%	0.10%
4	3.994	0.0005	0.013%	0.15%
6	5.985	0.0013	0.022%	0.26%
8	7.969	0.0020	0.026%	0.39%

data. The results are displayed in Table 2.4. We have obtained an accurate implementation of the boundaries for problem (2.26)-(2.27), where the difference between the theoretical convergence order and the experimental one is less than 0.5%. However, note that the convergence at the boundary depends on specific properties of the test problem.

For the last analytic test, we verify the accuracy of the method for a function which is $C_0^\infty := C^\infty(\mathbb{R}^3 \setminus \{\vec{0}\})$. The problem to solve was

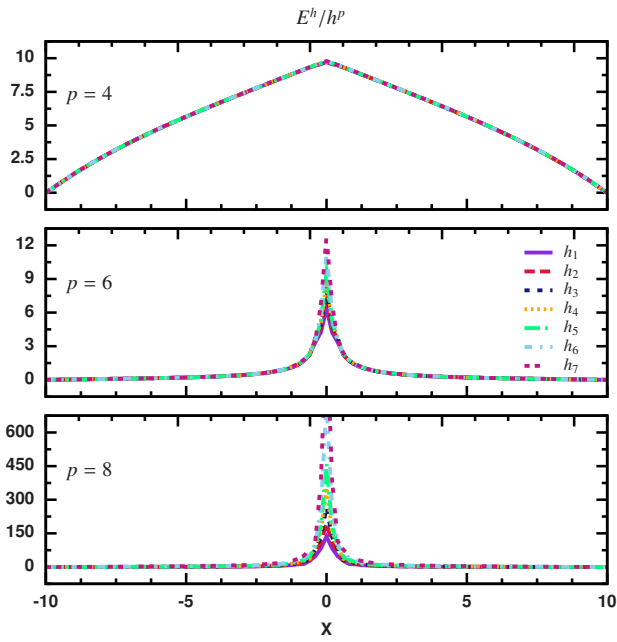
$$\nabla^2 U(\vec{x}) = \rho_3(\vec{x}) \quad \text{for } \vec{x} \in \Omega, \quad (2.30)$$

$$U(\vec{x}) = r^k \quad \text{for } \vec{x} \in \partial\Omega, \quad (2.31)$$

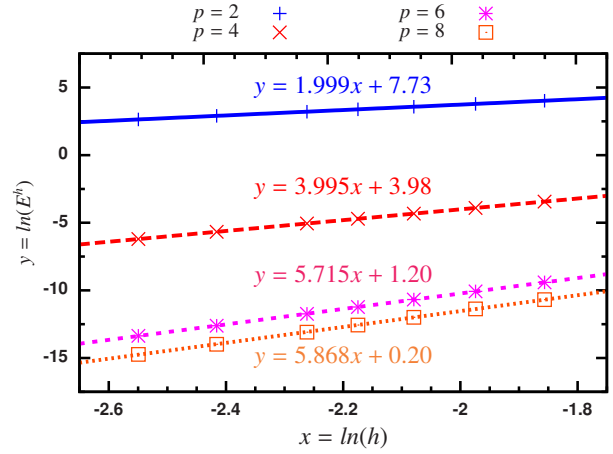
where we set $k = 3$ or $k = 5$, $r := |\vec{x}|$, and U is C^∞ everywhere except at the origin, where it is C^{k-1} . We use the procedure of the second test to estimate the convergence order, changing the equation and the boundaries (in this case we use a Dirichlet boundary condition). The result of our numerical experiments (detailed in Table 2.5) shows that the overall convergence of the numerical solution calculated using a standard finite differencing scheme is restricted by the differentiability of the analytical solution. The convergence order close to the origin (within a few grid points) is the same as the order of differentiability and improves significantly moving away from the origin (see Fig. 2.2 where we show the results for the case with $k = 5$). For more convergence test of an early version of the code see [55]. We show some of the performance results already presented in the previous reference in the Appendix A.

Table 2.5: Convergence for a solution which is C_0^∞ . Here k is the exponent given in (2.31).

k	3				5			
p	\mathcal{P}	σ	c_v	$\Delta\mathcal{P}$	\mathcal{P}	σ	c_v	$\Delta\mathcal{P}$
2	2.003	0.0003	0.013%	0.16%	1.999	0.0001	0.005%	0.06%
4	3.782	0.0088	0.233%	5.46%	3.995	0.0003	0.007%	0.12%
6	3.848	0.0067	0.175%	35.86%	5.715	0.0124	0.216%	4.74%
8	3.836	0.0038	0.098%	52.05%	5.868	0.0294	0.500%	26.65%



(a) Convergence test



(b) Convergence analysis

Figure 2.2: Convergence test for a solution which is $C^\infty(\Omega) \cup C^4(\vec{0})$. (a) Convergence test using OLLIPTIC with 4th, 6th and 8th order finite difference stencils. (b) Analysis of the convergence using the Eq. (2.29).

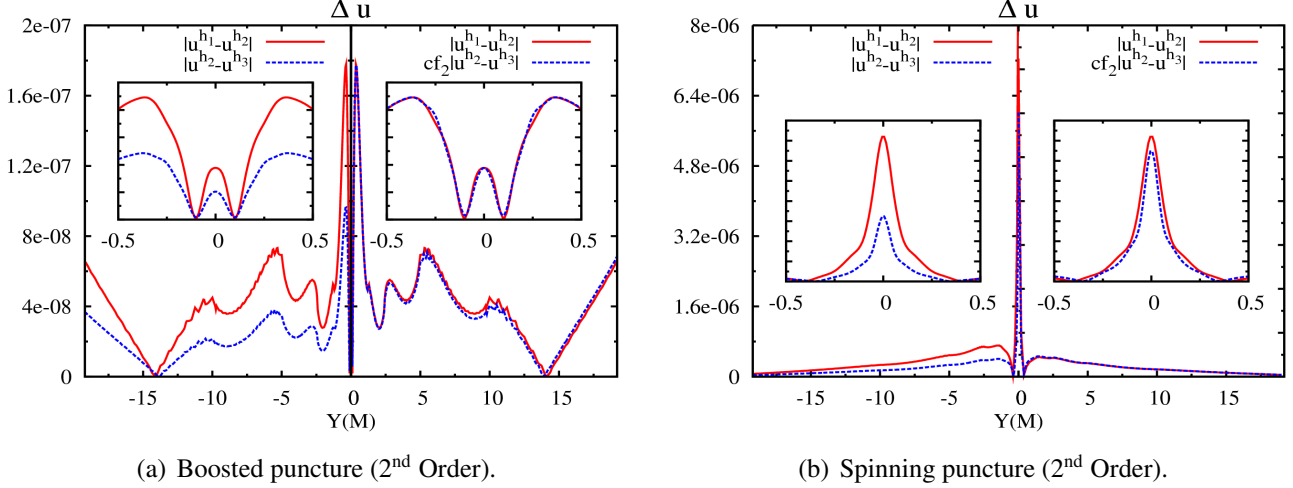


Figure 2.3: Regular part u of the conformal factor along the Y -axis of a single puncture. (a) Solution with vanishing spin parameter and with linear momentum $P_y = 0.2M$. (b) Solution with vanishing linear momentum and with spin $S_y = 0.2M$. In both cases, shown is a convergence test without scaling (left) and with scaling (right) for second-order convergence using $cf_2 = 1.8409$.

Single puncture initial data

After calibrating our code, we calculate the Hamiltonian constraint for a single puncture. We tested the convergence of our second-order implementation for a single boosted puncture ($P^i = 0.2 \delta_2^i M$, $S^i = 0$) by looking at the value of the regular part u of the conformal factor along the Y -axis for a cubic domain of length $40M$, 5 levels of refinement, and 3 resolutions $h_1 = (5/8)M$, $h_2 = 4h_1/5$, and $h_3 = 2h_1/3$ in the coarse level. In Fig. 2.3(a), we show rescaled and unscaled data for positive and negative values of Y , respectively.

We plot the values of $|u^{h_1} - u^{h_2}|$ and $|u^{h_2} - u^{h_3}|$ for $Y < 0$ on the left, and on the right values for $Y > 0$ with $|u^{h_2} - u^{h_3}|$ multiplied by a factor $cf_2 = 1.8409$ which corresponds to the proper scaling of second order. The lines in the right panel of the plot coincide almost everywhere, indicating second order convergence. We also show details of a region close to the puncture in the insets. We perform a similar test calculating spinning black hole initial data ($P^i = 0$, $S^i = 0.2 \delta_2^i M$). Fig. 2.3(b) shows the result of the convergence test for this case where we found second order convergence again.

As an example of a high order solution, in Fig. 2.4(a) we show the convergence test for the

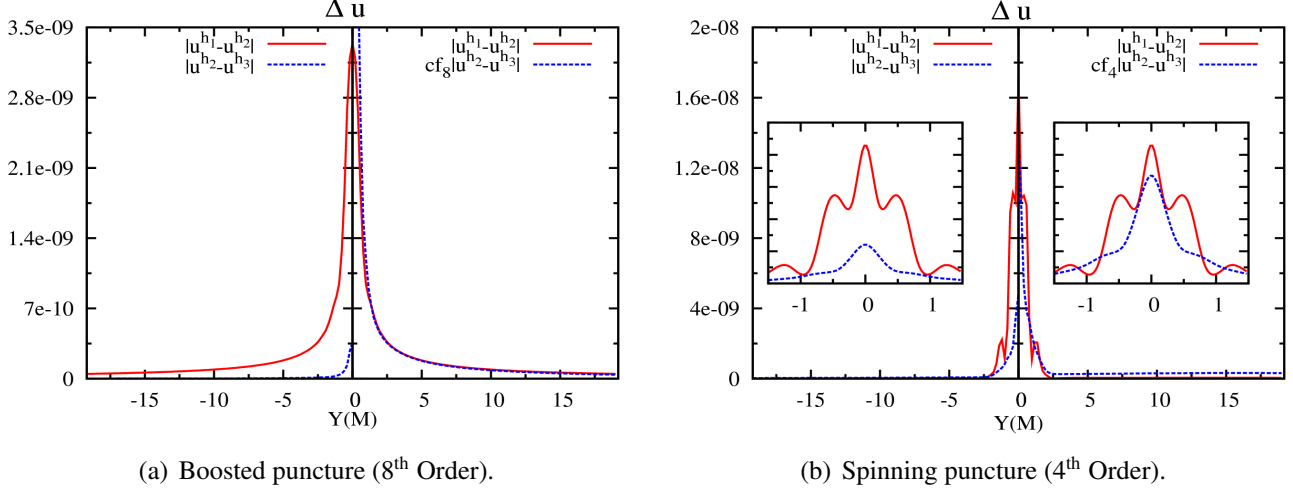


Figure 2.4: Regular part u of the conformal factor along the Y -axis of a single puncture. (a) Solution with vanishing spin parameter and with linear momentum $P_y = 0.2M$. Eighth-order convergence of u is obtained far from the puncture ($cf_8 = 6.4637$). (b) Solution with vanishing linear momentum and with spin $S_y = 0.2M$. Convergence test using $cf_4 = 2.7840$.

eighth order scheme of the boosted puncture. In this case the plot shows a drop of the convergence ratio close to the puncture. However, far from the puncture the convergence behaviour is better. In Fig. 2.4(b) we plot the results for the spinning black hole, obtained by using our fourth order implementation. Compared to the boosted puncture, in this case we see better behaviour close to the puncture (the solution of the 8th order spinning puncture is similar to the boosted case). Far from the puncture the convergence ratio is approximately second order.

As we saw in our third test and in our numerical experiment for a single boosted or spinning puncture, the convergence rate of the high order finite differencing scheme for functions C_0^∞ drops near to $\vec{0}$. This is a well known property of high order finite difference schemes (e.g. [92, 11]). We review some basics of this effect in Appendix C. Nevertheless, as we show in 3.1.2 and in the two-punctures test (see below), the numerical solution produced by our high order implementation seems to be accurate enough to perform numerical evolutions of multiple black holes. Looking at the waveforms, we found that the errors close to the puncture do not modify significantly the convergence during the evolution.

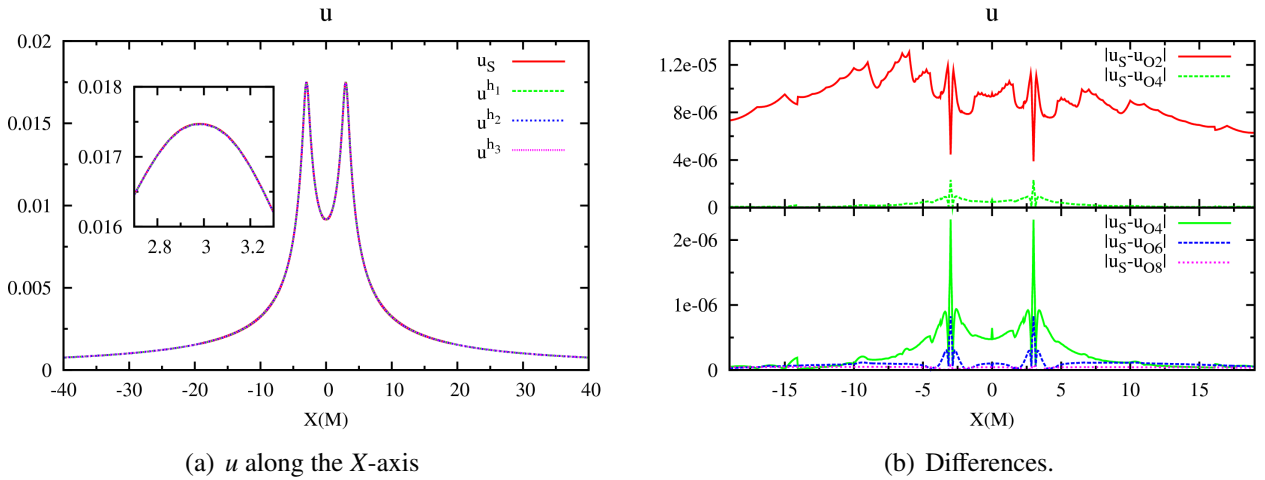
Two-puncture initial data

Figure 2.5: Comparison between the numerical solution of the Hamiltonian constraint calculated using a single-domain spectral method and the high-order multigrid solver. (a) The plot shows u along the X -axis produced by the spectral code (denoted by u_S) and using three resolutions calculated with the eighth order implementation of the multigrid code (labels u^{h_i}). (b) Absolute value of the differences between the numerical solution of u for the second, fourth, sixth, and eighth order finite difference implementation and the spectral solution.

As a test for a binary system we set the parameters for two punctures to $x_1 = -x_2 = 3M$, $P_1^i = -P_2^i = 0.2\delta_2^i M$. This configuration was studied before using a single-domain spectral method [8]. We compared the result of our new code with the solution produced by the spectral solver. For the spectral solution we use $n_A = n_B = 40$ and $n_\phi = 20$ collocation-points (see reference for details about the definition of spectral coordinates (A, B, ϕ)). We calculate the multigrid solution in a cubic domain of length $40M$, 7 levels of refinement and 3 resolutions of $h_1 = (1/16)M$, $h_2 = h_1/2$ and $h_3 = h_1/4$ in the finest level.

Fig. 2.5(a) shows a plot similar to Fig. 5 of [8]. We compare the spectral solution with the eighth order multigrid solution. The fact that the four lines coincide on the scale of the plot (3 resolutions of multigrid and one spectral solution) indicates that the two methods agree with each other on the whole domain. Using the same setting we solve the Hamiltonian constraint with the second, fourth, and sixth order stencil of the multigrid code. Then we use the highly accurate solution of the spectral code as reference to compare with the different orders. As we

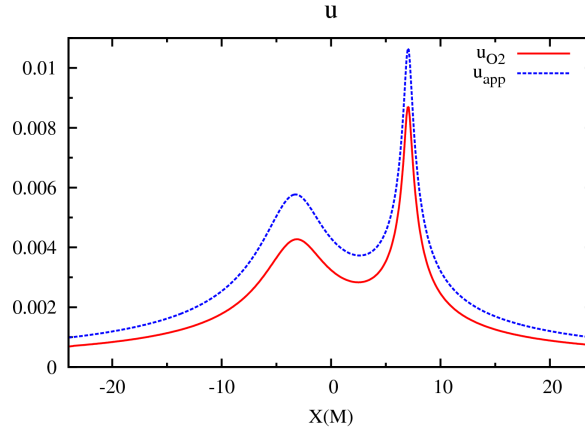


Figure 2.6: Plot of u along X -axis for system 3BH102, comparing the approximate solution with a second order numerical solution. The higher order numerical solutions would not be distinguishable from second order in this plot, compare Fig. 2.2.2.

showed before in the case of a single puncture, the accuracy close to the puncture decreases. However, the comparison with the spectral code (see Fig. 2.5(b)) shows that using high order finite differencing stencils improves the accuracy of the solution.

Three-puncture initial data

In previous work on the numerical evolution of three black holes [42, 94], the Hamiltonian constraint has been specified using an approximate solution (see [94, 86, 51, 58, 59]). We compare our numerical solution with the approximate solution (which we implemented as well) for the set of parameters labelled 3BH102 given in Table I of [42], see our Table 3.1.

In Fig. 2.6 we show a plot of the solution obtained using a cubic domain of length $50M$, a mesh size $h = 0.5M$ in the coarse level and 9 levels of refinement. The approximate solution was calculated in the same numerical grid. The result shows a significant difference between the two methods, and, as we will show later in 3.1.2, that fact leads to a quantitative and qualitative difference for evolutions.

Chapter 3

Numerical evolution of three black holes

3.1 Numerical relativistic three black hole simulations

In the mid 1960's, Hahn and Lindquist started the numerical investigation of colliding black holes [70]. After more than forty years and a series of breakthroughs starting in 2005 [110, 41, 13, 38, 114], the numerical relativity community is now able to produce stable black hole inspiral simulations and to compute gravitational waves signals. The most common formulation used to perform numerical evolutions of black holes is based on the work of Shibata and Nakamura [117], and Baumgarte and Shapiro [16] and is known as the BSSN formulation.

3.1.1 The moving puncture approach

We have performed the three black hole simulations using the BAM code as described in [37, 38], and with the AMSS-NCKU code [43]. BAM uses a sixth order discretization for the spatial derivatives [79] and fourth order accurate integration in time. Initial data are provided by the OLLIPTIC code. Gravitational waves are calculated in the form of the Newman-Penrose scalar Ψ_4 according to the procedure described in Sec. III of [37]. We use the BSSN system together with the 1 + log and gamma freezing coordinate gauges [6, 12, 7] as described in [37] (choosing in particular the parameter $\eta = 2/M$ in the gamma freezing shift condition). All the runs are carried out with the symmetry $(x, y, z) \rightarrow (x, y, -z)$ in order to reduce the computational cost. The Courant factor, $C := \Delta t/h_i$, seems to be an important ingredient to obtain clean

convergence. For long evolutions (evolution time $t > 200$), we set $C = 1/4$, in other cases we use $C = 1/2$.

We provide initial data for evolutions using the AMSS-NCKU in collaboration with Bernd Brügmann and Zhoujian Cao [57]. Later we show the results of the evolution, here we summarise the main features of the code. The AMSS-NCKU code is an extended version of the code described in [43]. Instead of GrACE, the new code includes a driver which combine C++ and FORTRAN 90 to implement moving box style mesh refinement. Regarding the numerical scheme dealing with the interface of neighbour levels, the implementation closely follows the methods described in [37, 135]. AMSS-NCKU can implement both the 6 point buffer zone method [37] and interpolation at each sub-Runge-Kutta step [135]. For simplicity, all simulations presented here use the 6 point buffer zone method. For time evolution, AMSS-NCKU implements a methods of lines with a 4th order Runge-Kutta method. The Sommerfeld boundary condition is implemented with 5th order interpolation.

3.1.2 Mergers and gravitational waves

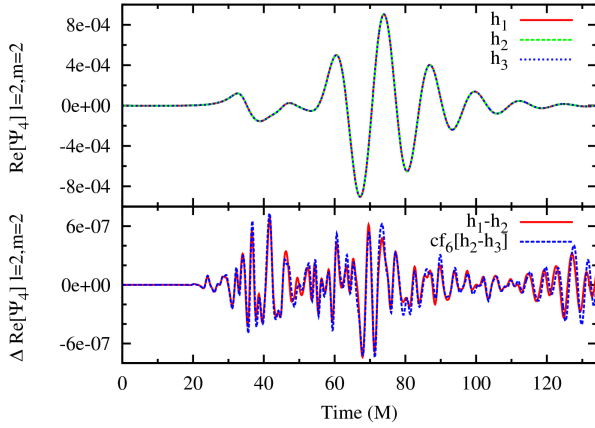
With the BAM code we simulate three black holes with initial parameters as given in Table 3.1. In the first experiments, we focus on runs that use the initial data parameters of runs “3BH1” and “3BH102” in [42]. We evolve this data with both the numerical initial data and the approximate solution to the conformal factor. We compare the puncture tracks and the extracted wave forms with those produced by the AMSS-NCKU code. The puncture tracks give a convenient measure of the black hole motion. It is much more cumbersome to compute the event horizon, which we do for a simple black hole triple in [125].

Analytical approximate and numerical initial data

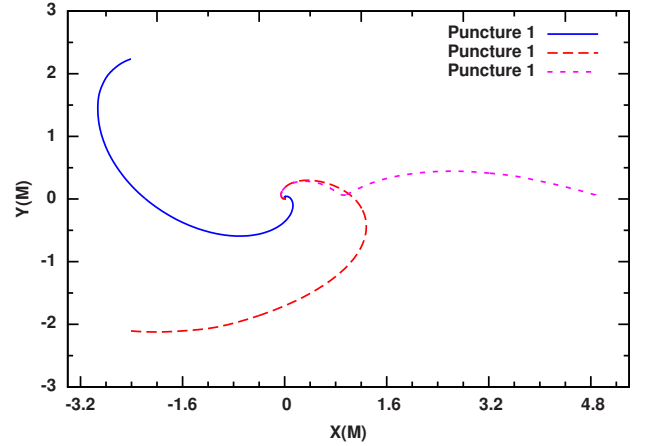
System 3BH1 is a short simulation which is useful for convergence tests. We use our sixth order implementation to calculate initial data, a cubic domain of length $1052M$, 10 levels of refinement and three resolution $h_1 = (125/12)M$, $h_2 = 6h_1/7$ and $h_3 = 2h_1/3$ on the finer level. We have obtained roughly sixth order convergence for the gravitational waveform, as shown in Fig. 3.1(a). Our results show a Ψ_4 waveform similar to that shown in Fig. 16 of [94]. For this evolution, we did not find a significant difference when using approximate initial data or solving

Table 3.1: Initial data parameters

Parameter	3BH1	3BH102	TBHLa	TBHLb	BBH
x_1/M	-2.4085600	-3.5223800	-5.0000000	-5.0000000	0.0000000
y_1/M	2.2341300	2.5850900	8.6602540	8.6602540	3.3941971
p_1^x/M	-0.0460284	0.0782693	-0.2795689	-0.2648550	-0.1270851
p_1^y/M	-0.0126181	-0.0433529	-0.1614092	-0.1529140	0.0000000
m_1/M	0.3152690	0.3175780	0.3152690	0.3152690	0.4792131
x_2/M	-2.4085600	-3.5246200	-5.0000000	-5.0000000	0.0000000
y_2/M	-2.1053400	-2.5850900	-8.6602540	-8.6602540	-3.3941971
p_2^x/M	0.1307260	-0.0782693	0.2795689	0.2648550	0.1270851
p_2^y/M	-0.0126181	-0.0433529	-0.1614092	-0.1529140	0.0000000
m_2/M	0.3152690	0.3175780	0.3152690	0.3152690	0.4792131
x_3/M	4.8735000	7.0447600	10.0000000	10.0000000	...
y_3/M	0.0643941	0.0000000	0.0000000	0.0000000	...
p_3^x/M	-0.0846974	0.0000000	0.0000000	0.0000000	...
p_3^y/M	0.0252361	0.0867057	0.3228184	0.3058280	...
m_3/M	0.3152690	0.3185850	0.3152690	0.3152690	...



(a) Waveform.



(b) Puncture track

Figure 3.1: (a) Real part of Ψ_4 (mode $l = m = 2$) calculated at $r = 40M$ for system 3BH1. The lower panel shows the convergence test for 6th order ($cf_6 = 1.9542$). (b) Trajectory of the punctures.

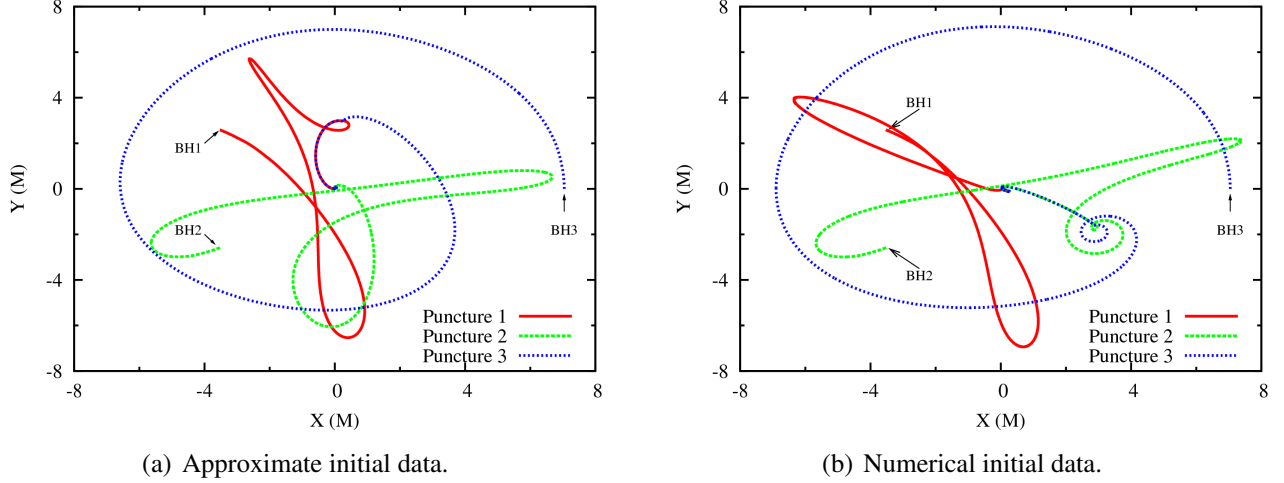


Figure 3.2: Puncture tracks for system 3BH102 using approximate initial data (a), and using the numerical solution of the Hamiltonian constraint with the 8th order multigrid method (b). There is a drastic change in the puncture tracks compared to the evolution of the approximate initial data, in particular the black holes merge in a different order.

the constraint equations numerically.

Our second example is black hole configuration 3BH102, which we consider first for approximate initial data, and later for the numerical solution. This set of parameters is a system which, starting with approximate initial data, leads to trajectories forming a nice figure similar to the Greek letters γ , σ and τ (see Fig. 3.2(a), computed with BAM). Our convergence test for this system shows sixth-order (see Fig. 3.3(a)), with small deviations from second and fourth order which are consistent with the accuracy of the evolution method of our code.

Comparing with Fig. 3 of [42], there is a small but noticeable difference in the puncture tracks of roughly up to $1M$ in the coordinates compared to our results. There are several possible explanations for this difference. Evolutions of multiple black holes are sensitive to small changes in the grid setup and initial data. We tested possible sources of errors, for example introduced by numerical dissipation or finite resolution. Changing these lead to negligible changes in the trajectories on the scale of the plot and do not seem to explain the existing difference. However, since the deviation from [42] does not change the qualitative shape of the tracks, we conclude that we have consistently reproduced that simulation.

We now focus on the evolution of system 3BH102 solving the Hamiltonian constraint with

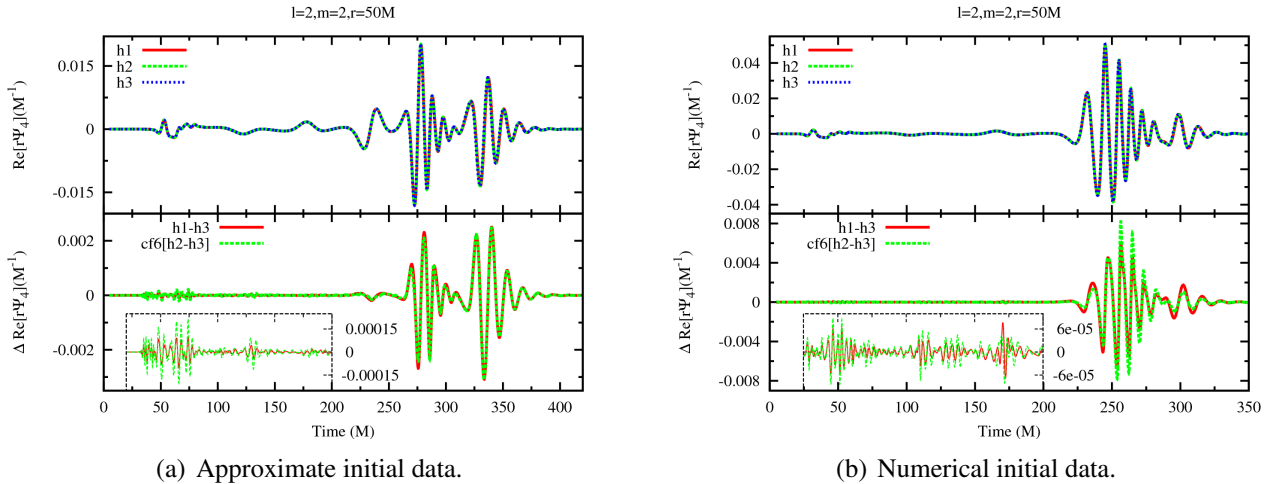


Figure 3.3: Real part of $r\Psi_4$ (mode $l = m = 2$) calculated at $r = 50M$ for system 3BH102 using approximate initial data (a) and using the numerical solution of the Hamiltonian constraint (b). In both cases the upper panel shows the $r\Psi_4$ waveform for 3 resolutions, the bottom plot shows sixth-order convergence scaling with a factor $cf_6 = 1.9542$.

the eighth-order multigrid method. As shown in Sec. 2.2.2, for system 3BH102 the numerical solution of the Hamiltonian constraint differs from the approximate prescription. As a consequence, the trajectories and waveform change. We show the paths followed by the punctures for this case in Fig. 3.2(b). Instead of the grazing collisions of the previous evolution, in this case the black holes with labels 2 and 3 merge after a small inspiral, producing a higher amplitude in the wave. The second merger is almost a head-on collision, which generates a smaller amplitude in the wave. Notice that the order in which the black holes merge differs from the previous evolution.

The Ψ_4 waveform and convergence are shown in Fig. 3.3(b). Note that we see approximately sixth-order convergence in the waveform except for the first merger where the convergence is close to 4th order. Looking at the wave forms, for the approximate initial data Fig. 3.3(a) shows a relatively large burst of “junk”-radiation which does not converge. Solving the Hamiltonian constraint we see a better convergence behaviour, see Fig. 3.3(b). Moreover, the difference in the junk-radiation between resolutions using the approximate initial data is one order of magnitude bigger than solving the Hamiltonian constraint numerically (compare the insets in Fig. 3.3).

In the case of a binary system it is possible to produce the same evolution for numerical and

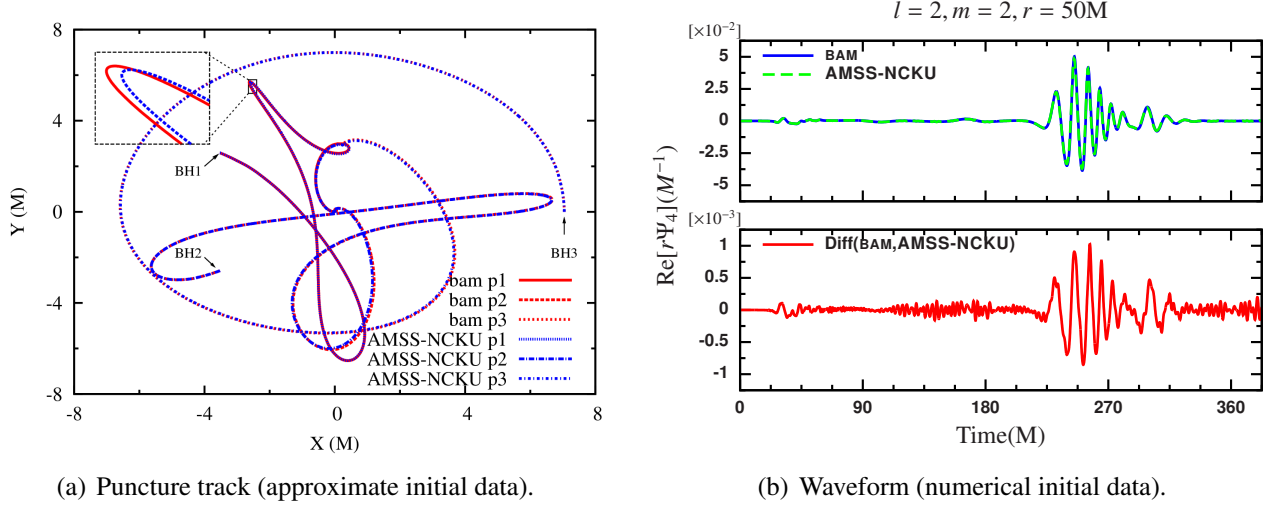


Figure 3.4: Puncture tracks and waveform for system 3BH102 comparing results for the BAM and AMSS-NCKU codes. (a) The difference in the trajectories is small, and the results agree in the general shape. Note that AMSS-NCKU uses fourth-order spatial discretization instead of sixth-order which is implemented in BAM. (b) The waveform shows differences in the phase of about 0.4% and of about 2% in the amplitude.

approximate initial data by adjusting the mass parameter [94]. In the case of three black holes, there does not seem to be a simple procedure to fit the initial parameters in order to reproduce the same trajectory with both types of initial data. We tried changes in the momentum, the mass, and the momentum and mass together, looking at the maximum of the regular part u of the conformal factor in order to reduce the difference between the analytical prescription and the numerical data. The result is not satisfactory, i.e. we did not find a way to change the parameters of the approximate data to better approximate the solution of the Hamiltonian constraint, and the large differences in the puncture tracks could not be removed.

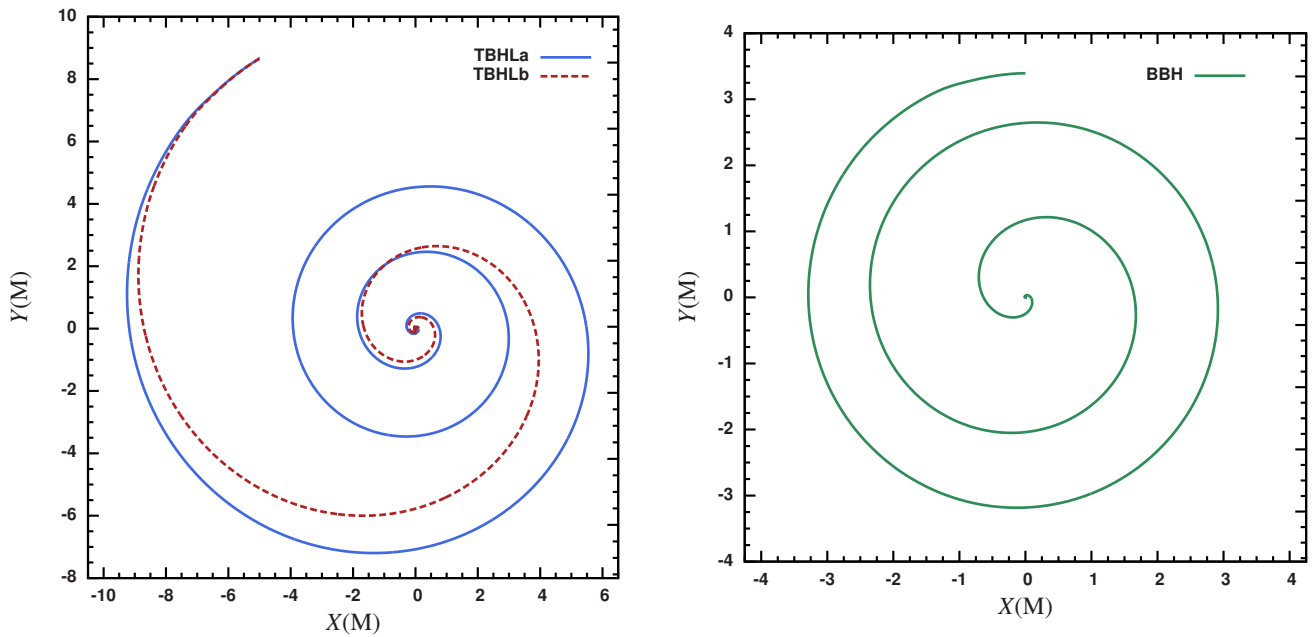
Alternatively, we can compare the paths of the punctures obtained with BAM with those produced by the AMSS-NCKU code. The implementation of the approximate initial data was done independently for the two codes, and in both cases the formula from [94] is used. We see in Fig. 3.4(a) that the results from the two codes agree within a maximum difference of about $0.2M$ in the given coordinates, or 2% with respect to an orbital scale of $10M$. An analysis of the $l = m = 2$ mode of Ψ_4 showed that there are differences in the phase of about 0.4% and of about 2% in the amplitude. Fig. 3.4(b) shows the result of comparing the waveforms for the evolution

which use numerical solution for initial data.

When comparing codes, recall that the BAM evolutions use 6th order spatial differencing, AMSS-NCKU 4th order, and [42] also 4th order for the figures, pointing out that there was little difference to an 8th order run. Our conclusion is that differences due to resolution are small, and they are significantly smaller than the changes introduced by replacing the approximate initial data by a numerical solution of the Hamiltonian constraint.

Looking at the waveforms of Fig. 3.3, is easy to identify a double merger. However, the waveform shown in Fig. 3.1(a) does not exhibit any particular shape that allow us to conclude that there was the presence of a triple merger. In the case of system TBH1 we do not see a double modulation because the bodies merge in a quick secession. To do a comparison between the merger of a binary system and a triple one under similar conditions we setup initial parameters to mimic the inspiral merger of a binary system (see Table 3.1). We use an equal mass system setting in a equilateral triangle. Each body is at $r = 10M$ from the origin. We choose the initial momentum taking as basis the Newtonian momentum of the equivalent Lagrangian system multiplied by 1.05 in order to reproduce an spiral merger. The initial momentum parameters of TBHLb is %5 smaller than TBHLa. The BBH system is an equal mass binary in a quasi-circular orbit studied previously in [37].

In Fig. 3.5 we show the trajectory of one of the punctures. It is clear that any of the two triple configurations is equivalent to the binary system, the initial separation and the path is different. However, the three systems follows a spiral trajectory, so we can try to see general properties of the waves. Fig. 3.6 shows a comparison of the Ψ_4 modes $l = m = 2$ and $l = m = 3$ for the three configurations. First we have to noted the scale in time and in amplitude. The binary system merger earlier than the others because the shorter initial separation, and TBHLb merges earlier than TBHLa because the smaller initial momentum. However, looking at the amplitude of the modes we observe that for the triple systems the contribution of the $l = m = 2$ mode is of the same order (in TBHLa) or smaller (in TBHLb) than the contribution of the mode $l = m = 3$. For the binary system the opposite happens, the contribution of the mode $l = m = 3$ is negligible and in our simulations looks just like numerical noise. From this result we conjecture that the way to identify a triple merger is by the characterisation of the $l = 3$ modes. In the next chapter we explore this idea for the pre-merger phase using post-Newtonian techniques. As we will show a the end of the next chapter, the post-Newtonian simulations also support this hypothesis.



(a) Puncture track for the triple systems TBHLa and TBHLb

(b) Puncture track for the binary system BBH.

Figure 3.5: Trajectory of one of the bodies (puncture 1), for the triple and the binary systems. (a) The punctures in systems TBHLa and TBHLb start in the same position. The initial momentum parameters of TBHLb is %5 smaller than TBHLa. The trajectory of the other two punctures follow the same path as puncture 1 rotated by $2\pi/3$ and $4\pi/3$. (b) Trajectory of puncture 1 for the binary system BBH. The other puncture follows a trajectory which is symmetric respect to the origin.

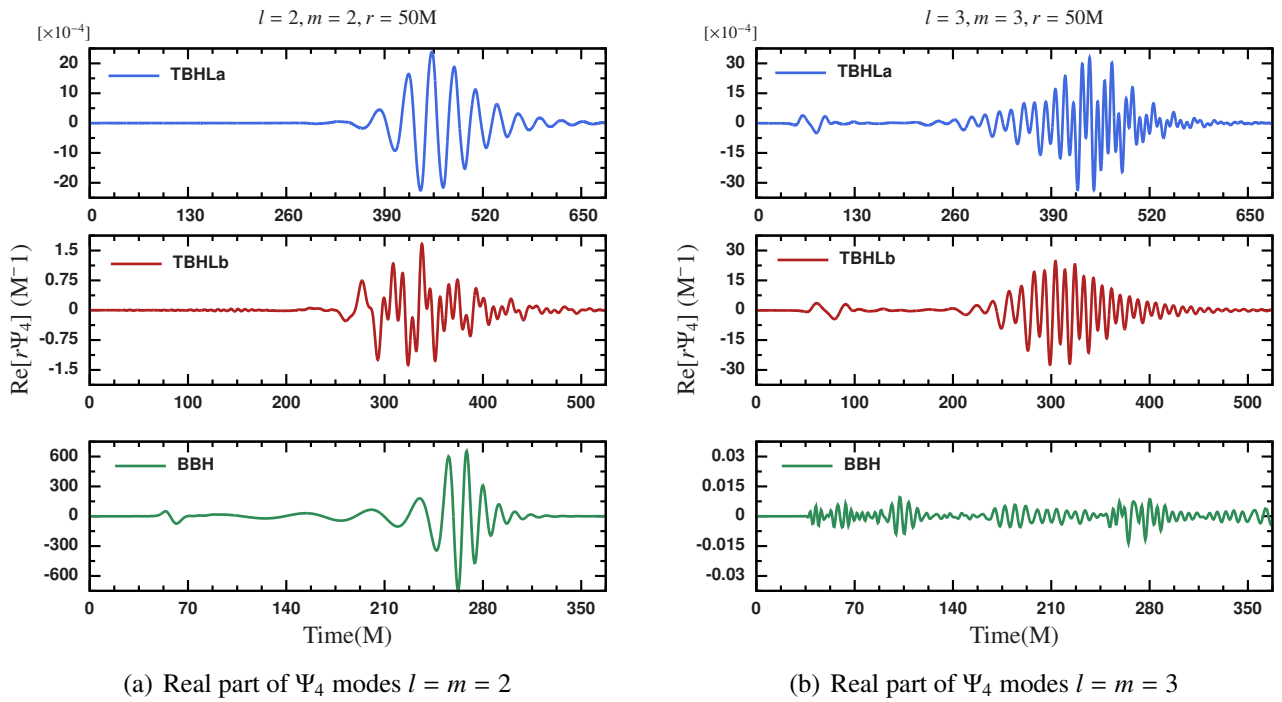


Figure 3.6: Real part of Ψ_4 calculated at $r = 50M$. (a) Comparison of the mode $l = m = 2$ for system TBHLa (top), TBHLb (middle) and BBH (bottom). (b) Comparison of the modes $l = m = 3$ for the same cases of (a). In every case, notice the differences in the scale.

Chapter 4

Post-Newtonian simulation of three black holes

In addition to the full numerical relativistic approach to study the dynamics of three black holes we use post-Newtonian techniques. Using post-Newtonian techniques (PN), it is now possible to describe the dynamics of n compact objects, up to 3.5 PN order (see e.g. [82, 22, 128]). For binary systems the ADM Hamiltonian has been specialised up to 3.5 PN order [85], and for three bodies there are explicit formula up to 2 PN order [47, 113, 93]. In this section we present the post-Newtonian equation of motion for n point-particles derived using Hamiltonian formulation in the ADM gauge. The equations of motion includes the effect of the 2.5 PN gravitational radiation reaction.

Notation and units

We employ the following notation: $\vec{x} = (x_i)$ denotes a point in the three-dimensional Euclidean space \mathbb{R}^3 , letters a, b, \dots are particles labels. We define $\vec{r}_a := \vec{x} - \vec{x}_a$, $r_a := |\vec{r}_a|$, $\hat{n}_a := \vec{r}_a/r_a$; for $a \neq b$, $\vec{r}_{ab} := \vec{x}_a - \vec{x}_b$, $r_{ab} := |\vec{r}_{ab}|$, $\hat{n}_{ab} := \vec{r}_{ab}/r_{ab}$; here $|\cdot|$ denote the length of a vector. The mass parameter of the a th particle is denoted by m_a , with $M = \sum_a m_a$. Summation runs from 1 to 3. The linear momentum vector is denoted by \vec{p}_a . A dot over a symbol, like in $\dot{\vec{x}}$, means the total time derivative, and partial differentiation with respect to x^i is denoted by ∂_i .

In order to simplify the calculations it is useful to define dimensionless variables (see, e.g., [120]). We use as basis quantities for the Newtonian and post-Newtonian calculation the gravi-

tational constant G , the speed of light c and the total mass of the system M . Using derived constants for time $\tau = MG/c^3$, length $l = MG/c^2$, linear momentum $\mathcal{P} = Mc$ and energy $\mathcal{E} = Mc^2$ we construct dimensionless variables. The physical variables are related with the dimensionless variables by mean of a scaling, for example denoting with capital letters the physical variables with the usual dimensions and with lowercase the dimensionless variable we define for a particle a its position $\vec{x}_a := \vec{X}_a/l$, linear momentum $\vec{p}_a := \vec{P}_a/\mathcal{P}$ and mass $m_a = M_a/M$ (notice that $m_a < 1, \forall a$).¹

Hamiltonian formulation

A well known result in the ADM post-Newtonian approach is that it is possible to split the Hamiltonian in a series with coefficients which are inverse powers of the speed of light (see, e.g.,[21, 95])

$$\mathcal{H}_{\leq 2.5} = \mathcal{H}_0 + c^{-2}\mathcal{H}_1 + c^{-4}\mathcal{H}_2 + c^{-5}\mathcal{H}_{2.5}. \quad (4.1)$$

Here each term of the Hamiltonian $c^n\mathcal{H}_{n/2}$, is a quantity with dimension of energy and we write it explicitly in factors of c . The dimensionless Hamiltonian is given by $H_{n/2} = c^n\mathcal{H}_{n/2}/\mathcal{E}$. For each term we calculate the equations of motion

$$(\dot{x}_a^i)_n = \frac{\partial H_n}{\partial p_a^i}, \quad (4.2)$$

$$-(\dot{p}_a^i)_n = \frac{\partial H_n}{\partial x_a^i}. \quad (4.3)$$

where the total equations of motion up to 2.5 PN approximation is

$$\dot{\vec{x}}_a = (\dot{\vec{x}}_a)_0 + (\dot{\vec{x}}_a)_1 + (\dot{\vec{x}}_a)_2 + (\dot{\vec{x}}_a)_{2.5}, \quad (4.4)$$

$$\dot{\vec{p}}_a = (\dot{\vec{p}}_a)_0 + (\dot{\vec{p}}_a)_1 + (\dot{\vec{p}}_a)_2 + (\dot{\vec{p}}_a)_{2.5}. \quad (4.5)$$

¹The system of units used in numerical relativity is the so-called geometric units, in which the speed of light c and Newton's gravitational constant G are taken to be equal to one. In previous sections we use geometric units for the general-relativistic numerical evolutions.

The first term in (4.1) is the Hamiltonian for n particles interacting under Newtonian gravity

$$H_0 = \frac{1}{2} \sum_a^n \frac{\vec{p}_a^2}{m_a} - \frac{1}{2} \sum_{a,b \neq a}^n \frac{m_a m_b}{r_{ab}}, \quad (4.6)$$

with $\vec{p}_a = m_a \dot{\vec{x}}_a$. The inclusion of post-Newtonian corrections are an extra component which enrich the phenomenology of the system.

4.0.3 Post-Newtonian equations of motion up to 2.5 order

The first post-Newtonian correction to the equations of motion is discussed in many papers and textbooks (see e.g., [50, 21]). The three-body Hamiltonian at first and second post-Newtonian order is given in Appendix D. The equations of motion for the first post-Newtonian order are given by (4.2), (4.3) and (D.1). For particle a we obtain

$$(\dot{\vec{x}}_a)_1 = -\frac{\vec{p}_a^2}{2m_a^3} \vec{p}_a - \frac{1}{2} \sum_{b \neq a} \frac{1}{r_{ab}} \left(6 \frac{m_b}{m_a} \vec{p}_a - 7 \vec{p}_b - (\hat{n}_{ab} \cdot \vec{p}_b) \hat{n}_{ab} \right), \quad (4.7)$$

$$\begin{aligned} (\dot{\vec{p}}_a)_1 = & -\frac{1}{2} \sum_{b \neq a} \left[3 \frac{m_b}{m_a} \vec{p}_a^2 + 3 \frac{m_a}{m_b} \vec{p}_b^2 - 7(\vec{p}_a \cdot \vec{p}_b) - 3(\hat{n}_{ab} \cdot \vec{p}_a)(\hat{n}_{ab} \cdot \vec{p}_a) \right] \frac{\hat{n}_{ab}}{r_{ab}^2} \\ & + \sum_{b \neq a} \sum_{c \neq a} \frac{m_a m_b m_c}{r_{ab}^2 r_{ac}} \hat{n}_{ab} + \sum_{b \neq a} \sum_{c \neq b} \frac{m_a m_b m_c}{r_{ab}^2 r_{bc}} \hat{n}_{ab} \\ & - \frac{1}{2} \sum_{a \neq b} \left[\frac{(\hat{n}_{ab} \cdot \vec{p}_b) \vec{p}_a + (\hat{n}_{ab} \cdot \vec{p}_a) \vec{p}_b}{r_{ab}^2} \right]. \end{aligned} \quad (4.8)$$

For the second post-Newtonian approximation the equation of motion are calculated using (4.2), (4.3) and (D.2). For brevity we do not display the explicit equations.

We follow the procedure given in [82, 85] to obtain equations of motions from the 2.5 PN Hamiltonian in the ADM gauge. The general 2.5 PN Hamiltonian is

$$H_{2.5} = \frac{1}{45} \dot{\chi}_{(4)ij}(\vec{x}_{a'}, \vec{p}_{a'}; t) \chi_{(4)ij}(\vec{x}_a, \vec{p}_a), \quad (4.9)$$

where is defined the auxiliary function

$$\chi_{(4)ij}(\vec{x}_a, \vec{p}_a) := \sum_a \frac{2}{m_a} (\vec{p}_a^2 \delta_{ij} - 3p_{ai}p_{aj}) + \sum_a \sum_{b \neq a} \frac{m_a m_b}{r_{ab}} (3n_{abi}n_{abj} - \delta_{ij}).$$

Notice that our expressions contain different factors than [82, 85] due to a different choice of units. The explicitly form of the derivative in (4.9) is

$$\begin{aligned} \dot{\chi}_{(4)ij}(\vec{x}_{a'}, \vec{p}_{a'}) &= \sum_{a'} \frac{2}{m_{a'}} \left[2(\dot{\vec{p}}_{a'} \cdot \vec{p}_{a'}) \delta_{ij} - 3(\dot{p}_{a'i} p_{a'j} + p_{a'i} \dot{p}_{a'j}) \right] \\ &+ \sum_{a'} \sum_{b' \neq a'} \frac{m_{a'} m_{b'}}{r_{a'b'}^2} \left[3(\dot{r}_{a'b'i} n_{a'b'j} + n_{a'b'i} \dot{r}_{a'b'j}) \right. \\ &\left. + (\dot{\hat{n}}_{a'b'} \cdot \dot{\vec{r}}_{a'b'}) (\delta_{ij} - 9n_{a'b'i} n_{a'b'j}) \right]. \end{aligned} \quad (4.10)$$

We denote with primed quantities the retarded variables. The position and momenta appearing in Eq. (4.10) are not affected by the derivative operators given by (4.2) and (4.3), and only after calculating those derivatives we identify positions and momenta inside and outside the transverse-traceless variables (i.e. the primed and unprimed quantities). We replace the time derivatives of the primed coordinates and position given in Eq. (4.10) by the 1PN equations of motion Eqs. (4.7) and (4.8).

The equations of motion for 2.5 PN are given in a short representation by

$$(\dot{\vec{x}}_a)_{2.5} = \frac{1}{45} \dot{\chi}_{(4)ij}(\vec{x}_a, \vec{p}_a; (\dot{\vec{x}}_a)_1, (\dot{\vec{p}}_a)_1, t) \frac{\partial}{\partial \vec{p}_a} \chi_{(4)ij}(\vec{x}_a, \vec{p}_a), \quad (4.11)$$

$$(\dot{\vec{p}}_a)_{2.5} = -\frac{1}{45} \dot{\chi}_{(4)ij}(\vec{x}_a, \vec{p}_a; (\dot{\vec{x}}_a)_1, (\dot{\vec{p}}_a)_1, t) \frac{\partial}{\partial \vec{x}_a} \chi_{(4)ij}(\vec{x}_a, \vec{p}_a). \quad (4.12)$$

Given initial values for \vec{x}_a and \vec{p}_a of each particle it is possible to integrate numerically the resulting equations of motion.

4.0.4 Gravitational radiation in the linear regime

We consider linearised gravitational waves calculated using trajectories which contain post-Newtonian corrections. We compute the gravitational waveforms for a given observational direction and alternatively we calculate the multipole decomposition which allow us to recon-

struct the waves for an arbitrary direction. The inclusion of post-Newtonian corrections to the gravitational waveforms is a topic for future research in the three-compact-body problem.

Quadrupole and octupole formulas

Here we summarise the formulas for quadrupole and octupole mass radiation and current quadrupole radiation (for a review see e.g. [95, 53]). The second and third mass momentum are define by

$$M^{ij}(t) = \int T^{00}(\vec{x}, t) x^i x^j d^3x, \quad (4.13)$$

$$M^{ijk}(t) = \int T^{00}(\vec{x}, t) x^i x^j x^k d^3x. \quad (4.14)$$

The third momenta of the momentum density is

$$P^{i,jk}(t) = \int T^{0i}(\vec{x}, t) x^j x^k d^3x. \quad (4.15)$$

For n point particles

$$T^{\mu\nu}(\vec{x}, t) = \sum_a \frac{p_a^\mu p_a^\nu}{\gamma_a m_a} \delta^3(\vec{x} - \vec{x}_a(t)), \quad (4.16)$$

where $\gamma_a := (1 - \vec{p}_a^2)^{-1/2}$ is the Lorentz factor, and $p_a^\mu := \gamma_a(m_a, \vec{p}_a)$ is the four-momentum. In this case Eqs (4.13)-(4.15) reduce to

$$M^{ij}(t) = \sum_a \gamma_a m_a x_a^i(t) x_a^j(t), \quad (4.17)$$

$$M^{ijk}(t) = \sum_a \gamma_a m_a x_a^i(t) x_a^j(t) x_a^k(t), \quad (4.18)$$

$$P^{i,jk}(t) = \sum_a p_a^i(t) x_a^j(t) x_a^k(t). \quad (4.19)$$

The mass quadrupole and octupole moment are given by:

$$\begin{aligned} Q^{ij}(t) &= M^{ij} - \frac{1}{3} \delta^{ij} M^{kk}, \\ \mathcal{O}^{ijk}(t) &= M^{ijk} - \frac{1}{5} (\delta^{ij} M^{llk} + \delta^{ik} M^{lkl} + \delta^{jk} M^{ill}), \end{aligned}$$

where repeated indices means summation from 1 to 3. The current quadrupole is given by

$$C^{k,lm}(t) = P^{k,lm} + P^{l,km} - 2P^{m,kl}. \quad (4.20)$$

A projection tensor in the normal plane of propagation \hat{n} of the wave is defined by

$$P_{ij} := \delta_{ij} - n_i n_j, \quad (4.21)$$

$$\Lambda_{ijkl}(\hat{n}) := P_{ik} P_{jl} - \frac{1}{2} P_{ij} P_{kl}. \quad (4.22)$$

The mass quadrupole and octupole waveform are given by

$$h_{ij}^{TT}(\vec{x}, t)_{MQ} = \frac{2}{r} \Lambda_{ijkl}(\hat{n}) \ddot{Q}^{kl}(t-r), \quad (4.23)$$

$$h_{ij}^{TT}(\vec{x}, t)_{MO} = \frac{2}{3r} \Lambda_{ijkl}(\hat{n}) n_m \ddot{\ddot{O}}^{klm}(t-r), \quad (4.24)$$

and the current quadrupole contribution to the waveform is

$$h_{ij}^{TT}(\vec{x}, t)_{CQ} = \frac{4}{3r} \Lambda_{ijkl}(\hat{n}) n_m \ddot{C}^{k,lm}. \quad (4.25)$$

We perform the standard multipole moments decomposition using standard spherical harmonics (see e.g., [95, 126]):

$$Y^{lm}(\theta, \phi) = \begin{cases} C^{lm} (e^{i\phi} \sin \theta)^m \sum_{k=0}^{[(l-m)/2]} a_k^{lm} (\cos \theta)^{l-m-2k} & \text{for } m \geq 0 \\ (-1)^m \bar{Y}^{l,-m} & \text{for } m < 0 \end{cases} \quad (4.26)$$

The notation $[(l-m)/2]$ denotes the largest integer smaller or equal to $(l-m)/2$, the over-line refers to the complex conjugate, and the coefficients are given by

$$C^{lm} = (-1)^m \left(\frac{2l+1}{4\pi} \frac{(l-m)!}{(l+m)!} \right)^{1/2}, \quad (4.27)$$

$$a_k^{lm} = \frac{(-1)^k (2l-2k)!}{2^l k! (l-k)! (l-m-2k)!}. \quad (4.28)$$

The spherical components are given by

$$\mathbb{Q}_{l=2}^m = \ddot{Q}^{ij} \int_0^{2\pi} \int_0^\pi n_i n_j \bar{Y}^{2m} d\Omega \quad \text{for } m \in \{-2, \dots, 2\}, \quad (4.29)$$

$$\mathbb{Q}_{l=3}^m = \dot{S}^{ijk} \int_0^{2\pi} \int_0^\pi n_i n_j n_k \bar{Y}^{2m} d\Omega \quad \text{for } m \in \{-3, \dots, 3\}. \quad (4.30)$$

Here $\hat{n} = (\sin \theta \cos \phi, \sin \theta \sin \phi, \cos \theta)$, $d\Omega = \sin \theta d\theta d\phi$ and S^{ijk} join up the current quadrupole and the mass octupole contributions. For point particles S^{ijk} is given by

$$S^{ijk} = \sum_a \frac{p_a^i p_a^j}{\gamma_a m_a} x_a^k. \quad (4.31)$$

It is possible to reconstruct the waveforms for a given direction using the spherical components

$$h_{ij}^{TT}(\vec{x}, t)_{MQ} = \frac{2}{r} \Lambda_{ijkl}(\hat{n}) \sum_{m=2}^2 \mathbb{Q}_{l=2}^m(t-r) \mathcal{Y}_{l=2,m}^{kl}, \quad (4.32)$$

$$h_{ij}^{TT}(\vec{x}, t)_{MO+CQ} = \frac{2}{3r} \Lambda_{ijkl}(\hat{n}) n_m \sum_{m=2}^2 \mathbb{Q}_{l=3}^m(t-r) \mathcal{Y}_{l=3,m}^{klm}, \quad (4.33)$$

where $\mathcal{Y}_{l=2,m}^{kl}$ and $\mathcal{Y}_{l=3,m}^{klm}$ are a basis of symmetric trace-free tensors (see [126] for a definition valid for an arbitrary SFT- l tensors with arbitrary number for index). Using the identities

$$\mathcal{Y}_{l=2,m}^{ij} \int n_i n_j n^a n^b d\Omega = \int n^a n^b Y^{2m} d\Omega, \quad (4.34)$$

$$\mathcal{Y}_{l=3,m}^{ijk} \int n_i n_j n_k n^a n^b n^c d\Omega = \int n^a n^b n^c Y^{3m} d\Omega, \quad (4.35)$$

together with²

$$\int n_{i_1} \cdots n_{i_{2l}} d\Omega = \frac{4\pi}{(2l+1)!!} (\delta_{i_1 i_2} \delta_{i_3 i_4} \cdots \delta_{i_{2l-1} i_{2l}} + \dots), \quad (4.36)$$

we can read off the values of $\mathcal{Y}_{l=2,m}^{kl}$ and $\mathcal{Y}_{l=3,m}^{klm}$

²In 4.36 the final dots denotes all possible pairing of indices

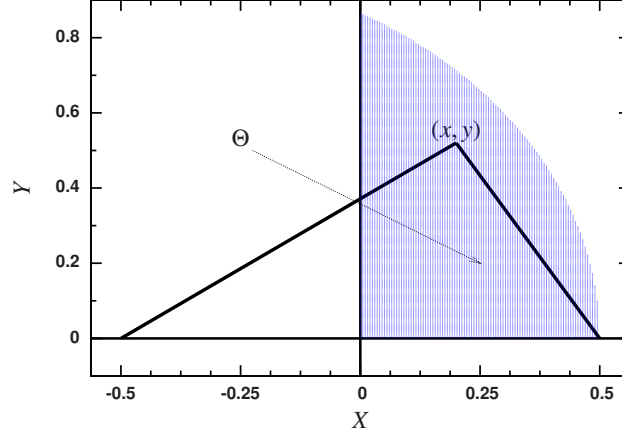


Figure 4.1: Agekyan-Anosova map: The two bodies with larger separation are placed on the horizontal axis one unit apart, the one which is further to the third in the negative part and the third body is at (x, y) , inside a curved triangle.

4.1 Simulations and results

From the Newtonian Hamiltonian (4.6) and the equations of motion (4.2) and (4.3) it is easy to show that for $\lambda \in \mathbb{R}^+$ and given $\vec{x}_1(t)$, $\vec{x}_2(t)$ and $\vec{x}_3(t)$ which represent a solution of the three-body problem, then $\lambda^2 \vec{x}_1(\lambda^3 t)$, $\lambda^2 \vec{x}_2(\lambda^3 t)$ and $\lambda^2 \vec{x}_3(\lambda^3 t)$ is a solution to the same problem. As consequence in the Newtonian case lengths scale as $l' \rightarrow \lambda^2 l$, time as $t' \rightarrow \lambda^3 t$, energy as $E' \rightarrow \lambda^{-2} E$, momentum as $p' \rightarrow \lambda^{-1} p$ and angular momentum as $L' \rightarrow \lambda L$. The scaling properties of the three-body problem allow us to reduce the set of initial configurations into a subset. One example is the Agekyan-Anosova (AA) map [3, 132, 88], where two bodies are placed on the horizontal axis one unit apart and the third body is at (x, y) coordinates, inside a region

$$\Theta = \{(x, y) \in \mathbb{R}^2 \mid 0 \leq x \leq 1/2, y \geq 0, y^2 \leq 1 - (x + 1/2)^2\}, \quad (4.37)$$

which is a curved triangle (see Fig 4.1). For initial position and momentum $(\vec{x}_1, \vec{p}_1, \vec{x}_2, \vec{p}_2, \vec{x}_3, \vec{p}_3) \in \mathbb{R}^{18}$, we can associate the initial configuration to a point in the subset $(x, y, \vec{p}_1, \vec{p}_2, \vec{p}_3) \in \Theta \times \mathbb{R}^9$. The AA map gives a unique description of the three-body configuration for several “length scales”.

If we include post-Newtonian corrections it is not always possible to scale the solutions. There is evidence about scaling properties in the case of first and second post-Newtonian cor-

rections [93]³. However, the inclusion of higher post-Newtonian corrections, particularly gravitational radiation, breaks the scaling properties. Full numerical relativistic simulations confirm that close to the merger phase the Newtonian dynamics and the General relativistic one produce different trajectories for the same initial parameters [94]. However, the main difference is the damping due to gravitational radiation and as consequence the merger of the black holes.

4.1.1 Numerical integration

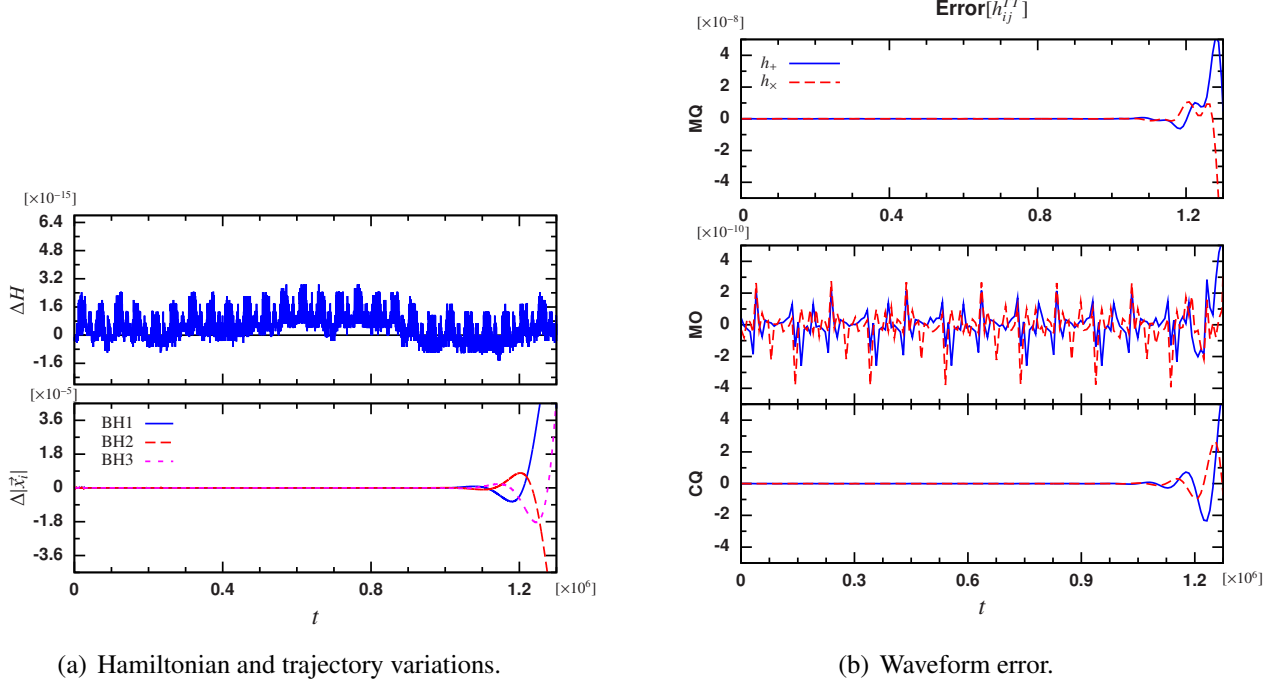
We solve the equations of motion numerically using `MATHEMATICA 7.0` [134]. We use the built-in low-level functions of `NDSolve` routine with a “double step” method using as sub-algorithm an “explicit mid-point” method. We divided a long simulation in sub-steps in order to store the result from time to time and avoid saturating the RAM. With this approach we can produce accurate numerical solutions of the equations of motion. An important issue in the numerical integration of a three-body system arises when two of the bodies come very close each other. In the case of adaptive step size methods its is necessary to reduce the step size in order to resolve properly the orbits in the close interaction. An usual approach to cure this problem is to perform a regularisation of the equations of motion, see e.g., [39, 73, 100, 101, 102] and references therein. However, in our simulations we include a different criteria. We monitor the absolute value of each conservative part of the Hamiltonian (4.1) relative to the sum of the absolute values

$$H_i^{\%} := 100 \left(\frac{|H_i|}{|H_0| + |H_1| + |H_2|} \right). \quad (4.38)$$

We stop our simulation when the contribution of the first post-Newtonian correction is larger than 10%. We perform several tests to estimate the numerical errors. Here we summarise the results of these tests.

We use the Lagrangian equilateral triangle solution to compare the numerical with an analytical solution. In Lagrange’s solution every body is sitting in one corner of an equilateral triangle (see e.g., [60]). We set the side of such triangle to $L = 1000$, the mass ratio to 1:2:3 and the eccentricity to zero, then every body follows a circular orbit around the center of mass. The solution in this case is not stable [132], however for circular orbits we can compute the

³In [93] Moore’s figure-eight [105] was studied using first and second Post-Newtonian approximations. The numerical experiments show that the scaling properties of the initial momentum are well approximated by a inverse power series.



(a) Hamiltonian and trajectory variations.

(b) Waveform error.

Figure 4.2: Test using Lagrange's equilateral solution of the Newtonian three body problem. (a) shows the relative variation of the Hamiltonian (top) and the relative change in the orbits (bottom). (b) shows the error for the mass quadrupole **MQ** (top), mass octupole **MO** (middle) and the current quadrupole **CQ** (bottom).

waveforms. Then we can compare the waveforms with the analytical expressions.

In Fig. 4.2(a), we show the relative variation of the Hamiltonian

$$\Delta H := \frac{H(0) - H(t)}{H(0)}, \quad (4.39)$$

and for each body the relative variation of the position respect to the center of mass. The variation of the Hamiltonian is small (close to machine accuracy), however the error in the orbits grow fast breaking the regular trajectory. In this case, after seven orbits the numerical solution fail. The waves exhibit a similar behaviour. In Fig. 4.2(b), we show the error for each polarisation of the waveforms (4.23)-(4.25). The error is defined as the difference between the analytical expression and the numerical calculation. The mass octupole exhibit a noisy error due to the complicate of the analytical expression.

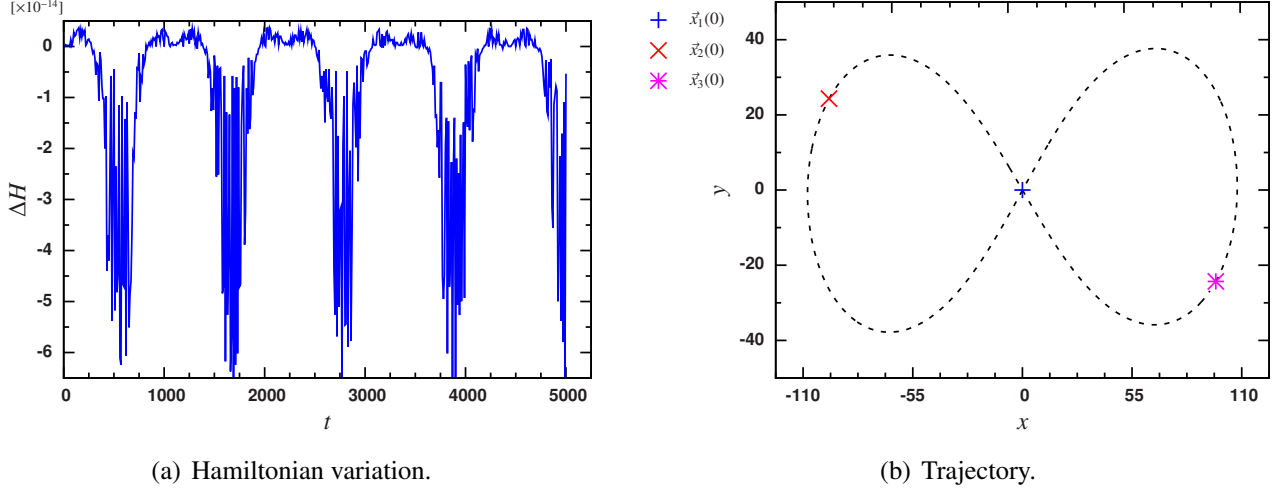


Figure 4.3: Moore’s figure eight solution. (a) Relative variation of the Hamiltonian for a solution which includes 2PN corrections. (b) Initial position (marks +, \times and $*$) and path followed by the bodies (dashed line).

We reproduce a few of the result from [93], specifically the simulation of the equal-mass Moore’s figure eight which includes first and second post-Newtonian corrections. Our implementation seems to be more accurate, we obtain variations on the Hamiltonian of 10^{-14} (see Fig. 4.3(a)), instead previous results shown a variation of 10^{-5} (compare Fig. 6 of [93]).

We tested our n -body 2.5 PN equations of motions for the case $n = 2$, i.e, for binary systems. The variation of the semi-major axis and eccentricity of a binary system due to the gravitational radiation is given by [108]

$$\frac{da}{dt} = -\frac{64}{5} \frac{m_1 m_2}{a^3 (1 - e^2)^{7/2}} \left(1 + \frac{73}{24} e^2 + \frac{37}{96} e^4 \right), \quad (4.40)$$

$$\frac{de}{dt} = -\frac{304}{15} \frac{m_1 m_2}{a^4 (1 - e^2)^{5/2}} \left(e + \frac{121}{304} e^3 \right). \quad (4.41)$$

We tested the 2.5 PN equations of motion (4.11) and (4.12) by comparison with direct numerical integration of the equations (4.40) and (4.41). We did the test for two different binaries, one with initial eccentricity $e_0 = 0.1$ and one with $e_0 = 0.5$. In both cases we set $m_1 = 2m_2$, $a_0 = 160$. The numerical integration of the 2.5 PN equations agree very well with the result provided by the numerical integration of (4.40) and (4.41). We calculate the eccentricity of our orbits with

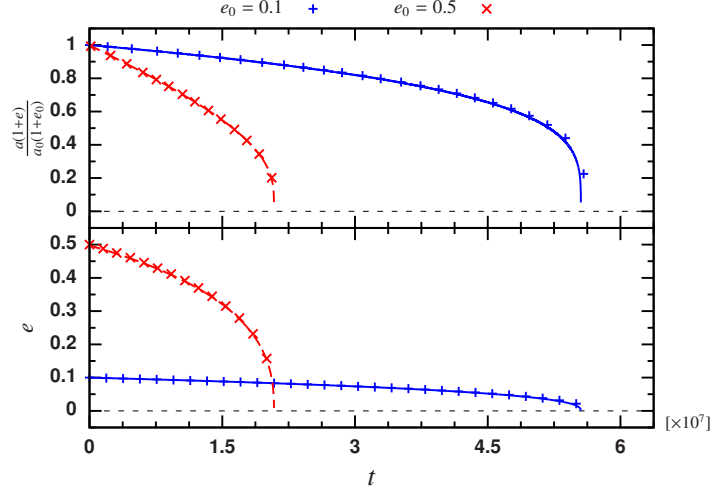


Figure 4.4: Binary system with 2.5 PN radiation. Top: Relative variation of the apoapsis of the two bodies. Bottom: eccentricity variation; comparison of our numerical result (solid and dashed lines) with the numerical integration of (4.40) and (4.41) (marks + and \times) for two initial eccentricities.

the Newtonian formula

$$e = \sqrt{1 + \frac{2l^2 H_c}{(m_1 m_2)^3}}, \quad (4.42)$$

where l is the magnitude of the total angular momentum and H_c is the value of the conservative part of the Hamiltonian. The apoapsis⁴ is related to the semi-major axis by $r_{\text{ap}} = a(1 + e)$. For simplicity we compare in upper panel of Fig. 4.4 the relative variation of r_{ap} respect to its initial value and in the lower panel the variation of the eccentricity.

In order to test the script for long evolution of three bodies we use Hénon's Criss-cross solution [75, 105, 106]. This solution is stable with respect to a wide range of perturbations [104]. We evolve the equal mass Criss-cross solution with $M = 200 M_\odot$ for around 10^3 orbits, and initial parameters ad-hoc for our system of units

$$\begin{aligned} \vec{x}_1(0) &= 1.07590\lambda^2 \hat{x}, & \vec{p}_1(0) &= 3^{-3/2} \cdot 0.19509\lambda^{-1} \hat{y} \\ \vec{x}_2(0) &= -0.07095\lambda^2 \hat{x}, & \vec{p}_2(0) &= 3^{-3/2} \cdot 1.23187\lambda^{-1} \hat{y} \\ \vec{x}_3(0) &= -1.00496\lambda^2 \hat{x}, & \vec{p}_3(0) &= 3^{-3/2} \cdot 0.19509\lambda^{-1} \hat{y}, \end{aligned}$$

⁴The apoapsis is the maximum separation of the two bodies.

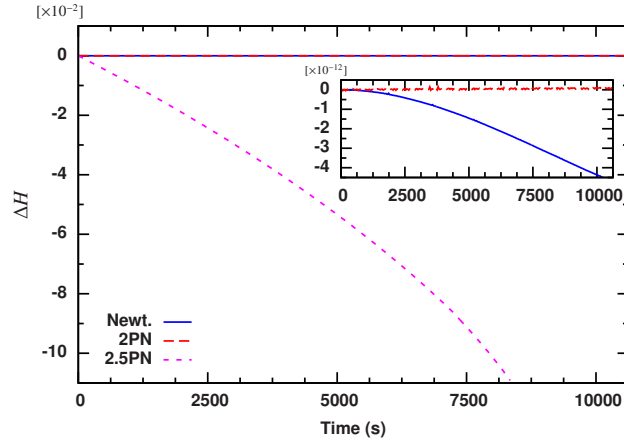


Figure 4.5: Hénon Criss-cross solution for Newtonian, 2 and 2.5 PN dynamics. The main panel shows the relative variation of the Hamiltonian for the three cases. The inset shows only the conservative systems (Newtonian and 2 PN).

where \hat{x} , \hat{y} and \hat{z} are the unitary basis vectors in Cartesian coordinates, and λ is a scaling factor (for our simulation $\lambda = 10$). In Fig. 4.5 we plot the relative variation of the Hamiltonian for the evolution using a Newtonian potential and the corresponding Hamiltonian variation for evolutions which includes 2 and 2.5 PN corrections. As is expected the variation of the Hamiltonian in the 2.5 PN case is huge in comparison with the conservative case and the bodies separate after around $t = 7825$ (s). The inner panel in Fig. 4.5 shows a detail of the conservative part. In this case the 2.5 PN dynamics shows better conservation of the Hamiltonian in contrast to the Newtonian case which has a variation on the Hamiltonian of around 4×10^{-12} .

We confirm that the system is stable even after the inclusion of 2 and 2.5 PN corrections, see Fig. 4.6. In the Newtonian case the accumulation of numerical errors and probably a round-off in the initial parameters lead to a small variation of the orbits. The basic shape of the Criss-cross figure suffers a small rotation. The 2 PN correction includes the effect of precession in the orbits, the original figure spin many times around the origin preserving the same shape. The inclusion of gravitational radiation via the 2.5 PN corrections makes a stronger effect in the orbits, slowly deforming the original figure. The body in the circular-like orbit has a significant reduction on the orbital radius, the two other bodies follow at the end a triangular-like orbit with narrow corners.

We use also the Newtonian Hénon Criss-cross solution for a performance and accuracy test.

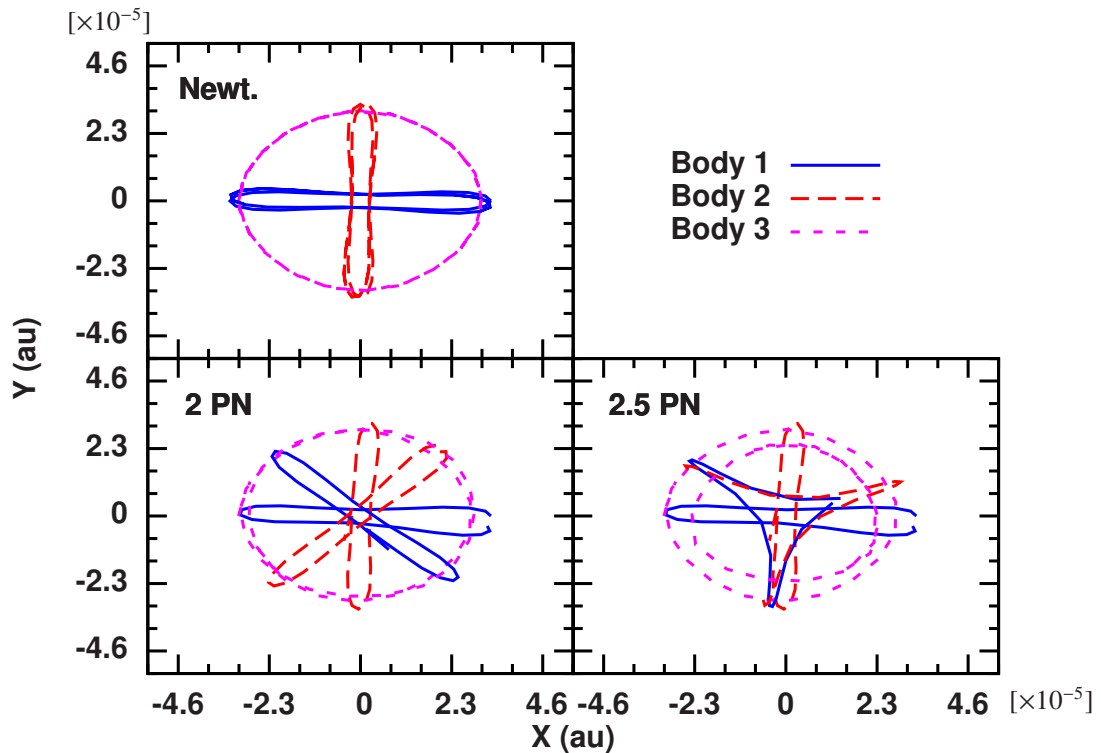


Figure 4.6: Hénon Criss-cross solution for Newtonian, 2 and 2.5 PN dynamics. First and last orbits. In the Newtonian dynamics the orbits don't show a significant change. For dynamics including 2 PN corrections the orbits suffer the expected precession. For the dynamics which include 2.5 PN corrections the gravitational radiation produce a significant change in the orbits which finally break the system.

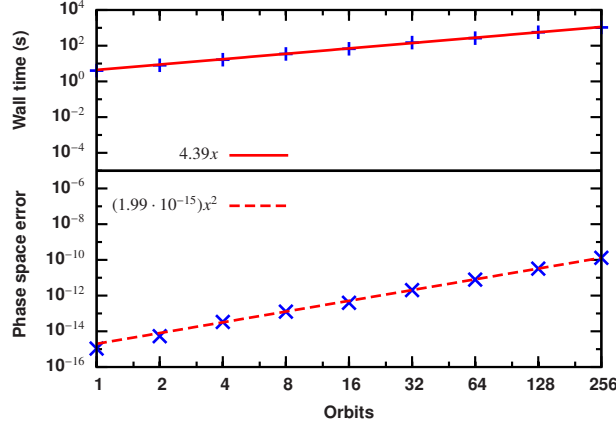


Figure 4.7: Performance and accuracy of the script solving Hénon Criss-cross solution of the Newtonian three-body problem. Top: We fit a linear function $f(x) = 4.39x$ (solid line) to the wall time as function of the number of orbits which represent very well the performance of the script (marks +). Bottom: Estimation of the propagation of the error by time reversibility of the orbits (marks \times). In this case we fit a parabolic function $f(x) = 1.99 \cdot 10^{-15}x^2$ (dashed line).

The performance test consisted on the measurement of the wall time for 9 evolutions. We solve the system in a progression of $1, 2, \dots, 2^8$ orbits. The upper panel of Fig. 4.7 shows the result where we found that the performance is well described by a linear function $f(x) = ax$ with a slope of $a = 4.39 \pm 0.05$. The accuracy test is based on the time reversibility of the orbits. For the same set of runs we solve the system backward in time starting with the last position of each particle but replacing every linear momentum for its opposite value. This process was done in run-time avoiding to reload the parameters. As measurement of the error we compute the variation on the phase space of the initial position and momentum respect to the final position and momentum of the backward evolution

$$(\Delta L_{\text{ps}})^2 := \left[\frac{\sum_a |\vec{x}_a^+(0) - \vec{x}_a^-(t_f)|}{\sum_a |\vec{x}_a^+(0)|} \right]^2 + \left[\frac{\sum_a |\vec{p}_a^+(0) + \vec{p}_a^-(t_f)|}{\sum_a |\vec{p}_a^+(0)|} \right]^2, \quad (4.43)$$

where $\vec{x}_a^+(0)$ and $\vec{p}_a^+(0)$ are the initial position and momentum of the particles (with this data we evolve forward), $\vec{x}_a^-(t_f)$ and $\vec{p}_a^-(t_f)$ are the final position and momentum of the backward evolution. In the case of infinite precision the bodies should retrace their trajectories exactly and the variation should be zero. For a numerical solution there are small differences which

accumulate for each time step, then for the computation in one direction we expect the error to be half of the variation of the cyclic calculation. In the lower panel of Fig. 4.7 we show the result. In this case the *phase space error*⁵ is well represented by a quadratic function $f(x) = ax^2$ with $a = 1.99 \cdot 10^{-15} \pm 8.16 \cdot 10^{-17}$.

The performance tests are representative for the Newtonian case. Including higher PN correction would lead to a different results. The post-Newtonian equations of motion contain many more terms than the Newtonian case, which significant increase in computational cost for a given accuracy. However, we expect the same functional behaviour, the computational time growing linearly respect to the number of orbits and the error accumulating quadratically.

4.1.2 Strong perturbation of a binary system

Here we consider the strong perturbation on the dynamics and waveform of a binary black hole system due to a third smaller black hole. We take all PN corrections up to 2.5 PN for the three bodies. This approach gives us a good description of the third body orbiting close to the binary. However, the computational cost of each simulation increases respect to the Newtonian simulations avoiding the possibility to produce a set of runs necessary to do a systematic statistics of the system. Nevertheless, we selected a representative case in order to try to identify key properties.

We study a *Jacobian system*⁶ with mass ratio 10:20:1. The inner binary system has initial semi-major axis $a_b(0) = 160$ and eccentricity $e_b(0) = 0$.⁷ We consider the third compact body and the center of mass of the inner binary as a new binary (we will refer to it as the external binary). The external binary has initial semi-major axis $a_3(0) = 10000$ and initial eccentricity $e_3(0) = 0$. The bodies start from a configuration where the apoapsis of the inner binary is perpendicular to the apoapsis of the external binary (see Fig. 4.8(b)).

We denote the inclination angle between the osculating orbital planes Π_{in} and Π_{out} by i (see Fig. 4.8(b)). The behaviour of the Hamiltonian is similar in every case. The conservative part of the Hamiltonian decreases relatively slowly during most of the simulation. However, when the

⁵We define the phase space error as $\Delta L_{\text{ps}}/2$.

⁶In a Jacobian system the three-body configuration is composed of two parts, a clearly defined binary and a third body orbiting faraway. We will refer to this kind of systems as hierarchical as well.

⁷We set the initial parameters considering only the Newtonian dynamics, particularly the eccentricity refers to the Newtonian case.

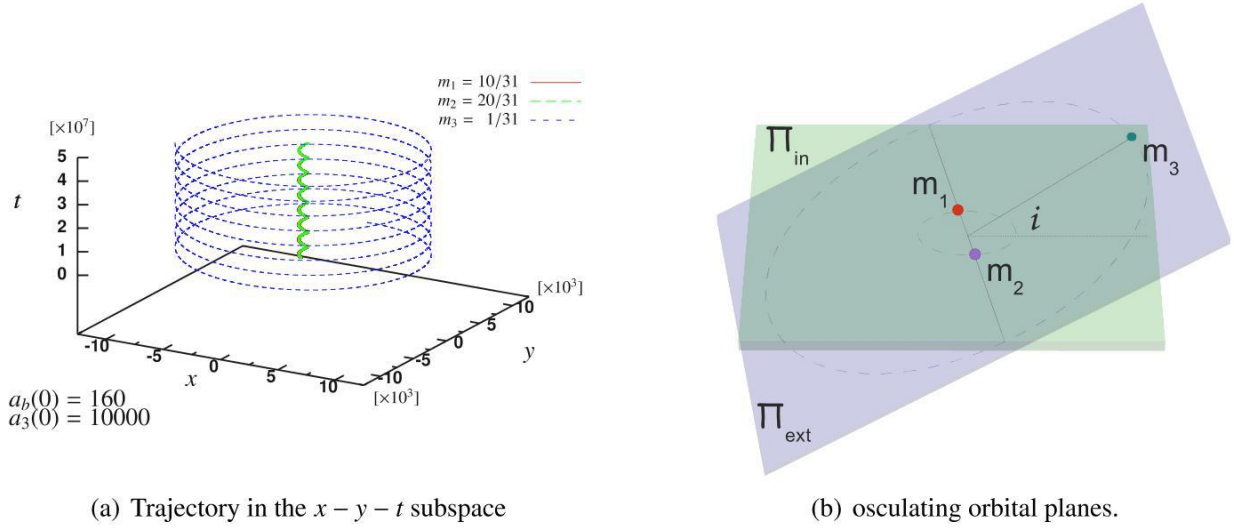


Figure 4.8: Hierarchical system formed by a binary system with a lighter body orbiting faraway. (a) The plot shows the trajectory in the $x-y-t$ subspace. The helix is the perturbed inner binary system. (b) The osculating orbital planes Π_{in} and Π_{out} for inner and outer binary orbits. The two planes are inclined by angle i .

system approaches to the merger phase, the Hamiltonian decreases fast (see Fig. 4.9(a)). As we mention before, the simulations are finished when the contribution of the first post-Newtonian correction becomes larger than 10%. We consider that instant the time when the merger phase start.

In the case of planar motion $i = 0$ we did a comparison with the case where the inner binary is not being perturbed by the third compact body. Fig. 4.9(b) shows the components of the waveform for h_+ polarisation. In both cases the plot shows in grey the mass quadrupole.⁸ The mass octupole plus the current quadrupole $MO + CQ$ are the red line (for the triple system) and the blue one (for the binary). Notice that in the triple system the $MO + CQ$ is modulated by the period of the third body (one cycle of modulation is half orbit of the third body). The perturbation affects also the merger time, the triple system take less time before the inner binary merge. However, for other initial configuration we observe the opposite behaviour, i.e., the single binary can merge before than the perturbed one. For each case, a combination of parameters like initial eccentricities, mass ratio or semi-major ratio can modify the merger time.

⁸The waveform looks like a shadow region because for the whole timescale of the evolution a single cycle looks like a very high frequency wave.

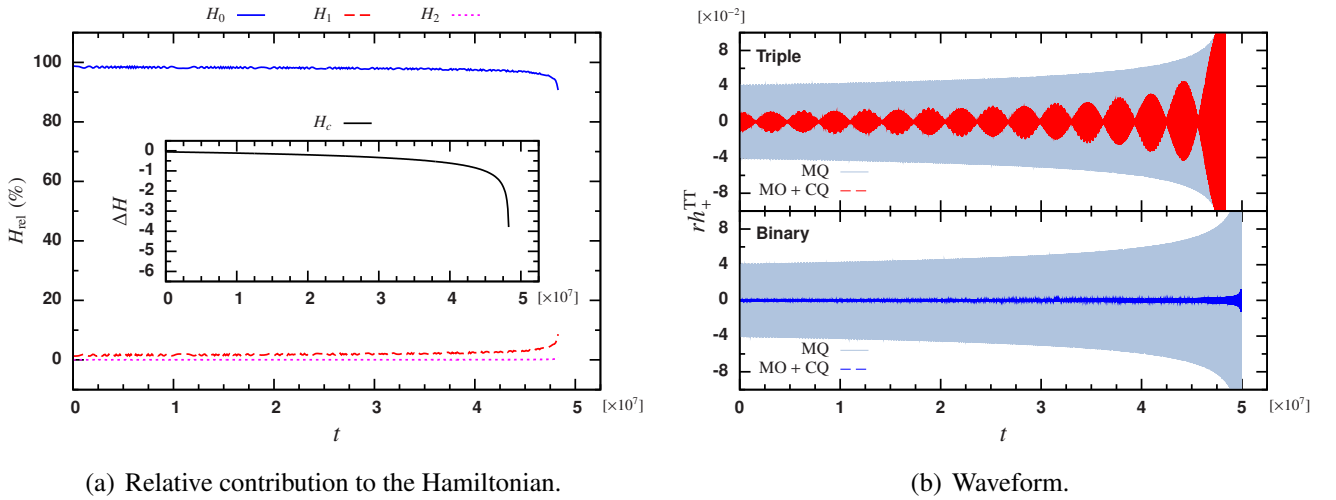


Figure 4.9: Planar hierarchical system. (a) Relative contribution to the Hamiltonian defined by (4.38). The inset shows the variation of $H_c = H_0 + H_1 + H_2$. Notice that when the system approaches to the merger phase, the Hamiltonian decreases fast. (b) Comparison between the perturbed binary and the unperturbed one. The grey region is the mass quadrupole **MQ** contribution to the waveform rh_+ , the region inside the grey one is the mass octupole plus the current quadrupole **MO + CQ** contribution to the waveform rh_+ (in red for the triple system and blue for the binary).

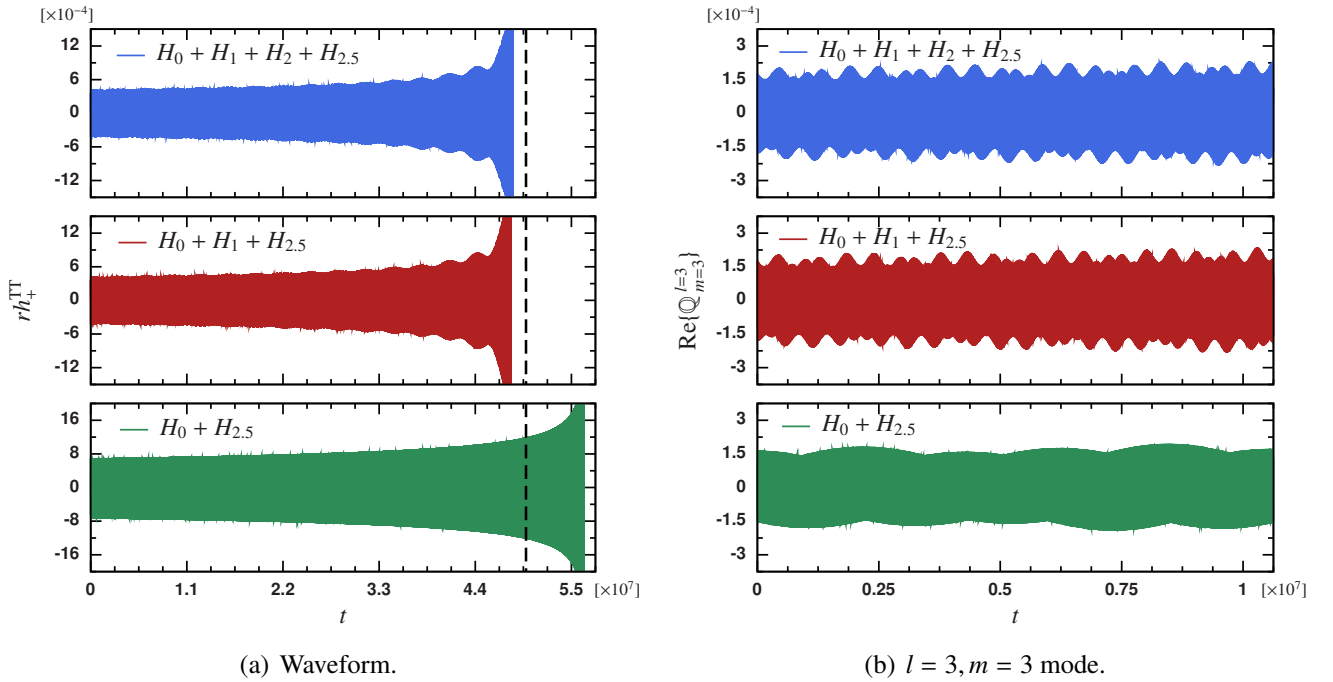


Figure 4.10: Successive change in the waveform due to post-Newtonian corrections. (a) Waveform of a radiative Newtonian system (bottom), radiative 1 PN system (middle), and full 2.5 PN system (top). The waveform includes the current and mass quadrupole and the mass octupole contributions. The vertical dash line at $t = 4.98 \times 10^7$ mark the time when the non-perturbed binary system start the merger phase (see Fig. 4.9(b)). (b). Mode $\text{Re}\{Q_{m=3}^{l=3}\}$ for the three cases referred in (a) for early time in the evolution $t < 10^7$.

Additionally to the comparison to the non-perturbed binary system, we use the planar configuration to explore the influence of the conservative post-Newtonian corrections. As in the previous case (which we will denote as *full 2.5 PN* case), we solve the system for equations of motion where we remove the 2 PN part of the Hamiltonian (*radiative 1 PN*) and where we remove both 1 and 2 PN corrections (*radiative Newtonian*). The full 2.5 PN case does not show a big difference respect to the radiative 1 PN case. The merger phase time changes from $t = 4.8325 \times 10^7$ in the first case to $t = 4.8075 \times 10^7$ in the second one. The waveform does not suffer a noticeable change (see Fig. 4.10). On the other hand, in the radiative Newtonian case the result changes dramatically. The merger phase time start later than in previous cases (around $t = 5.6352 \times 10^7$) and also later than the non-perturbed case (see Fig. 4.10(a)). The resulted waveform is also different. In the radiative Newtonian case each part of the waveform (mass and current quadrupole and the mass octupole) produces a relative constructive interference. The resulted waveform is bigger in amplitude than in the other cases (see the scales in Fig. 4.10(a)). The individual components of the waveform and the modes are of the same amplitude. Nevertheless, the additional precession and change on the dynamics of the full 2.5 PN case and the radiative 1 PN case produces different wave components (see Fig. 4.10(b)). The radiative Newtonian case produces a smoother waveform than the one produces with the inclusion of 1 and 2 PN corrections.

The modulation of the $l = 3$ modes of the waveform are related to the period of the third body. On the other hand, the amplitude of the $l = 3$ spherical components of the waveform encode information about the inclination angle i . We run simulations with the same initial configuration for $i \in \{0, \pi/8, \pi/4, 3\pi/8, \pi/2\}$. Fig 4.11(a) shows the variation on the amplitude for the real part of the modes $\mathbb{Q}_{m=2}^{l=3}$ and $\mathbb{Q}_{m=3}^{l=3}$ as function of i .⁹ The real part of $\mathbb{Q}_{m=2}^{l=3}$ is zero for planar motion $i = 0$. However, the contribution of this mode increases with i . On the other hand, the contribution of $\text{Re}\{\mathbb{Q}_{m=3}^{l=3}\}$ is maximum in the planar case and decreases when i increase. This behaviour is symmetric respect to $i = \pi/2$ and periodic of period π . We estimate the contribution of each mode calculating the *area* which is cover by the real part of the mode

$$\mathcal{A}_m^l(\tau) := - \int_{\tau_f}^{\tau} |\text{Re}\{\mathbb{Q}_m^l\}| d\tau, \quad (4.44)$$

⁹The real and the imaginary part of the modes show the same behaviour. For simplicity we present only the analysis of the real part.

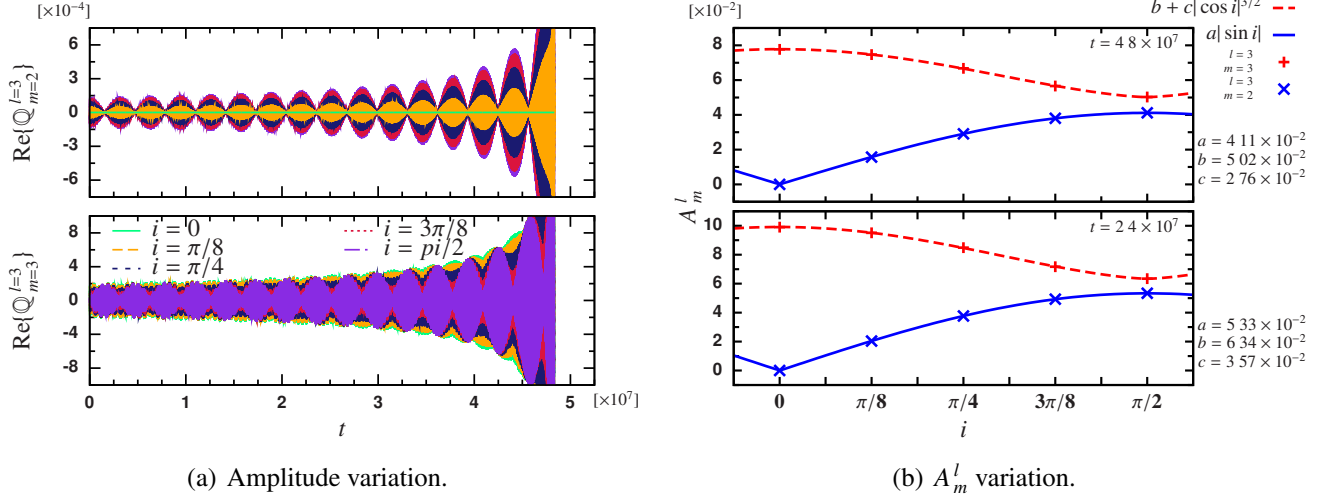


Figure 4.11: Variation on the amplitude of $l = 3$, $m = 2, 3$, modes as function of the inclination angle i . (a). Superposition of $\text{Re}\{Q_{m=2}^{l=3}\}$ and $\text{Re}\{Q_{m=3}^{l=3}\}$ as function of i . (b) Variation of A_m^l as function of i for $t = t_f$ (upper panel) and $t = t_f/2$ (lower panel).

where $\tau_f = 4.8325 \times 10^7$ is the final time of the evolution.¹⁰ We compute $\mathcal{A}_m^l(t)$ for 6 equal spaced times in the interval of simulation. We normalise the results using the maximum value $\mathcal{A}_{\max} = \mathcal{A}_{m=2}^{l=2}$. We denote the normalise area by A_m^l . As an example we show the results for $\tau = 0$ in Table 4.1 where we present the relevant modes. In total we compute 6 tables similar to the previous one, however for brevity we don't present them here. Notice that the contribution of $l = 2$ modes is almost constant respect to the variation of the inclination angle i . In Fig. 4.11(b) we show the variation of $A_{m=2}^{l=3}$ and $A_{m=3}^{l=3}$ for two integration times ($\tau = 0$ and $\tau = \tau_f/2$).

We found that the variation of $A_{m=2}^{l=3}$ is well represented by

$$A_{m=2}^{l=3}(t, i) = a(\tau) |\sin i|. \quad (4.45)$$

On the other hand, $A_{m=3}^{l=3}$ is well modelled by

$$A_{m=3}^{l=3}(t, i) = b(\tau) + c(\tau) |\cos i|^{3/2}, \quad (4.46)$$

where the fitting coefficients a, b and c depend on the integration interval. Table 4.2 shows the

¹⁰We integrate backward on time, then we define the beginning of the merger phase t_f as the origin.

Table 4.1: Variation of A_m^l as function of the inclination angle i .

$\tau = 0$		$i = 0$	$i = \pi/8$	$i = \pi/4$	$i = 2\pi/8$	$i = \pi/2$
l	m	A_m^l				
2	0	0.0147	0.0147	0.0147	0.0147	0.0147
2	2	1.0000	1.0000	1.0000	1.0000	1.0000
3	0	0.0000	0.0005	0.0009	0.0012	0.0013
3	1	0.0199	0.0192	0.0171	0.0144	0.0127
3	2	0.0000	0.0157	0.0291	0.0380	0.0412
3	3	0.0777	0.0747	0.0668	0.0566	0.0503

variation of the fitting coefficients as function of the time integration τ . From this data it is possible to fit a function to establish the functional behaviour of the coefficients respect to the integration time (Fig 4.12 shows the result). The coefficients a , b and c are well represented by

$$a(\tau) = \alpha_1 + \alpha_2/\tau^{1/2}, \quad (4.47)$$

$$b(\tau) = \beta_1 + \beta_2/\tau^{1/5}, \quad (4.48)$$

$$c(\tau) = \gamma_1 + \gamma_2/\tau^{1/2}, \quad (4.49)$$

where

$$\alpha_1 = (1.48 \pm 0.053) \times 10^{-2}, \quad (4.50)$$

$$\alpha_2 = (5.88 \pm 0.075) \times 10^{-2}, \quad (4.51)$$

$$\beta_1 = (-4.4 \pm 0.13) \times 10^{-2}, \quad (4.52)$$

$$\beta_2 = (12.9 \pm 0.16) \times 10^{-2}, \quad (4.53)$$

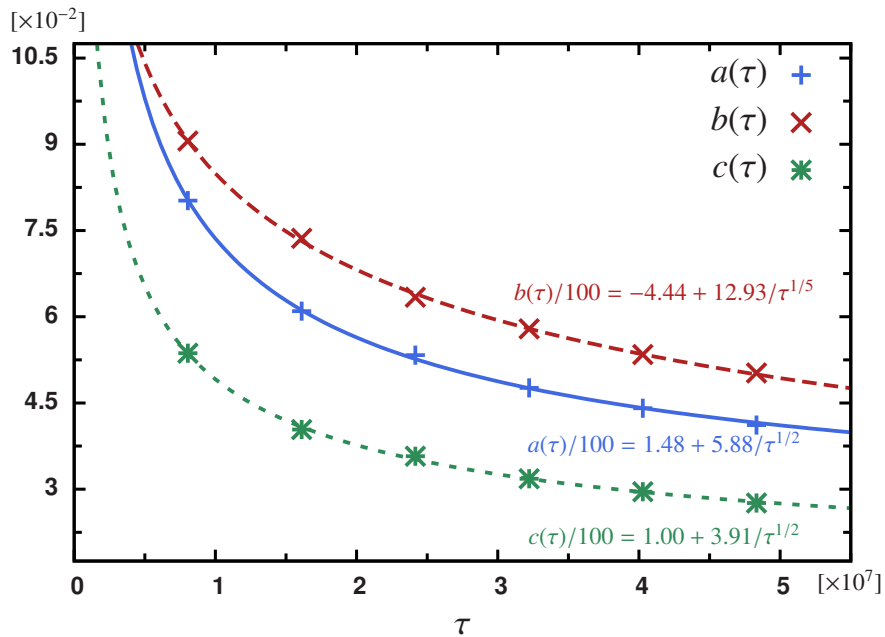
$$\gamma_1 = (1.00 \pm 0.049) \times 10^{-2}, \quad (4.54)$$

$$\gamma_2 = (3.91 \pm 0.069) \times 10^{-2}. \quad (4.55)$$

More general statements about the information related to the three compact object dynamics studying the high modes of the waveform require an extensive parameter study. The previous example shows the characterisation that we can do with this techniques.

Table 4.2: Fitting coefficients of Eqns. (4.45) and (4.46). For the 6 time intervals we compute the fitting coefficients a, b and c . We include the error of each coefficient.

τ [$\times 10^7$]	$a(\tau)$ [$\times 10^{-2}$]		$b(\tau)$ [$\times 10^{-2}$]		$c(\tau)$ [$\times 10^{-2}$]	
0.8054	8.020	± 0.0044	9.058	± 0.0115	5.37	± 0.017
1.6108	6.097	± 0.0025	7.363	± 0.0089	4.04	± 0.013
2.4163	5.332	± 0.0018	6.340	± 0.0087	3.57	± 0.013
3.2217	4.763	± 0.0014	5.789	± 0.0080	3.18	± 0.012
4.0271	4.408	± 0.0012	5.342	± 0.0078	2.95	± 0.011
4.8325	4.116	± 0.0010	5.023	± 0.0075	2.76	± 0.011

**Figure 4.12:** Functional behaviour of the fitting coefficients. The coefficients are well described by an inverse power function in τ .

Chapter 5

Conclusions

We have presented a numerical elliptic solver, `OLLIPTIC`. As a first application, we solve the Hamiltonian constraint to obtain numerical initial data for multiple black hole evolutions. `OLLIPTIC` implements a high-order multigrid method, which is parallelized and uses a box-based mesh refinement. The tests and first applications of the code showed that the new code seems to be sufficiently accurate for our purposes. However, we found that close to the puncture the convergence rate is less than that desired, which is expected for puncture data (see Appendix C). The drop in the convergence close to the punctures is not reflected in the convergence of the evolution.

We have shown evolutions of three black holes which use as initial data solutions to the Hamiltonian constraint generated with the new elliptic solver. We compared with results for a certain analytic approximation for the initial data. In the case of three black holes, the dynamics resulting from approximate data is different from the dynamics produced by evolutions which satisfy the Hamiltonian constraint numerically. As anticipated, the puncture tracks are sensitive to small changes in the initial data. Especially for three and more black holes changing the initial data, e.g. by solving the constraints rather than using an analytical approximation, can lead to qualitatively and quantitatively very different merger sequences. In any case, we confirmed the result of [42, 94] that, as expected, the puncture method lends itself naturally to the simulation of multiple black holes.

Simulations of three, four, or even more black holes lead to the following question about more general merger situations: How can we determine the number of black holes involved in a merger from the observation of gravitational waves? A first analysis of this topic was given previously using a Newtonian approach [9, 127]. Using post-Newtonian techniques and full numerical relativistic simulations, we started exploring a simple case where we give evidence which support the initial conjecture of [127] which we reformulate: *In order to characterise a system of N compact objects, it is necessary to perform an analysis of the waveform which includes at least the $l \leq N$ modes.*¹ In the highly relativistic case, we explore a symmetric triple equal-mass black hole configuration which merge in a spiral way similar to the merger of an equal-mass binary system in an quasi-circular merger. We found that in the case of the triple merger the mode $l = m = 3$ is of the same order or bigger than the $l = m = 2$ mode. For the binary system we find the opposite, namely the $l = m = 3$ mode is almost zero. Using post-Newtonian simulations for a particularly hierarchical configuration, we analysed the waveforms. We found that, looking at the mass octupole and current quadrupole part of the waveform, it is possible to distinguish between a Jacobian system and a binary system. Additionally, in this case we found a relation between the modulation of the modes $l = 3$ and the period of the third compact object. We established a link between the amplitude of the $l = 3, m = 2$ and $l = 3, m = 3$ modes and the angle of the osculating orbital planes.

In the future, we plan to extend our research of the three-compact-body problem presented in this thesis. Using numerical relativity methods, we plan to explore the characterisation of a triple merger from the analysis of the high modes of the waveform. We plan to study the influence of the spin in the ejection or merger of the three bodies. Using the post-Newtonian techniques we plan to do a systematic study of other hierarchical systems, as well as, slow encounters. We plan to improve the calculation of the waveforms (perhaps including post-Newtonian corrections) and the multipole decomposition as well. The study of three compact spinning bodies in the post-Newtonian formalism is a problem which is in our scope. An interesting problem is the study of chaos in the three compact body problem from the post-Newtonian point of view and particularly with the inclusion of gravitational radiation.

¹The original statement in [127] reads: *...Classification of N (or fewer) particles producing (nearly) the same wave forms requires inclusion of the l th multiple part with $l \leq N$.*

Bibliography

- [1] <http://www.tpi.uni-jena.de/gravity/Showcase/>.
- [2] Sverre J. Aarseth. *Gravitational N-Body Simulations*. Cambridge Monographs on Mathematical Physics. Cambridge University Press, 2003.
- [3] T. A. Agekyan and J. P. Anosova. A study of the dynamics of triple systems by means of statistical sampling. *Astronomicheskii Zhurnal*, 44:1261, 1967. (Soviet Astronomy 11, 1006).
- [4] George Biddell Airy. *Gravitation; an elementary explanation of the principal perturbations in the solar system*. Macmillan, 1884.
- [5] Miguel Alcubierre. *Introduction to 3+1 Numerical Relativity*. International Series of Monographs on Physics. Oxford University Press, USA, June 2008.
- [6] Miguel Alcubierre and Bernd Brügmann. Simple excision of a black hole in 3+1 numerical relativity. *Phys. Rev. D*, 63:104006, 2001.
- [7] Miguel Alcubierre, Bernd Brügmann, Peter Diener, Michael Koppitz, Denis Pollney, Edward Seidel, and Ryoji Takahashi. Gauge conditions for long-term numerical black hole evolutions without excision. *Phys. Rev. D*, 67:084023, 2003.
- [8] Marcus Ansorg, Bernd Brügmann, and Wolfgang Tichy. A single-domain spectral method for black hole puncture data. *Phys. Rev. D*, 70:064011, 2004.
- [9] Hideki Asada. Gravitational wave forms for a three-body system in lagrange’s orbit: Parameter determinations and a binary source test. *Phys. Rev. D*, 80(6):064021, Sep 2009.
- [10] O. Axelsson and B. Polman. *AMLI’96: Proceedings of the Conference on Algebraic Multilevel Iteration Methods with Applications*. University of Nijmegen, Nijmegen, The Netherlands, 1996.
- [11] D. Bai and A. Brandt. Local mesh refinement multilevel techniques. *SIAM J. Sci. Stat. Comput.*, 8(2):109–134, 1987.
- [12] John Baker, Bernd Brügmann, Manuela Campanelli, Carlos O. Lousto, and Ryoji Takahashi. Plunge waveforms from inspiralling binary black holes. *Phys. Rev. Lett.*, 87:121103, 2001.
- [13] John G. Baker, Joan Centrella, Dae-II Choi, Michael Koppitz, and James van Meter. Gravitational wave extraction from an inspiraling configuration of merging black holes. *Phys. Rev. Lett.*, 96:111102, 2006.
- [14] J. D. Barrow and J. Levin. A Test of a Test for Chaos. *arXiv:nlin/0303070*, March 2003.
- [15] June Barrow-Green. *Poincare and the Three Body Problem*. American Mathematical Society, 1996.

- [16] Thomas W. Baumgarte and Stuart L. Shapiro. On the numerical integration of Einstein's field equations. *Phys. Rev. D*, 59:024007, 1998.
- [17] R. Beig and N. O'Murchadha. Trapped surfaces in vacuum spacetimes. *Class. Quantum Grav.*, 11:419, 1994.
- [18] R. Beig and N. O'Murchadha. Vacuum spacetimes with future trapped surfaces. *Class. Quantum Grav.*, 13:739–751, 1996.
- [19] Argelia Bernal and F. Siddhartha Guzm'an. Scalar field dark matter: Head-on interaction between two structures. *Phys.Rev. D*, 74:103002, 2006.
- [20] Argelia Bernal and F. Siddhartha Guzm'an. Scalar field dark matter: Nonspherical collapse and late-time behavior. *Phys.Rev. D*, 74:063504, 2006.
- [21] L. Blanchet. Gravitational Radiation from Post-Newtonian Sources and Inspiralling Compact Binaries. *Living Rev. Relativity*, 2006-4, 2006. [Article in Online Journal] cited on 2 Jun 2006, <http://www.livingreviews.org/Articles/lrr-2006-4/download/index.html>.
- [22] Luc Blanchet. Gravitational radiation from post-Newtonian sources and inspiralling compact binaries. *Living Rev. Relativity*, 5:3, 2002.
- [23] J. M. Bowen and J. W. York, Jr. Time-asymmetric initial data for black holes and black-hole collisions. *Phys. Rev. D*, 21:2047–2056, 1980.
- [24] John P. Boyd. *Chebyshev and Fourier Spectral Methods (Second Edition, Revised)*. Dover Publications, New York, 2001.
- [25] A. Brandt and Boris Diskin. *Multigrid Solvers on Decomposed Domains*. Americal Mathematical Society, Providence, Rhode Island, 1994.
- [26] A Brandt and A Lanza. Multigrid in general relativity. i. schwarzschild spacetime. *Class. Quantum Grav.*, 5(5):713–732, 1988.
- [27] Achi Brandt. Multi-level adaptive solutions to boundary-value problems. *Math. Comp.*, 31:333–390, 1977.
- [28] S. Brandt and B. Brüggmann. A simple construction of initial data for multiple black holes. *Phys. Rev. Lett.*, 78(19):3606–3609, 1997.
- [29] William L. Briggs, Van Emden Henson, and Steve F. McCormick. *A Multigrid Tutorial*. SIAM Press, Philadelphia, 2nd edition, 2000.
- [30] D. R. Brill and R. W. Lindquist. Interaction energy in geometrostatics. *Phys. Rev.*, 131:471–476, 1963.
- [31] R. C. Brower, K. Moriarty, E. Myers, and C. Rebbi. The multigrid method for fermion calculations in quantum chromodynamics. In S. F. McCormick, editor, *Multigrid Methods: Theory, Applications, and Supercomputing*, volume 110 of *Lecture Notes in Pure and Applied Mathematics*, pages 85–100. Marcel Dekker, New York, 1988.
- [32] J. David Brown and Lisa L. Lowe. Multigrid elliptic equation solver with adaptive mesh refinement. *J. Comput. Phys.*, 209:582–598, 2005.
- [33] J. David Brown and Lisa L. Lowe. Multigrid elliptic equation solver with adaptive mesh refinement. *Journal of Computational Physics*, 209(2):582–598, 2005.
- [34] B. Brüggmann. Adaptive mesh and geodesically sliced Schwarzschild spacetime in 3+1 dimensions. *Phys. Rev. D*, 54(12):7361–7372, 1996.

- [35] B. Brügmann. Evolution of 30 black holes spelling AEI, 1997. Talk for Fachbeirat, Albert Einstein Institute. Unpublished.
- [36] B. Brügmann. Binary black hole mergers in 3d numerical relativity. *Int. J. Mod. Phys.*, 8:85–100, 1999.
- [37] Bernd Brügmann, José A. González, Mark Hannam, Sascha Husa, Ulrich Sperhake, and Wolfgang Tichy. Calibration of Moving Puncture Simulations. *Phys. Rev.*, D77:024027, 2008.
- [38] Bernd Brügmann, Wolfgang Tichy, and Nina Jansen. Numerical simulation of orbiting black holes. *Phys. Rev. Lett.*, 92:211101, 2004.
- [39] C. A. Burdet. Regularization of the two body problem. *Zeitschrift Angewandte Mathematik und Physik*, 18:434–438, May 1967.
- [40] Cactus Computational Toolkit. <http://www.cactuscode.org>.
- [41] Manuela Campanelli, Carlos O. Lousto, Pedro Marronetti, and Yosef Zlochower. Accurate evolutions of orbiting black-hole binaries without excision. *Phys. Rev. Lett.*, 96:111101, 2006.
- [42] Manuela Campanelli, Carlos O. Lousto, and Yosef Zlochower. Close encounters of three black holes. *Phys. Rev.*, D77:101501(R), 2008.
- [43] Zhoujian Cao, Hwei-Jang Yo, and Jui-Ping Yu. Reinvestigation of moving punctured black holes with a new code. *Phys. Rev. D*, 78(12):124011, Dec 2008.
- [44] T. Chiba, T. Imai, and H. Asada. Can n-body systems generate periodic gravitational waves? *Mon. Not. R. Astron. Soc.*, 377(1):269–272, 2007.
- [45] Matthew W. Choptuik. Numerical analysis for numerical relativists. Course given at VII Mexican School on Gravitation and Mathematical Physics, November 26 2006, 2006.
- [46] Matthew W. Choptuik and William G. Unruh. An introduction to the multi-grid method for numerical relativists. *Gen. Rel. Grav.*, 18(8):813–843, August 1986.
- [47] Yi-Zen Chu. -body problem in general relativity up to the second post-newtonian order from perturbative field theory. *Phys. Rev. D*, 79(4):044031, Feb 2009.
- [48] Gregory B. Cook. Initial data for numerical relativity. *Living Rev. Relativity*, 3:5, 2000.
- [49] N. J. Cornish and J. Levin. Chaos and damping in the post-Newtonian description of spinning compact binaries. *Phys. Rev. D*, 68(2):024004+, July 2003.
- [50] Thibault Damour and Gerhard Schäfer. Lagrangians for n point masses at the second post-newtonian approximation of general relativity. *Gen. Rel. Grav.*, 17(9):879–905, 1985.
- [51] Kenneth A. Dennison, Thomas W. Baumgarte, and Harald P. Pfeiffer. Approximate initial data for binary black holes. *Phys. Rev.*, D74:064016, 2006.
- [52] P. Diener. A new general purpose event horizon finder for 3D numerical spacetimes. *Class. Quantum Grav.*, 20(22):4901–4917, 2003.
- [53] Eanna E. Flanagan and Scott A. Hughes. The basics of gravitational wave theory. *New J. Phys.*, 7:204, 2005.
- [54] Bengt Fornberg. Classroom note: calculation of weights in finite difference formulas. *SIAM Review*, 40(3):685–691, 1998.

- [55] Pablo Galaviz. Codigo computacional para resolver ecuaciones elipticas en relatividad numerica. Master's thesis, Universidad Nacional Autonoma de Mexico, 2007. <http://www.archive.org/details/PabloGalavizMasterThesis>.
- [56] Pablo Galaviz, Bernd Brügmann, and Zhoujian Cao. Numerical evolution of multiple black holes with accurate initial data. *Phys. Rev. D*, 82(2):024005, Jul 2010.
- [57] Pablo Galaviz, Bernd Brügmann, and Zhoujian Cao. Numerical evolution of multiple black holes with accurate initial data. 2010.
- [58] Reinaldo J. Gleiser, Gaurav Khanna, and Jorge Pullin. Evolving the Bowen-York initial data for boosted black holes. *Phys. Rev. D*, 66:024035, 2002.
- [59] Reinaldo J. Gleiser, Carlos O. Nicasio, Richard H. Price, and Jorge Pullin. Evolving the Bowen-York initial data for spinning black holes. *Phys. Rev. D*, 57:3401–3407, 1998.
- [60] Herbert Goldstein, Charles P. Poole, and John Safko. *Classical Mechanics*. Addison Wesley, 2001.
- [61] A. Gopakumar and C. Königsdörffer. Deterministic nature of conservative post-Newtonian accurate dynamics of compact binaries with leading order spin-orbit interaction. *Phys. Rev. D*, 72(12):121501–+, December 2005.
- [62] Ericourgoulhon. Construction of initial data for 3+1 numerical relativity. *Journal of Physics: Conference Series*, 91(1):012001, 2007.
- [63] A. Gualandris, S. Portegies Zwart, and M. S. Sipior. Three-body encounters in the Galactic Centre: the origin of the hypervelocity star SDSS J090745.0+024507. *Mon. Not. R. Astron. Soc.*, 363:223–228, October 2005.
- [64] Kayhan Gültekin, M. Coleman Miller, and Douglas P. Hamilton. Three-body encounters of black holes in globular clusters. volume 686, pages 135–140. AIP, 2003.
- [65] Kayhan Gultekin, M. Coleman Miller, and Douglas P. Hamilton. Growth of intermediate-mass black holes in globular clusters. *ApJ*, 616(1):221–230, 2004.
- [66] Kayhan Gultekin, M. Coleman Miller, and Douglas P. Hamilton. Three-Body Dynamics with Gravitational Wave Emission. *ApJ*, 640:156–166, 2006.
- [67] Karl E. Gustafson. *Introduction to Partial Differential Equations and Hilbert Space Methods*. Dover, 1999.
- [68] F. Siddhartha Guzm'an and L. Arturo Ureña-López. Evolution of the Schrödinger-Newton system for a self-gravitating scalar field. *Phys. Rev. D*, 69(124033), 2004.
- [69] F. Siddhartha Guzm'an and L. Arturo Ureña-L'opez. Gravitational Cooling of Self-gravitating Bose Condensates. *The Astrophysical Journal*, 645(2):814–819, 2006.
- [70] Susan G. Hahn and Richard W. Lindquist. The two body problem in geometrodynamics. *Ann. Phys.*, 29:304–331, 1964.
- [71] W. Han. Chaos and dynamics of spinning particles in Kerr spacetime. *Gen. Rel. Grav.*, 40:1831–1847, September 2008.
- [72] Scott H. Hawley and Richard A. Matzner. Tips for implementing multigrid methods on domains containing holes. *Class. Quantum Grav.*, 21:805–821, 2004.
- [73] D. C. Heggie. A global regularisation of the gravitational N-body problem. *Celestial Mechanics*, 10:217–241, October 1974.

- [74] P. Heinämäki. Symmetry of black hole ejections in mergers of galaxies. *Astron. Astrophys.*, 371:795–805, June 2001.
- [75] M. Hénon. A family of periodic solutions of the planar three-body problem, and their stability. *Celestial Mechanics and Dynamical Astronomy*, 13:267–285, 1976.
- [76] G. T. Herman. *Image Reconstruction From Projections, The Fundamentals of Computerized Tomography*. Academic Press, New York, 1980.
- [77] Loren Hoffman and Abraham Loeb. Three-Body Kick to a Bright Quasar out of Its Galaxy During a Merger. *Astrophys. J.*, 638:L75–L78, 2006.
- [78] Loren Hoffman and Abraham Loeb. Dynamics of triple black hole systems in hierarchically merging massive galaxies. *Mon. Not. Roy. Astron. Soc.*, 377:957–976, 2007.
- [79] Sascha Husa, José A. González, Mark Hannam, Bernd Brügmann, and Ulrich Sperhake. Reducing phase error in long numerical binary black hole evolutions with sixth order finite differencing. *Class. Quantum Grav.*, 25:105006, 2008.
- [80] Tatsunori Imai, Takamasa Chiba, and Hideki Asada. Choreographic solution to the general-relativistic three-body problem. *Phys. Rev. Lett.*, 98(20):201102, May 2007.
- [81] Masaki Iwasawa, Yoko Funato, and Junichiro Makino. Evolution of massive black hole triples. i. equal-mass binary-single systems. *The Astrophysical Journal*, 651(2):1059, 2006.
- [82] P. Jaranowski and G. Schäfer. Radiative 3.5 post-Newtonian ADM Hamiltonian for many body point-mass systems. *Phys. Rev. D*, 55:4712–4722, 1997.
- [83] George Em Karniadakis and Roberet M. Kirby. *Parallel Scientific Computing in C++ and MPI*. Cambridge University Press, 2003.
- [84] Peter Knabner and Lutz Angermann. *Numerical Methods for Elliptic and Parabolic Partial Differential Equations*. Springer, 2003.
- [85] C. Königsdörffer, G. Faye, and G. Schäfer. Binary black-hole dynamics at the third-and-a-half post-newtonian order in the adm formalism. *Phys. Rev. D*, 68:044004, 2003.
- [86] Pablo Laguna. Conformal-thin-sandwich initial data for a single boosted or spinning black hole puncture. *Phys. Rev. D*, 69:104020, 2004.
- [87] A Lanza. Multigrid in general relativity. ii. kerr spacetime. *Class. Quantum Grav*, 9(3):677, 1992.
- [88] H. J. Lehto, S. Kotiranta, M. J. Valtonen, P. Heinämäki, S. Mikkola, and A. D. Chernin. Mapping the three-body system - decay time and reversibility. *Mon. Not. R. Astron. Soc.*, 388:965–970, August 2008.
- [89] Randall J. LeVeque. *Finite Difference Methods for Ordinary and Partial Differential Equations*. SIAM Press, 2007.
- [90] J. Levin. Gravity Waves, Chaos, and Spinning Compact Binaries. *Phys. Rev. D*, 84:3515–3518, April 2000.
- [91] J. Levin. Chaos and order in models of black hole pairs. *Phys. Rev. D*, 74(12):124027–+, December 2006.
- [92] Peter Linz. *Theoretical Numerical Analysis*. Dover Publications, 2001.
- [93] Carlos O Lousto and Hiroyuki Nakano. Three-body equations of motion in successive post-newtonian approximations. *Class. Quantum Grav.*, 25(19):195019, 2008.

- [94] Carlos O. Lousto and Yosef Zlochower. Foundations of multiple black hole evolutions. *Phys. Rev.*, D77:024034, 2008.
- [95] Michele Maggiore. *Gravitational Waves*, volume 1. Oxford University Press, USA., 2007.
- [96] Tonatihu Matos and L. Arturo Ureña-López. Further analysis of a cosmological model with quintessence and scalar dark matter. *Phys. Rev. D*, 63(6):063506, Feb 2001.
- [97] Tonatihu Matos and L. Arturo Ureña-López. On the nature of dark matter. *Int. J. Mod. Phys. D*, 13:2287–2291, 2004.
- [98] S. Mikkola. Encounters of binaries. I - Equal energies. *Mon. Not. R. Astron. Soc.*, 203:1107–1121, June 1983.
- [99] S. Mikkola. Encounters of binaries. II - Unequal energies. *Mon. Not. R. Astron. Soc.*, 207:115–126, March 1984.
- [100] S. Mikkola and S. J. Aarseth. A chain regularization method for the few-body problem. *Celestial Mechanics and Dynamical Astronomy*, 47:375–390, December 1989.
- [101] S. Mikkola and S. J. Aarseth. An implementation of N-body chain regularization. *Celestial Mechanics and Dynamical Astronomy*, 57:439–459, November 1993.
- [102] S. Mikkola and S. J. Aarseth. A Slow-down Treatment for Close Binaries. *Celestial Mechanics and Dynamical Astronomy*, 64:197–208, September 1996.
- [103] M. Coleman Miller and Douglas P. Hamilton. Four-body effects in globular cluster black hole coalescence. 2002.
- [104] C. Moore and M. Nauenberg. New Periodic Orbits for the n-Body Problem. *arXiv:math/0511219v2*, October 2008.
- [105] Christopher Moore. Braids in classical dynamics. *Phys. Rev. Lett.*, 70(24):3675–3679, Jun 1993.
- [106] M. Nauenberg. Periodic orbits for three particles with finite angular momentum. *Physics Letters A*, 292:93–99, December 2001.
- [107] D. J. Paddon and H. Holstein. *Multigrid Methods for Integral and Differential Equations*, volume 3 of *The Institute of Mathematics and its Applications Conference Series*. Clarendon Press, Oxford, 1985.
- [108] P. C. Peters. Gravitational radiation and the motion of two point masses. *Phys. Rev.*, 136:B1224–B1232, 1964.
- [109] William H. Press, Saul A. Teukolsky, William T. Vetterling, and Brian P. Flannery. *Numerical Recipes in C++*. Cambridge University Press, 1992.
- [110] Frans Pretorius. Evolution of binary black hole spacetimes. *Phys. Rev. Lett.*, 95:121101, 2005.
- [111] D. Ron. *Development of Fast Numerical Solvers for Problems of Optimization and Statistical Mechanics*. PhD thesis, The Weizmann Institute of Science, Rehovet, Israel, 1989.
- [112] V. Sahni and L. Wang. New cosmological model of quintessence and dark matter. *Phys. Rev. D*, 58:023503, 1998.
- [113] Gerhard Schäfer. Three-body hamiltonian in general relativity. *Physics Letters A*, 123(7):336–339, 1987.
- [114] Mark A. Scheel, Harald P. Pfeiffer, Lee Lindblom, Lawrence E. Kidder, Oliver Rinne, and Saul A. Teukolsky. Solving Einstein’s equations with dual coordinate frames. *Phys. Rev. D*, 74:104006, 2006.

- [115] J. D. Schnittman and F. A. Rasio. Ruling Out Chaos in Compact Binary Systems. *Phys. Rev. Lett.*, 87(12):121101, September 2001.
- [116] Jeremy D. Schnittman. The Lagrange Equilibrium Points L₄ and L₅ in a Black Hole Binary System. *arXiv:1006.0182v1*, 2010.
- [117] Masaru Shibata and Takashi Nakamura. Evolution of three-dimensional gravitational waves: Harmonic slicing case. *Phys. Rev. D*, 52:5428, 1995.
- [118] Barry Smith, Petter Bjorstad, and William Gropp. *Domain Decomposition: Parallel Multilevel Methods for Elliptic Partial Differential Equations*. Cambridge University Press, March 2004.
- [119] KF Sundman. Recherches sur le problème des trois corps. *Acta Soc. Sci. Fennicae*, 1907.
- [120] Thomas Szirtes. *Applied Dimensional Analysis and Modeling*. Butterworth-Heinemann, 2 edition, 2006.
- [121] X.-C. Tai and P. Neittanmäki. A FE-splitting-up method and its application to distributed parameter identification of parabolic type. In *Approximation, Optimisation and Computing. Theory and Applications*, pages 185–188, Amsterdam, 1990. Elsevier.
- [122] Michael E. Taylor. *Partial Differential Equations I*, volume 115 of *Applied Mathematical Science*. Springer, 1996.
- [123] Michael E. Taylor. *Partial Differential Equations II*, volume 116 of *Applied Mathematical Science*. Springer, 1996.
- [124] Michael E. Taylor. *Partial Differential Equations III*, volume 117 of *Applied Mathematical Science*. Springer, 1996.
- [125] Marcus Thierfelder, Bernd Brüggemann, and Pablo Galaviz. Finding event horizons in multiple black hole simulations. 2010.
- [126] K. Thorne. Multipole expansions of gravitational radiation. *Rev. Mod. Phys.*, 52(2):299, 1980.
- [127] Yuji Torigoe, Keisuke Hattori, and Hideki Asada. Gravitational wave forms for two- and three-body gravitating systems. *Phys. Rev. Lett.*, 102(25):251101, Jun 2009.
- [128] Yousuke Itoh Toshifumi Futamase. The post-newtonian approximation for relativistic compact binaries. *Living Reviews in Relativity*, 10(2), 2007.
- [129] Ulrich Trottenberg, Cornelis Oosterlee, and Anton Schüller. *Multigrid*. Academic Press, San Diego, 2001.
- [130] Aslak Tveito and Ragnar Winther. *Introduction to Partial Differential Equations: A Computational Approach*. Texts in Applied Mathematics. Springer, 2004.
- [131] M. Valtonen and S. Mikkola. The few-body problem in astrophysics. *Annu. Rev. Astron. Astrophys.*, 29:9–29, 1991.
- [132] Mauri J. Valtonen and Hannu Karttunen. *The three-body problem*. Cambridge University Press, New York, 2006.
- [133] H. F. Weinberger. *A First Course in Partial Differential Equations: with Complex Variables and Transform Methods*. Dover, 1965.
- [134] Wolfram Research, Inc. *Mathematica*. Wolfram Research, Inc., version 7.0 edition, 2008.
- [135] Tetsuro Yamamoto, Masaru Shibata, and Keisuke Taniguchi. Simulating coalescing compact binaries by a new code (sacra). *Phys. Rev. D*, 78(6):064054, Sep 2008.

- [136] Gerhard Zumbusch. *Parallel Multilevel Methods: Adaptive Mesh Refinement and Loadbalancing*. Teubner, January 2003.

Appendix A

Multigrid methods

Multigrid (MG) methods have a wide range of applications. For example there are MG methods suitable for solving elliptic partial differential equations [129], algebraic problems [10], image reconstruction and tomography [76], optimisation [121], statistical mechanics [111], quantum chromodynamics [31] and integral equations [107] among others. We can consider MG methods part of a more general class of algorithms known as *multilevel methods* [118].

We focus here on the MG method for solving elliptic partial differential equations. However, in every MG method the basic idea is to solve a given problem at some scale, using coarser scales to accelerate the computation. In our case, using a finite difference approach we solve a problem in a domain Ω for some fine grid of length h , using a set of coarse grids $\Omega^{h/2^l}$ for $l \in \{1, \dots, n\}$. We define a set of grids which contains a geometrical structure related to a physical domain Ω . For that reason this kind of MG methods are known as *Geometric Multigrid* GMG. In contrast to geometrical base multigrid, an algorithm which operate directly on linear sparse algebraic equations is known as *Algebraic Multigrid* AMG. Formally AMG and GMG can be describe in the same way (see e.g., [10] for the details).

Here we describe the MG approach for elliptic partial differential equations. For simplicity, we consider equations $\mathcal{L}u = \rho$ in some domain $\Omega \subset \mathbb{R}^2$ where

$$\mathcal{L}u = a_{11}\partial_x^2 u + a_{12}\partial_x\partial_y u + a_{22}\partial_y^2 u + a_1\partial_x u + a_2\partial_y u + a_0 u. \quad (\text{A.1})$$

where the coefficients a_{ij} , a_i and the source ρ are in general functions of x , y , u , $\partial_x u$ and $\partial_y u$. The operator \mathcal{L} is called *hyperbolic* if $4a_{11}a_{22} < a_{12}^2$, *parabolic* if $4a_{11}a_{22} = a_{12}^2$ and *elliptic* if

$4a_{11}a_{22} > a_{12}^2$. Let us focus in the last kind of operators and particularly in the Poisson equation with Dirichlet boundary condition.

$$\partial_x^2 u(x, y) + \partial_y^2 u(x, y) = \rho(x, y) \quad \text{for } (x, y) \in \Omega, \quad (\text{A.2})$$

$$u(x, y) = f(x, y) \quad \text{for } (x, y) \in \partial\Omega, \quad (\text{A.3})$$

where $f : \partial\Omega \rightarrow \mathbb{R}$ is a given smooth function. The finite difference representation of the problem using second order centred stencil in a uniform discretization grid with mesh size h is

$$u_{i,j-1} + u_{i-1,j} - 4u_{i,j} + u_{i+1,j} + u_{i,j+1} = h^2 \rho_{i,j} \quad \text{for } (x_i, y_j) \in \Omega^h, \quad (\text{A.4})$$

$$u_{i,j} = f_{i,j} \quad \text{for } (x_i, y_j) \in \partial\Omega^h, \quad (\text{A.5})$$

where $x_i = x_0 + ih$, $y_j = y_0 + jh$ are the grid coordinates with indexes $i, j \in \{0, \dots, n-1\}$ defined in the mesh $\bar{\Omega} = [x_0, x_{n-1}] \times [y_0, y_{n-1}]$ and, $u_{i,j} := u(x_i, y_j)$, $\rho_{i,j} := \rho(x_i, y_j)$ and $f_{i,j} := f(x_i, y_j)$. We can map the two indices to a single one by $I := i + jn$, then

$$(i, j) \rightarrow I, \quad (\text{A.6})$$

$$(i+1, j) \rightarrow I+1, \quad (\text{A.7})$$

$$(i-1, j) \rightarrow I-1, \quad (\text{A.8})$$

$$(i, j+1) \rightarrow I+n, \quad (\text{A.9})$$

$$(i, j-1) \rightarrow I-n, \quad (\text{A.10})$$

after this (A.4) becomes:

$$u_{I-n} + u_{I-1} - 4u_I + u_{I+1} + u_{I+n} = h^2 \rho_I. \quad (\text{A.11})$$

With the appropriate remapping of the boundary condition (A.5), we can associate to the equation (A.11) an equivalent linear system

$$\mathbf{A}\vec{u} = \vec{\rho}, \quad (\text{A.12})$$

where \mathbf{A} is an $n^2 \times n^2$ sparse, banded matrix, with band-width $2n+1$, \vec{u} and $\vec{\rho}$ are n -component

vectors with entrance u_I and ρ_I respectively. The direct method to solve (A.4)-(A.5) consist on invert numerically (A.12) using for example a Gaussian elimination method. However, the computational cost of invert a linear system of size $N = n^2$ is of order $\mathcal{O}(N^2)$. This is very expensive, especially for three dimensional problems where $N = n^3$ and typical grid size are $n \sim 100$.

A better approach is to use an iterative method. The general idea is to split \mathbf{A} as the sum of two suitable sub-matrices $\mathbf{A} = \mathbf{M} + \mathbf{N}$, then we obtain the solution through the iterative process

$$\mathbf{M}\vec{u}^{k+1} = \vec{\rho} - \mathbf{N}\vec{u}^k. \quad (\text{A.13})$$

We define a global error vector $\vec{\epsilon}^k := \vec{u}^k - \vec{u}^\infty$, where \vec{u}^∞ is the exact solution. Then \vec{u}^∞ is solution of A.12, i.e,

$$(\mathbf{M} + \mathbf{N})\vec{u}^\infty = \vec{\rho}. \quad (\text{A.14})$$

From (A.13), (A.14) and the definition of the global error we obtain:

$$\mathbf{M}\vec{\epsilon}^{k+1} = -\mathbf{N}\vec{\epsilon}^k, \quad (\text{A.15})$$

for a non-singular \mathbf{M}

$$\vec{\epsilon}^{k+1} = -\mathbf{M}^{-1}\mathbf{N}\vec{\epsilon}^k \quad (\text{A.16})$$

$$= (-\mathbf{M}^{-1}\mathbf{N})^{k+1}\vec{\epsilon}^0. \quad (\text{A.17})$$

We define the *amplification matrix* as

$$\mathbf{G} = -\mathbf{M}^{-1}\mathbf{N}, \quad (\text{A.18})$$

where the unfortunate term ‘‘amplification’’ comes from the fact that after $n + 1$ iterations the error can be amplified by the application of the matrix. However, the goal of the method is to reduce the error, then \mathbf{G}^n has to be bounded. A necessary condition for stability of the method is that the *spectral radius*¹ satisfy

$$\rho(\mathbf{G}) < 1. \quad (\text{A.19})$$

¹The spectral radius of a matrix is defined as the maximum magnitude of its eigenvalues.

Defining the matrix \mathbf{U} , \mathbf{D} and \mathbf{L} as the strictly upper, diagonal and strictly lower part of the matrix \mathbf{A} respectively, we can specify some common iterative methods, particularly relaxation methods:

- Jacobi - Computational cost $O(N^2)$

$$\mathbf{M} = \mathbf{D}, \quad (\text{A.20})$$

$$\mathbf{N} = \mathbf{L} + \mathbf{U}. \quad (\text{A.21})$$

- Gauss-Seidel - Computational cost $O(N^2)$

$$\mathbf{M} = \mathbf{D} + \mathbf{L}, \quad (\text{A.22})$$

$$\mathbf{N} = \mathbf{U}. \quad (\text{A.23})$$

- Successive over-relaxation (SOR) - Computational cost $O(N^{3/2})$

$$\mathbf{M} = \omega^{-1}\mathbf{D} + \mathbf{L}, \quad (\text{A.24})$$

$$\mathbf{N} = (1 - \omega)\mathbf{D} + \mathbf{U}, \quad (\text{A.25})$$

where $1 < \omega < 2$.

- Symmetric successive over-relaxation (SSOR) - Computational cost $O(N^{5/4})$

$$\mathbf{M} = \frac{(\mathbf{D} + \omega\mathbf{U})\mathbf{D}^{-1}(\mathbf{D} + \omega\mathbf{L})}{\omega(2 - \omega)}, \quad (\text{A.26})$$

$$\mathbf{N} = -\frac{[(1 - \omega)\mathbf{D} - \omega\mathbf{L}]\mathbf{D}^{-1}[(1 - \omega)\mathbf{D} - \omega\mathbf{U}]}{\omega(2 - \omega)}, \quad (\text{A.27})$$

where $1 < \omega < 2$.

For SOR and SSOR, the optimal value of the parameter ω depends on the problem to solve. Relaxation methods are characterised by a slow convergence. In practise they are useful only for one dimensional problems or for relatively small meshes. However, relaxation methods are good at reducing the error at some scales (relative to the mesh resolution). To see this we expand

the initial global error into eigen-components

$$\vec{\epsilon}^0 = \sum_{i=0}^{n-1} c_i \vec{e}_i, \quad (\text{A.28})$$

then using (A.17)

$$\vec{\epsilon}^k = \sum_{i=0}^{n-1} \lambda_i^k c_i \vec{e}_i, \quad (\text{A.29})$$

where λ_i are the eigenvalues of \mathbf{G}^k . For a large number of iterations k , the error is dominated by the components $\lambda_i^k c_i \vec{e}_i$ with $\lambda_i \lesssim 1$, typically that is the case for $i \simeq 0$ and $i \simeq n - 1$. This determines the overall convergence rate. Nevertheless, other components of the error decay much more rapidly like the middle range components, those nearest $i \simeq n/2$ with $\lambda_i \sim 1/2$. Usually just with a few iterations it is possible to reduce middle range frequencies of the error to a desired tolerance. In contrast, other frequencies may required thousand of iterations.

The key idea of the MG methods is that middle range frequencies of the errors in a coarse grid represent low frequency in a finer one. Then, if we transfer the solution between coarse grids and finer grids we can reduce the error in an efficient way. In practise, instead of transferring the solution between grids, we solve an equation for the error. After taking ν iterations on a fine grid we obtain an error

$$\vec{\epsilon}^\nu = \vec{u}^\nu - \vec{u}^\infty. \quad (\text{A.30})$$

This is related to the residual vector

$$\vec{r}^\nu = \vec{\rho} - \mathbf{A} \vec{u}^\nu, \quad (\text{A.31})$$

by the linear system

$$\mathbf{A} \vec{\epsilon}^\nu = -\vec{r}^\nu. \quad (\text{A.32})$$

If we approximate this system in a coarse grid, we can subtract $\vec{\epsilon}^\nu$ from \vec{u}^ν to obtain a better approximation to \vec{u}^∞ .

To summarise and using a differential operator form instead of the matrix one. We consider that the exact solution u^h is given by the sum of the current numerical approximation U^h plus

an exact² correction v^h

$$u^h = U^h + v^h, \quad (\text{A.33})$$

then for a discrete elliptic operator \mathcal{L}^h

$$\mathcal{L}^h(U^h + v^h) = \rho^h. \quad (\text{A.34})$$

If \mathcal{L}^h is linear

$$\mathcal{L}^h v^h = \rho^h - \mathcal{L}^h U^h := -R^h. \quad (\text{A.35})$$

At this point we can solve (A.35) on a coarser grid

$$\mathcal{L}^{2h} v^{2h} = -r^{2h}. \quad (\text{A.36})$$

However, we have to provide the right hand side of (A.36). To do that we use a *restricted* version of the right hand side of (A.35) via a *restriction* operator³ I_h^{2h} . Then we solve for

$$\mathcal{L}^{2h} V^{2h} = -I_h^{2h} R^h. \quad (\text{A.37})$$

If $2h$ is sufficiently coarse then we can solve this equation to machine accuracy in an inexpensive way, otherwise we can transfer the problem to an even coarser grid. In any case we end with a solution V^{2h} that we can use to correct the solution in the next finer level

$$U_{\text{new}}^h = U_{\text{old}}^h + I_{2h}^h V^{2h}, \quad (\text{A.38})$$

where I_{2h}^h is a *prolongation* operator which maps values from the coarse grid to the finer grid via some interpolation operation. The algorithm described before is known as *Linear Correction Scheme* (LCS). For non-linear operator we have to combine a linearization scheme (see Appendix B) with the *Full Approximation Storage Scheme* (see the algorithms 2.2.1 and 2.2.2).

The two-levels multigrid strategy can be used in several ways, two common are *V-Cycles* and *W-Cycles*. In a V-Cycle we start with an initial guess on the fine grid, at level h_{max} . Then we perform some number of smoothing sweeps p and restrict the problem to a coarser grid. We

²In general we use capital letter for numerical approximations and lowercase for exact functions.

³See the details of the restriction and prolongation operators implementation in Sec. 2.2.1

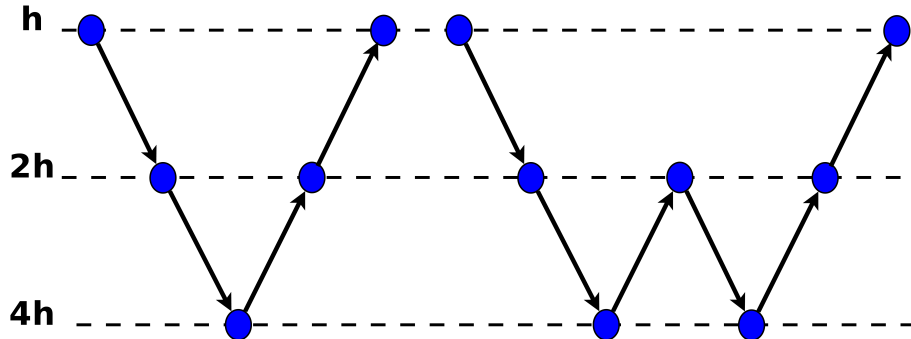


Figure A.1: Sketch of a V-Cycle and W-Cycle with three multigrid levels. In practise it is necessary to perform several V-Cycles before reach the desired accuracy. In some cases a W-Cycle may require several sub-cycles to solve each level.

continue smoothing and restricting to a coarser grids until we arrive at a grid coarse enough to solve the problem to machine accuracy. This coarse grid is at level h_{\min} . Then we prolong this solution to finer grids by performing a series of coarse-grid corrections, with additional smoothing operations q . In a W-Cycle we start again in a finer grid performing a smooth-restriction process until we arrive to the level h_{\min} . In the prolongation process we perform a V-Cycle to solve to solve each finer level. At the end we visit each level several times. Fig. A.1 shows a diagram which represent both cycles for three multigrid levels. With more number of cycles and depending on the problem the sketch can be more complicated.

Performance

Here we summarise some of the previous results of the performance tests originally presented in [55]. The main difference between the original version of OLLIPTIC and the used to produce the initial data for multiple black hole evolutions are the interface, the mesh refinement and the implementation of high order finite difference stencils. However, the core routines which implement the multigrid method and the parallelization are the same. The original code uses as interface the CACTUS code [40] to read the parameters. However, the grid structure and memory allocation was independent. The new code includes a separate interface which reads parameters from the command line. The implementation of the mesh refinement is straightforward, we only have to apply the algorithm 2.2.2 and redefine the size of the mesh to cover internal regions. The definition of the high order finite difference stencils requires more effort since we have to

Table A.1: OLLIPTIC performance in a single cpu for MG method solving a Poisson equation. For each grid setup we did 6 runs. We use the *linux* command `time` to measure the cpu and wall time. The time displayed in the table is the average of the 6 runs and the uncertainty is given by the standard deviation.

Sub-grids	Mesh points				Time (sec)	
	N_x	N_y	N_z	N_{total}	Wall time	cpu time
1	33	33	33	35937	0.091 ± 0.0015	0.089 ± 0.0022
2	65	65	65	274625	1.75 ± 0.07	1.62 ± 0.078
2	81	81	81	531441	4.8 ± 0.39	4.48 ± 0.059
2	97	97	97	912673	10.6 ± 0.99	9.3 ± 0.43
2	105	105	105	1157625	14.6 ± 0.74	14.5 ± 0.78
3	113	113	113	1442897	20 ± 1.1	18.4 ± 0.23
3	129	129	129	2146689	33.9 ± 0.17	33.7 ± 0.16
3	145	145	145	3048625	52 ± 1.5	50.8 ± 0.45

implement in a general way to switch between orders in an efficient way. OLLIPTIC is written in C++ so we take advantage of the object oriented programming paradigm to provide such implementation. Brief test shows that there is not a big difference in the performance of the new code comparing with the previous version. In fact the new interface work faster and uses less memory. However, the result depends on the hardware, compiler, MPI and OS distribution, etc. The main goal of the original code was the evolution of the Schrödinger-Poisson system [20, 19, 69, 68, 97, 96, 112], where a Poisson equation has to be solved at each time-step. The efficiency in that case was crucial. On the other hand, for initial data the goal is to provide accurate solutions. The new version of the code was exhaustive tested to determine the accuracy but only partially tested to estimate the performance. The old performance test, which we present here are directly applicable for the new second order implementation. We are confident that the high order implementation does not suffer a significant reduction in the performance.

The first test was a comparison between the relaxation method (Gauss-Seidel) and the MG method. We solve a Poisson equation in a single processor for 8 resolutions.⁴ We calculate the working time using the *linux* command `time`. Every run was repeated 6 times to make an statistic. We present the result for the MG method in the table A.1 and in table A.2 for the Gauss-Seidel method. Fig. A.2(a) shows the results and functions which we fit to the data. For MG the

⁴The computer was a desktop with processor AMD-Sempron 1.8 GHz and 1 GB of RAM.

Table A.2: OLLIPTIC performance in a single cpu for Gauss-Seidel method solving a Poisson equation. We use the same procedure as in the MG case (see Table A.1)

Mesh points				Time (sec)	
Nx	Ny	Nz	N_{total}	Wall time	cpu time
33	33	33	35937	0.123 ± 0.006	0.117 ± 0.009
65	65	65	274625	3.2 ± 0.19	2.94 ± 0.078
81	81	81	531441	9.5 ± 0.23	8.3 ± 0.15
97	97	97	912673	21.2 ± 0.98	19.7 ± 0.47
105	105	105	1157625	30 ± 1.8	28.6 ± 0.84
113	113	113	1442897	43 ± 2.2	40.8 ± 0.81
129	129	129	2146689	80 ± 4.1	79 ± 1.5
145	145	145	3048625	146 ± 6.8	138 ± 1.3

results are well represented by a linear function $T(N) = a_1N + b_1$ with $a_1 = (1.77 \pm 0.06) \times 10^{-5}$ and $b_1 = -4 \pm 1$. On the other hand the results for the Gauss-Seidel method are represented by a quadratic function $T(N) = (a_2N + b_2)^2$ with $a_2 = (3.8 \pm 0.06) \times 10^{-6}$ and $b_2 = 0.83 \pm 0.6$.

The test for parallel computation was done in the Kan-Balam computer cluster.⁵ The results were not entirely satisfactory due to hardware issues. Here we show one of the tests in which we keep the total number of grid point approximately constant and we solve the problem increasing the number of processors. In table A.3 we summarise the grid configuration. Table A.4 shows the results where we run 5 times for each configuration to have a representative measurement of the running times. In Fig. A.2(b) we show plot in logarithmic scale of the results. We observe a quite erratic behaviour which can be divided in two sets. Each set is well represented by a function $T(N) = (a_3N + b_3)^{-2/3}$ and $T(N) = (a_4N + b_4)^{-2/3}$ with $a_3 = (7 \pm 2) \times 10^{-4}$, $b_3 = (-4 \pm 1) \times 10^{-4}$, $a_4 = (2 \pm 0.1) \times 10^{-4}$, $b_4 = (-5 \pm 1.2) \times 10^{-4}$. As we can see the “slow” group correspond to the partitions with 2^n with $n \in \{2, \dots, 6\}$ processors. We did not do additional test of the hardware. However, the results suggested a communication problem with the cpu array.

⁵Kan-Balam is a computer cluster available for the numerical relativity group from *Instituto de Ciencias Nucleares, Universidad Nacional Autónoma de México*.

Table A.3: Domain partition per cpus. For MG test we choice the global grid size and partition of the domain in order to keep the total number of grid points almost constant.

Local mesh size			Partition			Total mesh size			N_{total}	N_{cpu}
NxL	NyL	NzL	X	Y	Z	NxG	NyG	NzG		
289	289	289	1	1	1	289	289	289	24137569	1
289	145	145	1	2	2	289	290	290	24304900	4
145	145	145	2	2	2	290	290	290	24389000	8
145	145	97	2	2	3	290	290	291	24473100	12
145	145	73	2	2	4	290	290	292	24557200	16
145	97	97	2	3	3	290	291	291	24557490	18
97	97	97	3	3	3	291	291	291	24642171	27
145	73	73	2	4	4	290	292	292	24726560	32
73	73	73	4	4	4	292	292	292	24897088	64
Average									24520564	

Table A.4: OLLIPTIC performance running in parallel for MG method solving a Poisson equation. Using the grid configuration of Table A.3, we did 5 runs for each configuration. As before we take the average of the time as central value and the standard deviation as error.

Total grid points:		~24520564	
Sub-grids	cpus	Time -wall- (sec)	Time -cpu- (sec)
5	1	667.15 ± 0.32	661.80 ± 0.10
4	4	773.13 ± 0.45	761.53 ± 0.02
4	8	410.20 ± 0.26	398.44 ± 0.11
4	12	111.54 ± 0.89	104.49 ± 0.09
3	16	243.53 ± 0.48	225.59 ± 0.03
4	18	88.65 ± 0.23	77.36 ± 0.10
5	27	63.89 ± 0.56	53.33 ± 0.12
3	32	137.09 ± 0.12	122.18 ± 0.02
3	64	67.45 ± 0.46	52.93 ± 0.19

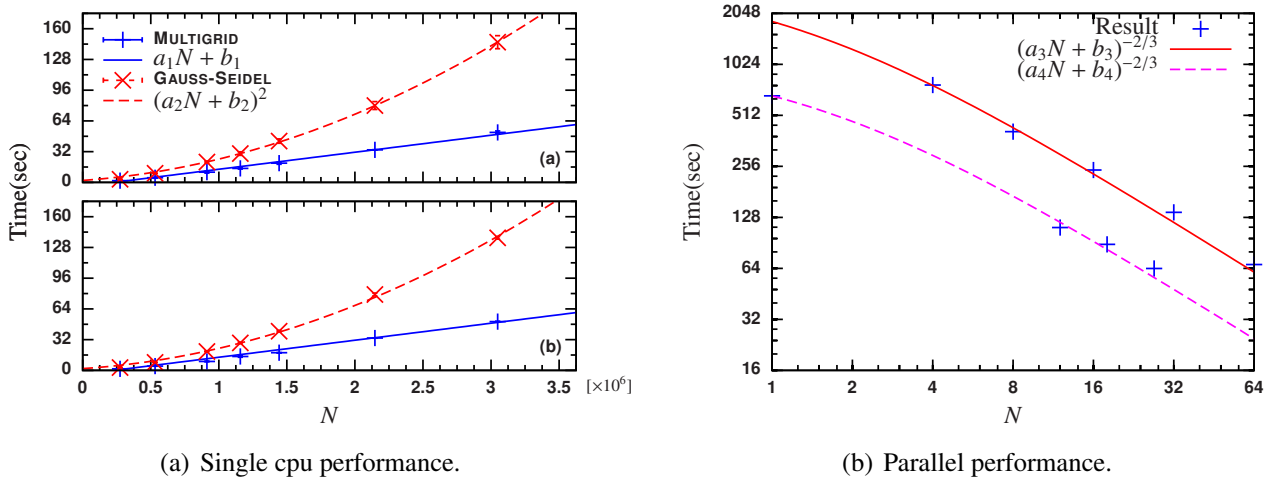


Figure A.2: (a) We compare the performance of the MG method and the Gauss-Seidel method. We confirm the theoretical performance of both methods, for MG the computational cost increases linearly with the total number of mesh points. For the Gauss-Seidel the computational cost grows quadratically. (b) The parallel performance of the code for the MG method is quite erratic. The general behaviour is as an inverse power. However the results group in two categories, each with different coefficients.

Appendix B

Newton-Raphson method

In this appendix we review the Newton-Raphson method and we describe its implementation in OLLIPTIC. The Newton-Raphson method is one of several root-finding algorithm. Given a smooth function $f : \mathbb{R} \rightarrow \mathbb{R}$ with a root in s

$$f(s) = 0, \tag{B.1}$$

it is possible, given a initial test point x_0 , to write down s as the initial value plus a correction h : $s = x_0 + h$. We can use a Taylor expansion of the function

$$f(s) = f(x_0 + h) = f(x_0) + hf'(x_0) + \frac{h^2}{2}f''(x_0) + \dots = 0. \tag{B.2}$$

to get an approximation to the correction

$$h \approx h_0 := -\frac{f(x_0)}{f'(x_0)}. \tag{B.3}$$

where we used only the linear terms of the series. Using now $x_1 := x_0 + h_0$ as a new test point we get a new correction h_1 . We can apply the algorithm iteratively

$$h_n = -\frac{f(x_n)}{f'(x_n)}, \tag{B.4}$$

$$x_{n+1} = x_0 + \sum_{i=0}^n h_i. \tag{B.5}$$

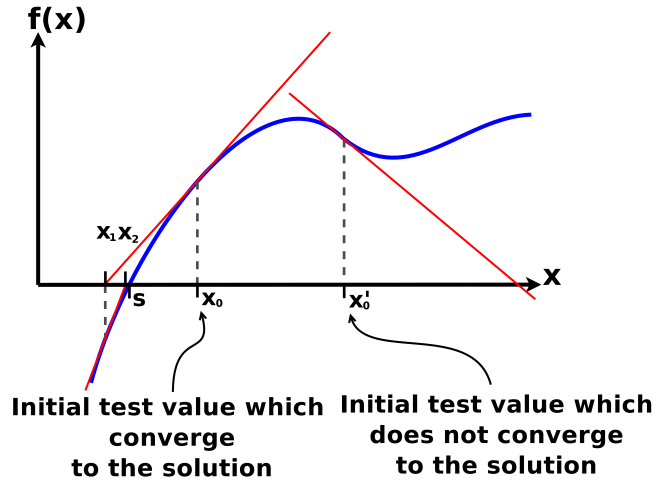


Figure B.1: Newton-Raphson root-finding method. Geometrical example of a few iterations. In one case starting at point x_0 the solution may converge. If the initial guess (for example starting at x'_0) is far from the root, then the root search may fail.

It is possible to combine (B.4) and (B.5) in a single equation

$$x_{n+1} = x_n - \frac{f(x_n)}{f'(x_n)}. \quad (\text{B.6})$$

Each iteration of the Newton-Raphson method has a geometrical meaning. The new test point x_{n+1} is given by the abscissa of the tangent line which touches the point $(x_n, f(x_n))$. In Fig. B.1 we illustrate the procedure for a few iterations. The Newton-Raphson methods converge for a smooth function if we start with an initial guess point that is sufficiently close to a solution. Depending on the function it is possible to start in a point which diverges (see Fig. B.1).¹ Further improvements to the method include the addition of more terms in the Taylor series or the combination with other methods in order to guarantee the convergence in an interval which contain a root.²

In the case of non-linear partial differential equations it is possible to use a similar approach. Particularly in the case of elliptic equations a direct method involve the solution of non-linear

¹If the derivative in (B.6) tends to zero, then the tangent to the curve in $(x_n, f(x_n))$ will cross the x -axis far from the origin and probably far from the root. The tangent in the successive guess points can fall off the approximation.

²A popular method which uses this idea is Brent's algorithm, it combine the bisection method, the secant method and inverse quadratic interpolation [109].

system of equations $\mathbf{A} : \mathbb{R}^m \rightarrow \mathbb{R}^m$ (see Appendix A and [55, 136, 89])

$$\mathbf{A}\vec{u} = \vec{\rho} \quad (\text{B.7})$$

The Newton-Raphson method in this case is given by:

$$\vec{u}_{n+1} = \vec{u}_n + \vec{\delta}_n, \quad (\text{B.8})$$

where $\vec{\delta}_n$ is the solution of

$$\mathbf{J}(\vec{u}_n)\vec{\delta}_n = -\mathbf{A}\vec{u}_n. \quad (\text{B.9})$$

Here $\mathbf{J}(\vec{u}) := \mathbf{A}'(\vec{u}) \in \mathbb{R}^{m \times m}$ is the *Jacobian matrix* of \mathbf{A} with elements

$$J_{ij}(\vec{u}_n) = \frac{\partial}{\partial u_j} A(\vec{u}_n)_i. \quad (\text{B.10})$$

In OLLIPTIC we use an alternative approach. From the definition of the residual (2.18) we get on the lattice location x_{ijk} a non-linear equation

$$r_{ijk} = \mathcal{L}^h(u_{ijk}^n) - \rho_{ijk}, \quad (\text{B.11})$$

where \mathcal{L}^h is the finite difference representation of the non-linear partial differential operator. Depending on the order of the finite difference scheme \mathcal{L} in x_{ijk} can be function of the neighbours (see example below). However, we can consider to solve the equation for u_{ijk} so that the corresponding residual becomes pointwise zero. The Newton-Raphson method that we apply in each point of our grid is

$$u_{ijk}^{n+1} = u_{ijk}^n - \frac{r_{ijk}^n}{\text{d}r_{ijk}^n}, \quad (\text{B.12})$$

here $\text{d}r_{ijk}^w := \frac{\partial}{\partial u_{ijk}} \mathcal{L}^h(u_{ijk}^n)$. In practise instead of solving Eq. (B.12), we do only one iteration in order to reduce r_{ijk} . It is important to notice that in this case we take an entire vector of unknowns \vec{u}_n , and we calculate a new estimation \vec{u}_{n+1} working component by component. Then, we have to distinguish between the convergences of the iterative solver (Gauss-Seidel relaxation) and the convergence of the root-finding algorithm. Taking a single step in the root-finding procedure we combine the two iterations in a single process. If the solution of the

PDE problem has a local unique solution, and we start with an initial guess function pointwise enough close to that solution, then during the iterative process the vector solution will converge component by component to the solution. In OLLIPTIC we use as initial guess function $\vec{u}^0 = \vec{0}$. For our numerical experiments the solution converges to the analytical one in every case.

For example, the implementation for the boundary condition (2.10) in direction $-\hat{y}$ is given by

$$r_{ijk} := D_y^{p+} u_{ijk}^n - \frac{qy_{ijk}}{r_{ijk}^2} (A - u_{ijk}^n), \quad (\text{B.13})$$

$$dr_{ijk} := \frac{\partial}{\partial u_{ijk}} D_y^+ u_{ijk}^n + \frac{qy_{ijk}}{r_{ijk}^2} u_{ijk}^n, \quad (\text{B.14})$$

$$u_{ijk}^{n+1} \rightarrow u_{ijk}^n - \frac{r_{ijk}}{dr_{ijk}}, \quad (\text{B.15})$$

where D_y^{p+} is the forward difference operator of order p in the y -direction, u_{ijk} , r_{ijk} and y_{ijk} are the values of u , r , and y , respectively, at the lattice location (i, j, k) , and n is an iteration index. For example, in the case $p = 2$ we obtain

$$D_y^{2+} u_{ijk} = -\frac{3u_{ijk} - 4u_{i,j+1,k} + u_{i,j+2,k}}{2\Delta y}, \quad (\text{B.16})$$

$$\frac{\partial}{\partial u_{ijk}} D_y^{2+} u_{ijk}^n = -3/2\Delta y. \quad (\text{B.17})$$

Note that Eq. (B.13) is linear in u_{ijk} , so in fact the algorithm is equivalent to implementing the explicit finite difference formula, with the advantage that its implementation is easier.

Appendix C

Convergence of C^n functions

In certain cases, the order of convergence of a finite difference scheme can be higher in the interior than at the boundary, without the lower order at the boundary spoiling the convergence in the interior (e.g. [89], Sec. 2.12). Here we estimate the order of convergence of a standard p -order finite difference scheme for an elliptic problem, where the solution is C^∞ everywhere except on the origin where it is C^n (where $n < p$). In order to simplify the notation, we will later restrict the examples to the one dimensional case. However, the extension to the three dimensional case is straightforward.

Let \mathcal{L} be an elliptic operator, $\Omega \subset \mathbb{R}^3$ an open domain, and $u : \Omega \rightarrow \mathbb{R}$ the solution of the problem

$$\mathcal{L}u(\vec{x}) = \rho \quad \text{for} \quad \vec{x} \in \Omega, \quad (\text{C.1})$$

$$\mathcal{B}u(\vec{x}) = u_b(\vec{x}) \quad \text{for} \quad \vec{x} \in \partial\Omega, \quad (\text{C.2})$$

where \mathcal{B} is a boundary operator, $\rho : \Omega \rightarrow \mathbb{R}$ is a source term, and $u \in C_0^\infty(\Omega) \cap C^n(0)$. Let \mathcal{L}^h be a finite difference representation of order p of \mathcal{L} in a mesh $\Omega^h \subset \mathbb{N}^3$ with a uniform grid size h . The numerical solution $U^h : \Omega^h \rightarrow \mathbb{R}$ satisfies

$$\mathcal{L}^h U^h(\vec{x}^h) = \rho^h(\vec{x}^h) \quad \text{for} \quad \vec{x}^h \in \Omega^h, \quad (\text{C.3})$$

$$\mathcal{B}^h U^h(\vec{x}^h) = u_b^h(\vec{x}^h) \quad \text{for} \quad \vec{x}^h \in \partial\Omega^h, \quad (\text{C.4})$$

where \mathcal{B}^h is a discrete boundary operator and ρ^h is the restriction of ρ on Ω^h .

Given a point $x \in \Omega$, we identify points between Ω^h and Ω by $x_i = x_0 + ih$, where $i \in \{0, 1, \dots, N\}$. For every grid function we use as notation $U_i := U^h(x_i)$. The finite difference representation of \mathcal{L} on the lattice location x_i has for each direction the form

$$\mathcal{L}^h U_i^h = \sum_{l=i-p}^{i+p} a_{l-i} U_l, \quad (\text{C.5})$$

where the coefficients a_{l-i} depend of the order of approximation and the kind of stencil. For example, the standard 2nd order centred approximation to the second derivative is defined by $a_0 = -2/h^2$, $a_{\pm 1} = 1/h^2$.

The truncation error is defined by

$$\tau^h := |\mathcal{L}^h u^h - \rho^h|, \quad (\text{C.6})$$

where u^h is the restriction of u to the grid Ω^h . The approximation has the order of consistency $p > 0$ if there is $h_0 > 0$ which for all positive $h < h_0$ satisfies

$$\tau^h \leq Ch^p, \quad (\text{C.7})$$

with a constant $C > 0$ independent of h . The standard approach to analysing the error in a finite difference approximation is to expand each of the function values of u^h in a Taylor series about the point (x_i) . Taylor's theorem states that for a function $u \in C^{n-1}([x_i, x])$ and $u \in C^n((x_i, x))$,

$$u(x) = \sum_{k=0}^{n-1} \frac{u_i^{(k)}}{k!} (x - x_i)^k + \frac{u^{(n)}(\xi)}{n!} (x - x_i)^n, \quad (\text{C.8})$$

where $\xi \in [x_i, x]$ and $u^{(n)}$ denotes the n -th derivative. For grid functions the expansion formula is

$$u_j = \sum_{k=0}^{n-1} \frac{u_i^{(k)}}{k!} (j - i)^k h^k + \frac{u^{(n)}(\xi)}{n!} (j - i)^n h^n. \quad (\text{C.9})$$

Using (C.5) and (C.9), it is possible to calculate

$$\begin{aligned} \mathcal{L}^h u_i^h &= \sum_{l=i-p}^{i+p} \sum_{k=0}^{n-1} a_{l-i} \frac{u_i^{(k)}}{k!} (l-i)^k h^k \\ &+ \sum_{l=i-p}^{i+p} \sum_{k=0}^{n-1} a_{l-i} \frac{u^{(n)}(\xi)}{n!} (j-i)^n h^n. \end{aligned} \quad (\text{C.10})$$

If $n \geq p$ and the operator \mathcal{L} contains a linear combination of derivatives up to order $n-1$, then it is possible to select the coefficients a_i to cancel the remaining factors. We obtain

$$\begin{aligned} \mathcal{L}^h u_i^h &= \mathcal{L} u_i^h + \sum_{l=i-p}^{i+p} \sum_{k=p}^{n-1} a_{l-i} \frac{u_i^{(k)}}{k!} (l-i)^k h^k \\ &+ \sum_{l=i-p}^{i+p} \sum_{k=0}^{n-1} a_{l-i} \frac{u^{(n)}(\xi)}{n!} (j-i)^n h^n, \end{aligned} \quad (\text{C.11})$$

where now the second summand starts at $k = p$. If $|u^{(n)}(\xi)|$ is bounded, the dominant term is of order h^p . A substitution with (C.6) leads to

$$\tau^h \leq \left| \sum_{l=i-p}^{i+p} a_{l-i} \frac{u_i^{(p)}}{p!} (l-i)^p \right| h^p, \quad (\text{C.12})$$

where the factor is bounded and independent of h . If we use the same scheme close to the origin, where $n < p$, we are not able to cancel terms lower than h^n :

$$\mathcal{L}^h u_i^h = \mathcal{L} u_i^h + \sum_{l=i-p}^{i+p} \sum_{k=0}^{n-1} a_{l-i} \frac{u^{(n)}(\xi)}{n!} (j-i)^n h^n. \quad (\text{C.13})$$

The truncation error in this case is of order $n < p$,

$$\tau^h \leq \left| \sum_{l=i-p}^{i+p} a_{l-i} \frac{u^{(n)}(\xi)}{n!} (l-i)^n \right| h^n. \quad (\text{C.14})$$

For example, for the operator

$$\mathcal{L} = \frac{\partial^2}{\partial x^2}, \quad (\text{C.15})$$

the 4th order centred approximation to the second derivative is

$$\mathcal{L}^h u_i^h = -\frac{u_{i-2} - 16u_{i-1} + 30u_i - 16u_{i+1} + u_{i+2}}{12h^2}. \quad (\text{C.16})$$

If $u \in C_0^\infty(\mathbb{R}) \cap C^2(0)$ and $0 \in [x_{i+1}, x_{i+2}]$, a substitution of the Taylor series of $x_{i\pm 2}$ and $x_{i\pm 1}$ in equation (C.16) results in

$$\begin{aligned} \mathcal{L}^h u_i^h &= \frac{\partial^2 u_i^h}{\partial x^2} + \frac{1}{9}h \left(\frac{\partial^3 u_i^h}{\partial x^3} - \frac{\partial^3 u^h(\xi)}{\partial x^3} \right) + \\ &\quad \frac{1}{18}h^2 \frac{\partial^4 u^h(\xi)}{\partial x^4} + O(h^3), \end{aligned} \quad (\text{C.17})$$

where we expand the term x_{i+2} only up to $O(h^2)$. The truncation error is of order $O(h)$.

Appendix D

First and second post-Newtonian Hamiltonian

Here we reproduce in our notation the Hamiltonian given in [113, 93]

$$\begin{aligned}
 H_1 = & -\frac{1}{8} \sum_a m_a \left(\frac{\vec{p}_a^2}{m_a^2} \right)^2 - \frac{1}{4} \sum_a \sum_{b \neq a} \frac{1}{r_{ab}} \left(6 \frac{m_b}{m_a} \vec{p}_a^2 - 7 \vec{p}_a \cdot \vec{p}_b - (\hat{n}_{ab} \cdot \vec{p}_a)(\hat{n}_{ab} \cdot \vec{p}_b) \right) \\
 & + \frac{1}{2} \sum_a \sum_{b \neq a} \sum_{c \neq a} \frac{m_a m_b m_c}{r_{ab} r_{ac}}.
 \end{aligned} \tag{D.1}$$

$$\begin{aligned}
 H_2 = & \frac{1}{16} \sum_a m_a \left(\frac{\vec{p}_a^2}{m_a^2} \right)^3 + \frac{1}{16} \sum_a \sum_{b \neq a} \frac{m_a^{-1} m_b^{-1}}{r_{ab}} \left[10 \left(\frac{m_b}{m_a} \vec{p}_a^2 \right)^2 - 11 \vec{p}_a^2 \vec{p}_b^2 - 2 (\vec{p}_a \cdot \vec{p}_b)^2 \right. \\
 & + 10 p_a^2 (\hat{n}_{ab} \cdot \vec{p}_b)^2 - 12 (\vec{p}_a \cdot \vec{p}_b) (\hat{n}_{ab} \cdot \vec{p}_a) (\hat{n}_{ab} \cdot \vec{p}_b) - 3 (\hat{n}_{ab} \cdot \vec{p}_a)^2 (\hat{n}_{ab} \cdot \vec{p}_b)^2 \left. \right] \\
 & + \frac{1}{8} \sum_a \sum_{b \neq a} \sum_{c \neq a} \frac{1}{r_{ab} r_{ac}} \left[18 \frac{m_b m_c}{m_a} \vec{p}_a^2 + 14 \frac{m_a m_c}{m_b} \vec{p}_b^2 - 2 \frac{m_a m_c}{m_b} (\hat{n}_{ab} \cdot \vec{p}_b)^2 \right. \\
 & - 50 m_c (\vec{p}_a \cdot \vec{p}_b) + 17 m_a (\vec{p}_b \cdot \vec{p}_c) - 14 m_c (\hat{n}_{ab} \cdot \vec{p}_a) (\hat{n}_{ab} \cdot \vec{p}_b) \\
 & + 14 m_a (\hat{n}_{ab} \cdot \vec{p}_b) (\hat{n}_{ab} \cdot \vec{p}_c) + m_a (\hat{n}_{ab} \cdot \hat{n}_{ac}) (\hat{n}_{ab} \cdot \vec{p}_b) (\hat{n}_{ac} \cdot \vec{p}_c) \left. \right] \\
 & + \frac{1}{8} \sum_a \sum_{b \neq a} \sum_{c \neq a} \frac{1}{r_{ab}^2} \left[2 m_b (\hat{n}_{ab} \cdot \vec{p}_a) (\hat{n}_{ac} \cdot \vec{p}_c) + 2 m_b (\hat{n}_{ab} \cdot \vec{p}_b) (\hat{n}_{ac} \cdot \vec{p}_c) \right. \\
 & \left. + \frac{m_a m_b}{m_c} \left(5 (\hat{n}_{ab} \cdot \hat{n}_{ac}) \vec{p}_c^2 - (\hat{n}_{ab} \cdot \hat{n}_{ac}) (\hat{n}_{ac} \cdot \vec{p}_c)^2 - 14 (\hat{n}_{ab} \cdot \vec{p}_c) (\hat{n}_{ac} \cdot \vec{p}_c) \right) \right]
 \end{aligned}$$

$$\begin{aligned}
& +\frac{1}{4} \sum_a \sum_{b \neq a} \frac{m_a}{r_{ab}^2} \left[\frac{m_b}{m_a} \vec{p}_a^2 + \frac{m_a}{m_b} \vec{p}_b^2 - 2(\vec{p}_a \cdot \vec{p}_b) \right] \\
& +\frac{1}{2} \sum_a \sum_{b \neq a} \sum_{c \neq a,b} \frac{(n_{ab}^i + n_{ac}^i)(n_{ab}^j + n_{cb}^j)}{(r_{ab} + r_{bc} + r_{ca})^2} \left[8m_b(p_{ai}p_{cj}) - 16m_b(p_{aj}p_{ci}) \right. \\
& +3m_c(p_{ai}p_{bj}) + 4\frac{m_a m_b}{m_c}(p_{ci}p_{cj}) + \frac{m_b m_c}{m_a}(p_{ai}p_{aj}) \left. \right] \\
& +\frac{1}{2} \sum_a \sum_{b \neq a} \sum_{c \neq a,b} \frac{m_a m_b m_c}{(r_{ab} + r_{bc} + r_{ca}) r_{ab}} \left[8 \frac{\vec{p}_a \cdot \vec{p}_c - (\hat{n}_{ab} \cdot \vec{p}_a)(\hat{n}_{ab} \cdot \vec{p}_c)}{m_a m_c} \right. \\
& \left. -3 \frac{\vec{p}_a \cdot \vec{p}_b - (\hat{n}_{ab} \cdot \vec{p}_a)(\hat{n}_{ab} \cdot \vec{p}_b)}{m_a m_b} - 4 \frac{\vec{p}_c^2 - (\hat{n}_{ab} \cdot \vec{p}_c)^2}{m_c^2} - \frac{\vec{p}_a^2 - (\hat{n}_{ab} \cdot \vec{p}_a)^2}{m_a^2} \right] \\
& -\frac{1}{2} \sum_a \sum_{b \neq a} \sum_{c \neq b} \frac{m_a^2 m_b m_c}{r_{ab}^2 r_{bc}} - \frac{1}{4} \sum_a \sum_{b \neq a} \sum_{c \neq a} \frac{m_a m_b m_c}{r_{ab} r_{ac}} \left(\frac{m_c}{r_{ac}} + 3 \frac{m_a}{r_{ab}} \right) \\
& -\frac{3}{8} \sum_a \sum_{b \neq a} \sum_{c \neq a,b} \frac{m_a^2 m_b m_c}{r_{ab} r_{ac} r_{bc}} + \frac{1}{2} \sum_a \sum_{b \neq a} \frac{m_a^2 m_b}{r_{ab}^3} \left(m_a + \frac{3}{4} m_b \right) \\
& -\frac{1}{64} \sum_a \sum_{b \neq a} \sum_{c \neq a,b} \frac{m_a^2 m_b m_c}{r_{ab} r_{ac}^3 r_{bc}} \{ 18r_{ac}^2 - 60r_{bc}^2 - 24r_{ac}(r_{ab} + r_{bc}) \\
& +60 \frac{r_{ac} r_{bc}^2}{r_{ab}} + 56r_{ab} r_{bc} - 72 \frac{r_{bc}^3}{r_{ab}} + 35 \frac{r_{bc}^4}{r_{ab}^2} + 6r_{ab}^2 \} - \frac{1}{4} \sum_a \sum_{b \neq a} \frac{m_a^2 m_b^2}{r_{ab}^3}. \tag{D.2}
\end{aligned}$$

Ehrenwörtliche Erklärung

Ich erkläre hiermit ehrenwörtlich, dass ich die vorliegende Arbeit selbständig, ohne unzulässige Hilfe Dritter und ohne Benutzung anderer als der angegebenen Hilfsmittel und Literatur angefertigt habe. Die aus anderen Quellen direkt oder indirekt übernommenen Daten und Konzepte sind unter Angabe der Quelle gekennzeichnet.

Bei der Auswahl und Auswertung folgenden Materials haben mir die nachstehend aufgeführten Personen in der jeweils beschriebenen Weise unentgeltlich geholfen:

1. Prof. Bernd Bruegmann (beratend).

Weitere Personen waren an der inhaltlich-materiellen Erstellung der vorliegenden Arbeit nicht beteiligt. Insbesondere habe ich hierfür nicht die entgeltliche Hilfe von Vermittlungs- bzw. Beratungsdiensten (Promotionsberater oder anderen Personen) in Anspruch genommen. Niemand hat von mir unmittelbar oder mittelbar geldwerte Leistungen für Arbeiten erhalten, die im Zusammenhang mit dem Inhalt der vorgelegten Dissertation stehen.

Die Arbeit wurde bisher weder im In- noch im Ausland in gleicher oder ähnlicher Form einer anderen Prüfungsbehörde vorgelegt.

Die geltende Promotionsordnung der Physikalisch-Astronomischen Fakultät ist mir bekannt.

Ich versichere ehrenwörtlich, dass ich nach bestem Wissen die reine Wahrheit gesagt und nichts verschwiegen habe.

Jena, December 16, 2010

Juan Pablo Galaviz Vilchis

Zusammenfassung

In dieser Arbeit wurde ein numerischer, elliptischer Löser, *OLLIPTIC*, präsentiert. Als erste Anwendung wurde die Hamiltonsche Zwangsbedingung gelöst, um numerische Anfangsdaten für Simulationen mit mehreren Schwarzen Löchern zu erhalten. *Olliptic* implementiert eine "Multigrid"-Methode hoher Ordnung, die parallelisiert ist und Boxen-basierte Gitterverfeinerung verwendet. Die Tests und ersten Anwendungen des Codes zeigen, dass der neue Code für unsere Zwecke genau genug zu sein scheint. Allerdings fanden wir das Nahe an der Punktur die Konvergenz-Rate geringer ist als gewünscht, was man für Punktur Daten (siehe Anhang C) erwartet. Der Abfall der Konvergenz nahe der Punkturen spiegelt sich nicht in der Konvergenz der Zeitentwicklung wieder.

Wir haben Entwicklungen von drei Schwarzen Löchern gezeigt, für deren Anfangsdaten die Lösungen der Hamiltonschen Zwangsbedingung, wie sie durch den neuen elliptischen Löser generiert wurden, verwendet wurden. Wir haben unsere Anfangsdaten mit denen einer bestimmten analytischen Näherung für Anfangsdaten verglichen. Im Falle dreier Schwarzer Löcher ist die aus den genäherten Anfangsdaten resultierende Dynamik von der in Zeitentwicklungen, die die Hamiltonsche Zwangsbedingung numerisch erfüllen, verschieden. Wie zu vermuten, sind die Trajektorien der Punkturen sensitiv auf kleine Änderungen in den Anfangsdaten. Besonders, für drei und mehr Schwarze Löcher kann eine Änderung der Anfangsdaten, z.B. durch das Lösen der Zwangsbedingungen statt eine analytische Näherung zu verwenden, zu qualitativ und quantitativ sehr unterschiedlichen Verschmelzungssequenzen führen. Dennoch haben wir die Resultate von [42, 94] bestätigt, wie erwartet, dass sich die Punktur Methode auf natürliche Weise für die Simulation mehrerer Schwarzer Löcher eignet.

Simulationen dreier, vierer oder gar mehrerer Schwarzer Löcher führt zur der folgenden Frage über allgemeinere Verschmelzungs Situationen: Wie kann man die Anzahl der in einer Verschmelzung beteiligten Schwarzen Löchern aus der Beobachtung ihrer Gravitationswellen bestimmen? Eine erste Analyse dieses Themas wurde zuvor im Newtonschen Fall gegeben [9, 127]. Unter Verwendung Post-Newtonscher Techniken und voll relativistischer, numerischer Simulationen haben wir mit der Erforschung eines einfachen Falles begonnen, in dem wir Evidenz aufzeigen, die die anfängliche Vermutung von [127] unterstützt, welche wir hier umformulieren:

Um ein System mit N kompakten Objekten zu charakterisieren ist es nötig eine Analyse der Wellenformen einschliesslich mindestens der $l \leq N$ Moden durchzuführen.¹ Im hochrelativistischen Fall untersuchen wir eine symmetrische Konfiguration dreier Schwarzer Löcher gleicher Massen, die spiralförmig verschmelzen ähnlich wie ein Binärsystem zweier Schwarzer Löcher gleicher Massen in einer quasi-zirkularen Verschmelzung. Wir haben im Fall der drei Schwarzen Löcher gefunden, dass die $l = 3, m = 3$ Moden von gleicher Grössenordnung oder grösser sind als die $l = 2, m = 2$ Moden. Für das binär System finden wir gegenteilig, dass die $l = m = 3$ Moden beinahe Null sind. Unter Verwendung Post-Newtonscher Simulationen einer bestimmten hierarchischen Konfiguration haben wir die Wellenformen betrachtet. Wir fanden, dass es möglich ist zwischen dem Jacobischen - und dem Binärsystem durch den Massenoktupol - und Stromquadrupolteil der Wellenform zu unterscheiden. Zusätzlich fanden wir in diesem Fall eine Beziehung zwischen den Modulationen der $l = 3$ Moden und der Periode des dritten kompakten Objekts. Wir haben einen Zusammenhang zwischen der Amplitude der $l = 3, m = 2$ und $l = 3, m = 3$ Moden und dem Winkel der oskulierenden Orbitalebene gefunden.

In Zukunft planen wir unsere in dieser Thesis präsentierte Forschung des Dreikörperproblems auszuweiten. Mit numerischen Methoden planen wir die Charakterisierung der dreifach Verschmelzung mithilfe der Analyse der höheren Moden der Wellenformen zu untersuchen. Wir planen den Einfluss des Spins auf den Ausstoss oder die Verschmelzung der drei Körper zu studieren. Mit Post-Newtonschen Techniken planen wir eine systematische Studie des hierarchischen Systems sowie langsamen Zusammentreffen. Wir planen die Berechnung der Wellenformen (wahrscheinlich inklusive Post-Newtonscher Korrekturen) und die Multipolzerlegung zu verbessern. Das Studium dreier kompakter, spinnender Körper im Post-Newtonschen Formalismus ist ein Problem in unserer Reichweite. Ein interessantes Problem ist das Studium von Chaos im Dreikörperproblem aus der Post-Newtonschen Sichtweise und insbesondere unter Berücksichtigung gravitativer Abstrahlung.

¹Die ursprüngliche Aussage in [127] lautet: *...Classification of N (or fewer) particles producing (nearly) the same wave forms requires inclusion of the l th multiple part with $l \leq N$*

Acknowledgments

I would like to thank Prof. Bernd Brüggmann, for all the support and teachings. Additionally, it is a pleasure to thank my colleagues at the TPI particularly to Sebastiano Bernuzzi, Zhoujian Cao, Roman Gold, David Hilditch and Milton Ruiz for valuable discussions and comments on this thesis.

This thesis is dedicated to my parents, Alicia and Manuel, my brothers Victor and Maricela and especially my nephews Daniel, Braulio, Bruno, Briana and Ana Victoria which are my main motivation. Also, I would like to dedicate this thesis to my aunt Lupita and my cousins Rodolfo and Alvaro.

I would like to do a special acknowledgment to my *alma mater* the National Autonomous University of Mexico, where I got my main scientific education. I would like to thank particularly Miguel Alcubierre, Darío Núñez, Tonatiuh Matos and my friends Tanya, Anabel, Nico, Ali, Alejandro and a long list which is impossible to mention here.

Agradecimientos

Quisiera agradecer todo el apoyo y enseñanzas a mi supervisor Prof. Bernd Brüggmann. A mis colegas del instituto, en particular a Sebastiano Bernuzzi, Zhoujian Cao, Roman Gold, David Hilditch y Milton Ruiz por brindarme su amistad y por las valiosas discusiones y comentarios sobre este trabajo.

Esta tesis es dedicada con mucho cariño a mis padres Alicia y Manuel, mis hermanos Victor y Maricela y especialmente a mis sobrinos Daniel, Braulio, Bruno, Briana y Ana Victoria que son mi principal motivación. Igualmente dedico esta tesis a toda mi familia, en particular a mi Tía Lupita y a mis primos Rodolfo y Alvaro por ser además mis amigos de siempre.

Quisiera hacer un especial reconocimiento a mi alma máter la Universidad Nacional Autónoma de México, a la cual le debo mi formación. A mis compañeros y profesores, en particular a Miguel Alcubierre, Darío Núñez y Tonatiuh Matos. A todos mis amigos Tannya, Anabel, Nico, Ali, Alejandro y una larga lista que no aparece aquí, gracias por su amistad.

Numerical simulations of three black holes

Juan Pablo Galaviz Vilchis

1. “We have presented a numerical elliptic solver, OLLIPTIC ... the new code seems to be sufficiently accurate for our purposes.”
2. “... we found that close to the puncture the convergence rate is less than that desired ”
3. “The drop in the convergence close to the punctures is not reflected in the convergence of the evolution.”
4. “In the case of three black holes, the dynamics resulting from approximate data is different from the dynamics produced by evolutions which satisfy the Hamiltonian constraint numerically.”
5. “As anticipated, the puncture tracks are sensitive to small changes in the initial data.”
6. “... the puncture method lends itself naturally to the simulation of multiple black holes.”
7. “In the highly relativistic case, ... in the case of the triple merger the mode $l = m = 3$ is of the same order or bigger than the $l = m = 2$ mode. For the binary system we find the opposite, namely the $l = m = 3$ mode is almost zero.”
8. “Using post-Newtonian simulations ... looking at the mass octupole and current quadrupole part of the waveform, it is possible to distinguish between a Jacobian system and a binary system.“
9. “... we found a relation between the modulation of the modes $l = 3$ and the period of the third compact object.”
10. “We established a link between the amplitude of the $l = 3, m = 2$ and $l = 3, m = 3$ modes and the angle of the osculating orbital planes.”

Numerische Simulationen dreier Schwarzer Loecher

Juan Pablo Galaviz Vilchis

1. "In dieser Arbeit wurde ein numerischer, elliptischer Löser, OLLIPTIC, präsentiert ... Der neue Code scheint für unsere Zwecke genau genug zu sein."
2. "... fanden wir das Nahe an der Punktur die Konvergenz-Rate geringer ist als gewünscht "
3. "Der Abfall der Konvergenz nahe der Punkturen spiegelt sich nicht in der Konvergenz der Zeitentwicklung wieder."
4. "Im Falle dreier Schwarzer Löcher ist die aus den genäherten Anfangsdaten resultierende Dynamik von der in Zeitentwicklungen, die die Hamiltonsche Zwangsbedingung numerisch erfüllen, verschieden."
5. "Wie zu vermuten, sind die Trajektorien der Punkturen sensitiv auf kleine Änderungen in den Anfangsdaten."
6. "... die Punktur Methode eignet sich auf natürliche Weise für die Simulation mehrerer Schwarzer Löcher."
7. "Im hoch-relativistischen Fall haben wir im Fall der drei Schwarzen Löcher gefunden, dass die $l = 3, m = 3$ Moden von gleicher Grössenordnung oder grösser sind als die $l = 2, m = 2$ Moden. Für das binär System finden wir gegenteilig, dass die $l = m = 3$ Moden beinahe Null sind."
8. "Unter Verwendung Post-Newtonscher Simulationen fanden wir, dass es möglich ist zwischen dem Jacobischen - und dem Binärsystem durch den Massenoktupol - und Stromquadrupolteil der Wellenform zu unterscheiden."
9. "... wir fanden in diesem Fall eine Beziehung zwischen den Modulationen der $l = 3$ Moden und der Periode des dritten kompakten Objekts."
10. "Wir haben einen Zusammenhang zwischen der Amplitude der $l = 3, m = 2$ und $l = 3, m = 3$ Moden und dem Winkel der oskulierenden Orbitalebene gefunden."